Mjerenje toplinskog kapaciteta u sustavima s kompleksnim faznim dijagramom s magnetskim poljem duž osi teške magnetizacije

Bonačić, Nives

Master's thesis / Diplomski rad

2016

Degree Grantor / Ustanova koja je dodijelila akademski / stručni stupanj: **University of Zagreb, Faculty of Science / Sveučilište u Zagrebu, Prirodoslovno-matematički fakultet**

Permanent link / Trajna poveznica: https://urn.nsk.hr/urn:nbn:hr:217:879734

Rights / Prava: In copyright/Zaštićeno autorskim pravom.

Download date / Datum preuzimanja: **2024-12-18**

UNIVERSITY OF ZAGREB

FACULTY OF SCIENCE

DEPARTMENT OF PHYSICS

Nives Bonačić

Measurements of heat capacity of systems with complex magnetic phase diagrams for magnetic field along hard magnetisation axes

Master Thesis

Zagreb, 2016

SVEUČILIŠTE U ZAGREBU

PRIRODOSLOVNO-MATEMATIČKI FAKULTET

FIZIČKI ODSJEK

Nives Bonačić

Mjerenje toplinskog kapaciteta u sustavima s kompleksnim faznim dijagramom s magnetskim poljem duž osi teške magnetizacije

Diplomski rad

Zagreb, 2016

UNIVERSITY OF ZAGREB

FACULTY OF SCIENCE

DEPARTMENT OF PHYSICS

STUDY PROGRAM: Research oriented study of physics

Nives Bonačić

Master Thesis

Measurements of heat capacity of systems with complex magnetic phase diagrams for magnetic field along hard magnetisation axes

1. Advisor: prof. Christian Pfleiderer, Ph. D.

2. Advisor: assist. prof. dr. Mihael Srđan Grbić

Master Thesis grade: _____

Commission: 1. _____

2. _____

3. _____

Master Thesis defence date: _____

Zagreb, 2016

Mjerenje toplinskog kapaciteta u sustavima s kompleksnim faznim dijagramom s magnetskim poljem duž osi teške magnetizacije

Sažetak

Od otkrića topološki netrivijalnih uređenja, npr. faze rešetke skirmiona u MnSi-u 2009. godine [1], izrazito je povećan intenzitet istraživanja u ovom području. Ključni eksperimentalni potpis su magnetske strukture u više k smjerova, ispitivane raspršenjem neutrona pod malim kutom, dok se za $k = 0$ promatraju masivna magnetska svojstva poput topološkog Hallovog efekta koji proizlazi zbog pojave baždarnog polja, teorijski nađene manifestacije Berryjeve zakrivljenosti pobuđenja. Mjerenjem topoloških Hall signala identificirani su novi magnetski sustavi i skupine spojeva u kojima bi mogla nastati netrivijalna spinska stanja. Kao jedan kandidat je u našoj grupi izdvojena serija RE-Cu intermetalnih spojeva s antiferomagnetskim uređenjem u više k smjerova i vrlo velikom topološkom Hallovom otpornošću, dva reda veličine većom nego u A-fazi MnSi-a. Magnetska anizotropija je ključni sastojak energijske hijerarhije interakcija. Zbog javljanja snažnog zakretnog momenta u konačnom magnetskom polju i neprikladnosti sadašnjih mjernih postava i kalorimetrijskih tehnika, dosad nije postojala mogućnost dodatnog istraživanja mogućih potpisa spinskih tekstura masivnim mjerenjima npr. toplinskog kapaciteta. Stoga, uglavnom nema dostupnih informacija o pratećim promjenama entropije duž granica faza. U ovom radu su dizajnirani, konstruirani, karakterizirani i optimizirani sasvim novi postavi za mjerenje toplinskog kapaciteta koji prevladavaju navedeni problem osiguravajući mehaničku stabilnost usprkos zakretnih momenata koji djeluju na uzorak pri mjerenjima s jakim magnetskim poljem uzduž osi teške magnetizacije. Dva nova eksperimentalna postava su implementirana u komercijalno dostupan uređaj Physical Property Measurements System-a (PPMS) od Quantum Design-a, jedan koristeći vijcima stegnutu Al pločicu umjesto platforme za uzorak i drugi Kevlar postav potpuno nove strukture koja se može ugađati i podešavati za različite materijale. Detaljno su uspoređeni novi postavi s konvencionalnim kalorimetrom. Njima je određen specifični toplinski kapacitet ErCu duž tri glavne kristalografske osi u temperaturnom rasponu $2\,\mathrm{K}$ do $200\,\mathrm{K}$ i poljima do $14\,\mathrm{T}$. Time su razjašnjeni bogati magnetski fazni dijagrami i utvrđen strukturni prijelaz. Ne-magnetski ekvivalent materijala LuCu je pripremljen i njegov specifični toplinski kapacitet izmjeren za utvrđivanje magnetskog doprinosa spojeva od interesa.

Measurements of heat capacity of systems with complex magnetic phase diagrams for magnetic field along hard magnetisation axes

Abstract

Since the discovery of topologically non-trivial forms of order, e.g. the skyrmion lattice phase in MnSi in 2009 [1], the intensity of research in this field increased tremendously. The key experimental signatures are multiple-k structures as probed by small-angle neutron scattering, while in the $k = 0$ space, e.g. bulk magnetic properties, a large topological Hall effect arises due to an emergent gauge field as theoretically found to be a manifestation of the Berry curvature of the excitations involved. The latter route was followed to identify new magnetic systems or compound families, possibly hosting non-trivial spin states by measuring a topological Hall effect signal. As one class the rare-earth intermetallics series RE-Cu were recently identified in our group as having multiple-k antiferromagnetic orderings and very large topological Hall resistivity two orders of magnitude higher than in the A-phase of MnSi. One key element to the energetic hierarchy of interactions is the magnetic anisotropy. To further probe possible signatures of spin textures by other bulk measurements, e.g. heat capacity, no option so far is available since strong magnetic torques in finite magnetic fields along hard magnetisation axes forbid detailed investigations by present state-of-the-art calorimetric techniques. Therefore essentially no information is available on the underlying changes in entropy across the phase boundaries. To overcome this issue an entirely new design to measure heat capacity was invented, constructed, characterised and optimised during the course of this master thesis to ensure mechanical stability against torques acting on the sample when applying magnetic fields along the hard axes. Two setups were designed, one a screw tightened Al-plate as sample platform and second a Kevlar setup which has a completely new structure, permitting to tune and adjust the setup for different materials, both fitting to a commercially available sample puck provided by the Physical Property Measurements System (PPMS) from Quantum Design. We started with a detailed characterization of the new setups in comparison to the conventional heat pulse calorimeter technique and concentrated on the heat capacity of ErCu along the three principal crystallographic directions in the temperature range from $2\,\mathrm{K}$ to $200\,\mathrm{K}$ up to magnetic fields of $14\,\mathrm{T}$. It enabled us to shed light to the rich magnetic phase diagram in identifying a structural transition. A non-magnetic equivalent of the material - LuCu - was prepared and its specific heat was used to find the magnetic contribution in the compounds of interest.

Contents

1 Introduction

1.1 *Emergence of complex spin structures*

Recent discoveries of topologically non-trivial complex spin structures [1] emerging from a superposition of magnetic ordering in several k directions sparked research interest in RE-Cu materials: HoCu, ErCu and TmCu, known to magnetically order in multiple-k direction [2].

1.1.1 Multi-k structures

An important example for complex magnetic structures are multi-k forms of order, alluding to their multiple Fourier components. A spin structure $m(r)$ is considered as a continuous field of multiple components of the magnetisation.

$$m(r) = \sum_i \vec{\mu}_i \cos\left(k_i r + \phi_i\right) \tag{1.1}$$

It is an alternative to defining a magnetic unit cell which is equally universal and natural. Moreover, it is advantageous for symmetry analysis and numerical calculations [3]. Figure 1.1 illustrates a classification of magnetic structures according to their propagation vectors. Firstly, one can distinguish the ferromagnetic (FM), antiferromagnetic (AFM) or incommensurate (modulated) structure.

For a FM $k_i = 0$, for an AFM k_is are rational fractions, while modulated structures generally have a modulation wavelength much larger than the lattice constant, $1/k_i \ll a$. Prominent modulated structures with a single propagation vector are the sine-wave, cycloid, helix and cone. A superposition of several such structures can yield complex textures, e.g. skyrmions.
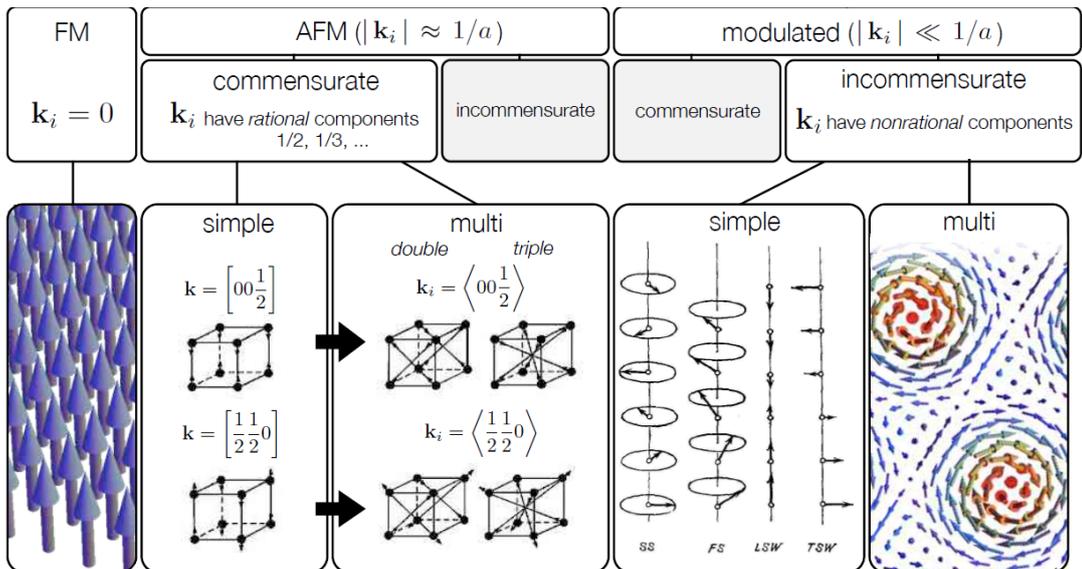
Figure 1.1: General interpretation of magnetic structures in terms of propagation vectors of the magnetic order. [4]

1.1.2 Skyrmions in magnetic structures

The identification of the so-called A-phase in the itinerant helimagnet MnSi [1] was the first example of a skyrmion lattice in a bulk solid state system. At intermediate fields $(100 - 200)$ mT, just below the helimagnetic transition temperature $(29\,\mathrm{K})$, three helices superimpose at $120°$ form topologically non-trivial spin whirls called skyrmions. They arrange in a regular hexagonal lattice in a plane perpendicular to the applied field (Fig. 1.2). Following the theoretical concepts from nuclear physics [5], one interprets these solitons as quasi-particleswith a topological charge or winding number, describing the underlying spin structure.
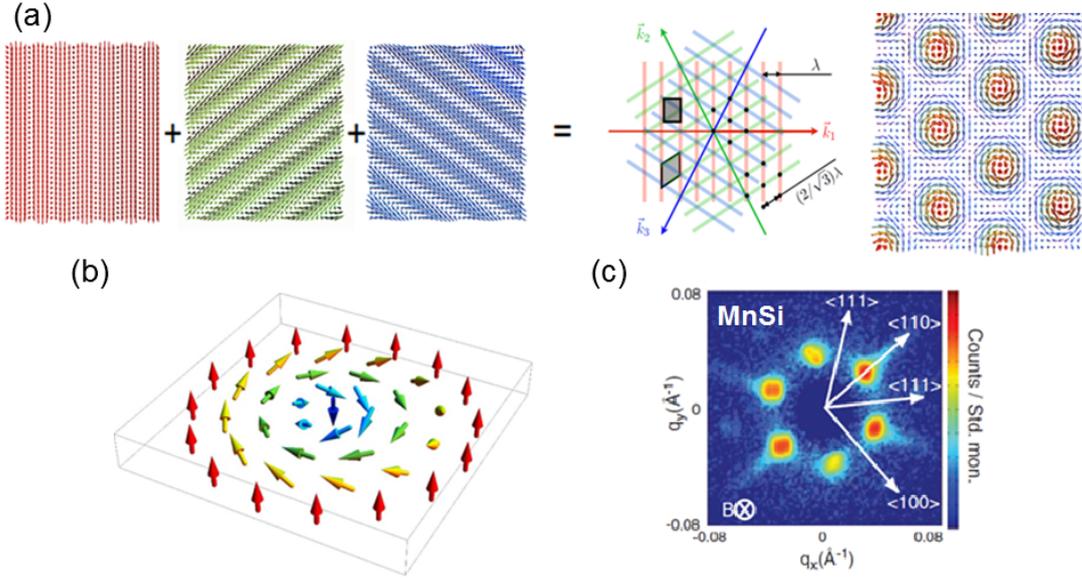
Figure 1.2: Superposition of three k-vectors resulting in the skyrmion lattice (a), real space single skyrmion (b) and the six-fold small-angle neutron scattering pattern observed in the "A-phase" of MnSi (c). [1]

MnSi crystallises in a non-centrosymmetric B20−type structure. The lack of inversion symmetry [6] results in the anisotropic exchange coexisting with an itinerant FM exchange. The third in the hierarchy of magnetic interactions is a weaker interaction with the crystal electric field (CEF). Dzyaloshinskii [7] and Moriya [8] proposed a model for the anisotropic exchange $\hat{H}_{DM} = \vec{D}\left(\vec{S}_1 \times \vec{S}_1\right)$, favouring skew spin arrangements for a finite vector $\vec{D}$ which emerges only if the underlying system lacks inversion symmetry. Dzyaloshinskii-Moriya (DM) energy is a standard origin of helical magnetism, which can result in stability of structures with a strong gradient of the moment modulus, such as skyrmions, in the presence of local fluctuations.

Except for MnSi, skyrmions were found in some isostructural B20−alloys, such as $Mn_{1-x}Fe_xSi$ [9], FeGe [10], FeCoSi [11] and Cu_2OSeO_3 [12], which all have the same cubic chiral space group $P2_13$, but recently also at room temperature in Co-Zn-Mn compounds, crystallising in a β-Mn-type structure which belongs to another cubic chiral space group $P4_132$ or $P4_332$ [13].

Probing non-trivial topology

There are several probes of non-trivial topology: neutron scattering, the Hall effect, scanning tunnelling microscopy (STM), magnetic force microscopy (MFM), Lorentz transmission electron microscopy (L-TEM), etc. The first two techniques are regularly practised in our group. Though the neutron scattering measurements give more direct information on the present orderings, they are costly and time-consuming, so the primary crucial experimental probe is the Hall effect. The Hall data is interpreted by a theoretical model where ρ_{xy}^n, ρ_{xy}^a and ρ_{xy}^{top} represent the normal, anomalous and topological contributions as shown in Figure 1.3 (a). Topological Hall effect contribution in the A-phase of MnSi is represented in Figure 1.3 (b). Topological resistivity is proportional to spin canting in real space which is connected with Berry curvature (Appendix A).

(a)

$$\rho_{xy} = \rho_{xy}^N + \rho_{xy}^A + \rho_{xy}^{top} =$$
$$= R_0 H + R_S M + P \cdot R_0 \cdot B_{\text{eff}}$$

(b)
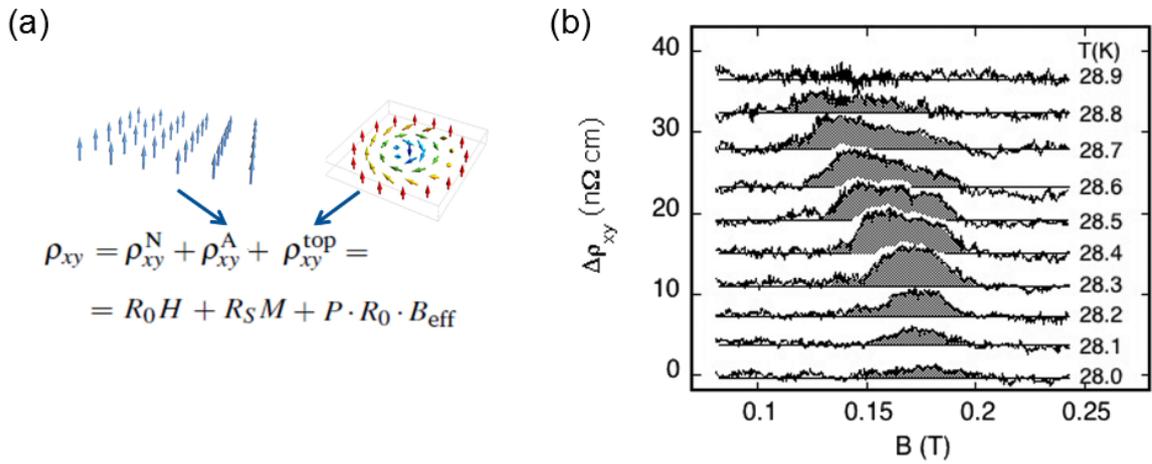
Figure 1.3: Hall effect contributions associated with schematics of the anomalous and the topological contribution. The proporionality of Berry curvature to the topological Hall effect is displayed (a). Additional Hall contribution after subtracting the normal and anomalous Hall contribution in the A-phase of MnSi. Data are shifted vertically for better visibility (b). [14]

1.2 Rare-earth copper compounds (RE-Cu)
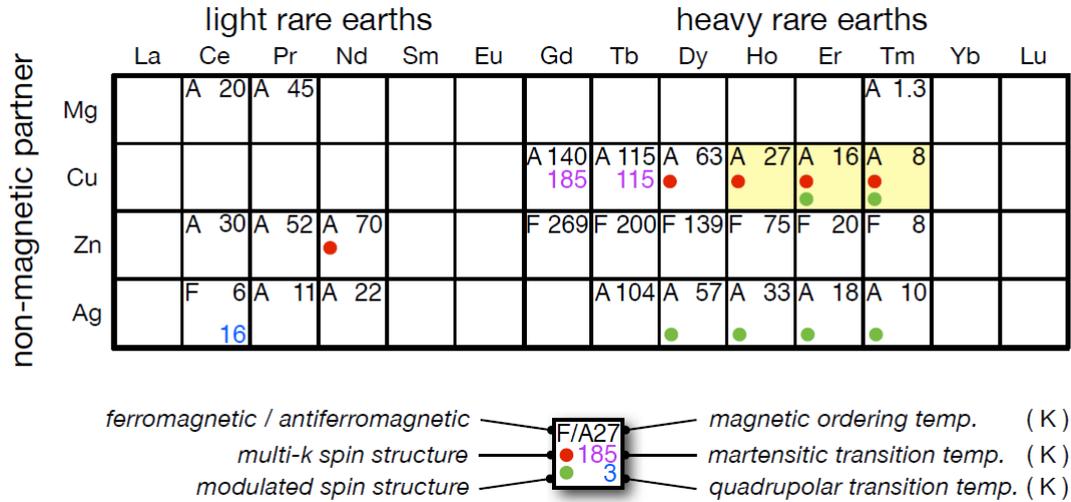
Figure 1.4: Overview of some rare earth intermetallic compounds, cf. review by Morin and Schmitt. [2] Red dots mark compounds hosting multi-k magnetic orderings.

The discovery of skyrmions sparked research interest in other materials with multi-k magnetic ordering. Extensive results on the rare earth intermetallic compounds by a group of Morin, Pierre and Schmitt from the 1970s [2] can indicate the possible hosts of non-trivial topological structures. In Figure 1.4, materials in which multi-k magnetic ordering is present are marked with a red dot.

We focused on the cubic rare earth intermetallics RE-Cu, (RE = Ho, Er, Tm). They order antiferromagnetically in the temperature range (7-27) K, and display strong electronic correlations and large magnetic anisotropies. These anisotropic systems are of particular interest due to a strong interplay of spin and orbital degrees of freedom, hence supporting the Berry curvature principle.

1.2.1 Crystal structure and magnetic moment

The rare-earth intermetallics chosen for investigation are isoatomic binary compounds of rare-earths (RE) and copper. The electron configurations of the studied rare-earths are $[Xe]4f^{11}6s^2$, $[Xe]4f^{12}6s^2$ and $[Xe]4f^{13}6s^2$ for Ho-, Er- and Tm atoms, respectively. Xe electron configuration is $[Kr]4d^{10}5s^25p^6$. The radial distribution of the atomic orbitals 4f, 5s, 5p and 6s shows that the incomplete 4f shell of RE lies well shielded beneath the Xe orbitals (Fig. 1.5 (a)). The expected value of 4f shell radius is smaller than the expected values of radii of the 5s and 5d shells. Therefore, the RE atoms can be considered chemically identical. In the RE-Cu compounds, the rare-earth ions are approximately in a 3+ state leading to electron configurations $[Xe]4f^{10}$, $[Xe]4f^{11}$ and $[Xe]4f^{12}$ for Ho^{3+}, Er^{3+} and Tm^{3+} ion respectively. To a good approximation,

the variation of physical properties of RE-Cu compounds reflects only the change in the magnetic moment of the 4f state. They crystallise in a CsCl-type crystallographic structure of high symmetry, as shown in Figure 1.5 (b).
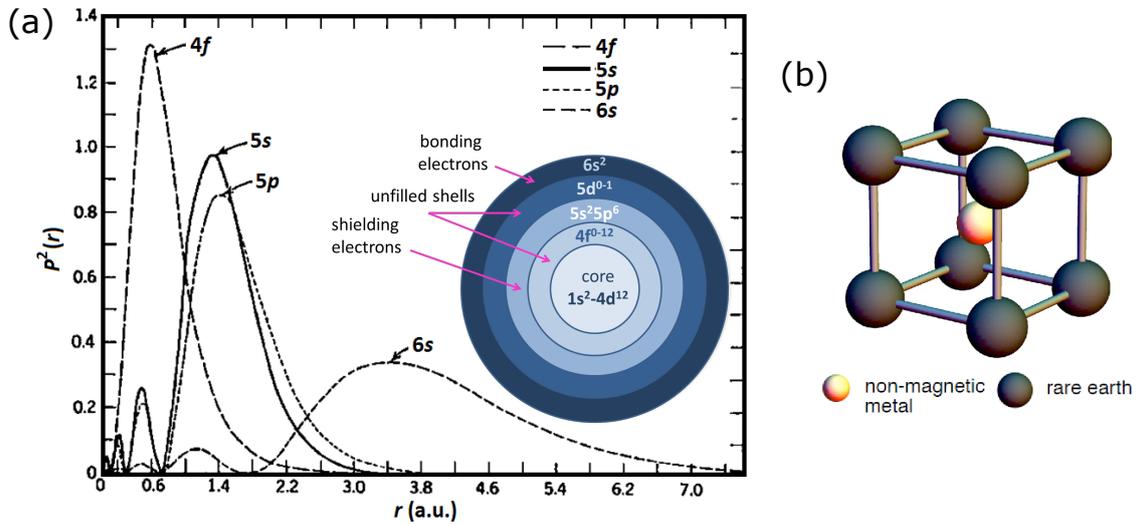
Figure 1.5: Radial probability function of 4f, 5s, 5p and 6s atomic orbitals. A graphic inset shows their usual role in lanthanides (a). Figure adapted from [15]. Highly symmetric CsCl-type crystal structure of studied rare earth intermetallics (b).

A summary of crystallographic and magnetic properties of investigated materials is given in Table 1.1. All compounds have a similar lattice parameter but differ in the measured magnetic moment. The last row shows the magnetic moment according to Hund's rules which apply when the repulsion between the outer electrons is much greater than the spin-orbit interaction, which is stronger than the remaining interactions.

An agreement is identifiable for HoCu and TmCu whereas ErCu displays a lower magnetic moment than theoretically predicted. The latter might be assignable to the influence of crystal electric field (CEF).

compound	HoCu	ErCu	TmCu
a(Å) [16]	3.447	3.431	3.415
$\mu_{eff}(\mu_B)$ [17]	10.73	6.83	7.56
RE^{3+} conf.	$4f^{10}$	$4f^{11}$	$4f^{12}$
$g_J J$ by Hund's rules	10	9	7

Table 1.1: Crystallographic and magnetic properties of investigated materials. [18]

1.2.2 Interactions

The scientific interest in RE-Cu (RE = Ho, Er, Tm) persisted due to the identification of multiple phase transitions below the antiferromagnetic ordering temperature [2]. They manifest some unusual physical phenomena such as multi-step magnetism, strong electronic anisotropy, multi-axis spin structures and complex magnetic phase diagrams [4].

These observations can be mediated by a number of competing interactions along with the crystal electric fields (CEF):

- The Ruderman-Kittel-Kasuya-Yosida (RKKY) [19] theory provides means of estimating the magnetic ordering temperature of the RE-Cu compounds. The magnetic moment of the strongly localised RE 4f orbitals is assumed to spin-polarise the delocalised 4s electrons of the Cu atoms. In the simple model, a spatially oscillating exchange constant $J(r)$ is identified

$$J(r) = \frac{1}{r^3} \cos k_f r \tag{1.2}$$

  The systematic comparison of the RKKY predictions with the experiment showed qualitative agreement at most.

- The indirect exchange takes into account the influence of the RE 5d shells. Contrary to the isolated picture of 4f shells in the RKKY model, Campbell [20] argues that the intra-atomic coupling of 4f and 5d RE electrons could enable a direct 5d-5d coupling, favouring a ferromagnetic alignment of the spins.

- The third influence that needs to be taken into account is the CEF of the d orbitals of the Cu site. The crystal electric field operators for a cubic system comprising d and f electrons can be rewritten in the effective Hamiltonian [21]

$$\hat{H} = A_4 \beta(r_4) O_4 + A_6 \gamma(r_6) O_6 \tag{1.3}$$

  where $A_4\beta(r_4)$ and $A_6\gamma(r_6)$ are functions of the total angular momentum of the fourth and the sixth order respectively.

  The fourth order contribution measures the extent of d electrons delocalisation. Smaller $A_4\beta(r_4)$ values indicate localised d electrons leading to a stronger deformation of RE orbitals.

  According to the CEF level schemes, the magnetic moment aligns along the principal axes of the cubic system, $\langle 100 \rangle$, $\langle 110 \rangle$ and $\langle 111 \rangle$. Furthermore, the magnetic hardness of the system may vary with temperature, but in zero-field at zero temperature the easy axis is predicted to be the $\langle 110 \rangle$ axis.

- Secondary effects stabilising certain magnetic structures are the complexity of the band structure [22], the quadrupolar exchange of 4f orbitals [23], [24] and the magnetoelastic coupling [25].

Though a hierarchy of magnetic interactions is not yet established, the stated aspects imply that the magnetic moment is confined to principal symmetry directions due to crystal electric fields. There exists a large number of equivalent directions (e.g. eight for $\langle 111 \rangle$ direction) among which the most favourable depends on the secondary interactions, such as the quadrupolar exchange. Unlike the non-centrosymmetric B20- and β-Mn-type skyrmion-hosting compounds, allowing the Dzyaloshinskii-Moriya (DM) interaction, the RE-Cu compounds are centrosymmetric, so the spin-skewing would arise from the mentioned secondary contributions.

1.2.3 Previous studies

Comparative studies of HoCu - ErCu - TmCu, conducted by Morin et. al from the mid-1970s onward, attempted to characterise the magnetic ordering by neutron powder diffraction and specific heat measurements. In all three compounds, they observed a $k = \langle \frac{1}{2} \frac{1}{2} 0 \rangle$-type antiferromagnetic ordering [26]. Previous reports on heat capacity by Morin et al. and Ho [27] were both limited to polycrystalline samples and zero magnetic fields.

The results for ErCu (Fig. 1.6) showed two anomalies: one at $10.9\,$K, a first-order phase transition, and another at $13.8\,$K, a second-order phase transition, the Néel temperature. These two transitions overlap making the analysis dubious. This ambiguity could be a result of samples being polycrystalline, the purity of starting elements in the synthesis or the density of data points.
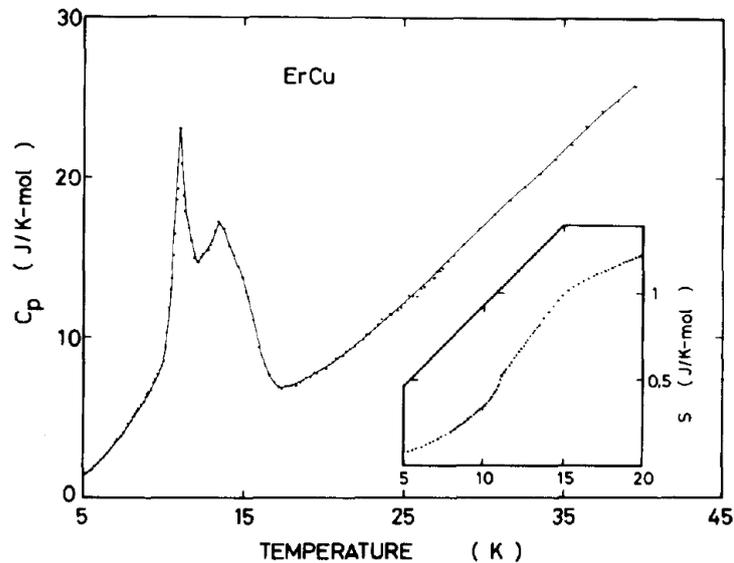
Figure 1.6: Specific heat of ErCu as a function of temperature, the inset is the integrated entropy over temperature. [26]

Neutron time-of-flight spectroscopy on magnetically diluted RE-Cu was used to extract the specific CEF parameters; the results are presented in Table 1.2. The fourth order coefficient in ErCu is larger than the one in HoCu indicating more delocalised

d electrons. In terms of magnetic anisotropy, the hard axis was found to be the $\langle 100 \rangle$ axis, which is in discord with the later bulk measurements. This signifies that there are further significant interactions except the CEF, which in competition and interplay with CEF lead to changes of the magnetic easy axis with temperature and field.

compound	HoCu [28]	ErCu [29]
$A_4\beta(r_4)(K)$	-68 ± 8	-84 ± 7
$A_6\gamma(r_6)(K)$	-15 ± 1	-15 ± 1

Table 1.2: Crystal electric field parameters in HoCu and ErCu.

From the measured neutron scattering spectra, several potential magnetic structures were suggested. At $1.5\,\mathrm{K}$, the magnetic moment of the proposed multi-k structure would be at $60°$ angle to the $\langle 100 \rangle$ axis (Fig. 1.7). The magnetic ordering at $12\,\mathrm{K}$ is along the $\langle 100 \rangle$ axis (Fig. 1.8).
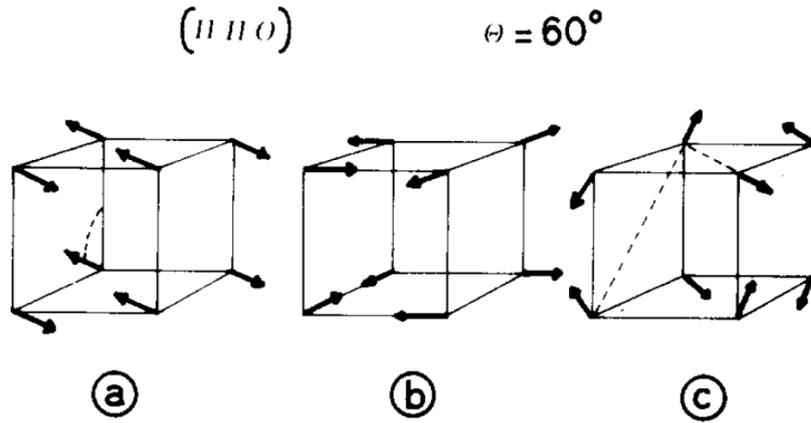
Figure 1.7: Possible ground state magnetic orderings in the $\langle \frac{1}{2}\ \frac{1}{2}\ 0 \rangle$ direction with $\Theta = 60°$ to the $\langle 100 \rangle$ axis, a single-k (a) and double-k structures (b), (c). [26]
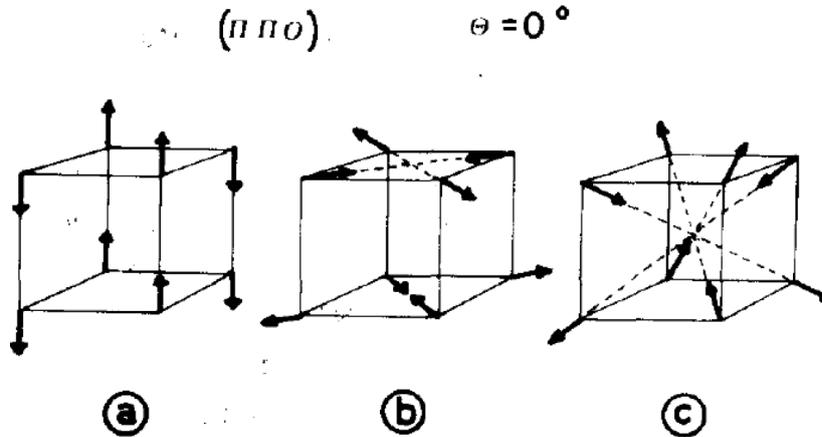
Figure 1.8: Possible magnetic orderings in the $\langle \frac{1}{2}\ \frac{1}{2}\ 0 \rangle$ direction with $\Theta = 0°$ to the $\langle 100 \rangle$ axis, a single-k (a), a double-k (b) and a multi-k structure (c). [26]

Except for this commensurable ordering, another incommensurable structure with the propagation vector $k = \langle 0.54\ 0.5\ 0 \rangle$ was observed. The lower-temperature lying phase transition is assumed to be a transition from the commensurable to the incommensurable structure. This is in agreement with the theoretical calculations [30] which predicted a commensurate ground state and an incommensurable modulated magnetic structure just below the Néel temperature. The powder diffraction leaves open the possibility of a collinear structure in one, two or all three $\langle \frac{1}{2}\ \frac{1}{2}\ 0 \rangle$ directions.

Magnetostriction measurements were performed by Ibarra et al. [31] attributing the full structural phase transitions to magnetic reorderings, unlike in the lighter RE-Cu compounds.

There are two reports on the transport properties of polycrystalline RE-Cu in which the precision of experiment did not allow a detailed resolution of the ordered regime [32], [33]. A large positive magnetoresistance is visible in the antiferromagnetic regime.

1.3 State of the art

Previous efforts to study these materials were dedicated to the construction of magnetic phase diagrams by bulk measurements and the clarification of the magnetic structures by neutron diffraction and spectroscopy. Their endeavours were limited by polycrystalline samples.

In this group, the first high-quality RE-Cu single crystals were grown using optical floating zone by M. Wagner [34]. An example of an ErCu crystal and its Laue image is given in Figure 1.9. Samples were cut along the crystallographic axes of interest for bulk and neutron scattering characterisation.

ErCu - OFZ 104

Laue||110

Cutoff = 2, Number of Points 0

Figure 1.9: ErCu crystal prepared using optical floating zone technique with its Laue image in $\langle 110 \rangle$ direction.

They were investigated in this group as a part of the master thesis of M. Rahn [4], the bachelor thesis od H. Hautmann [35] and the doctoral studies of W. Simeth. Resistivity, magnetisation and ac-susceptibility measurements were performed with the field applied along the high-symmetry axes of the system.

1.3.1 Transport properties

Transport measurements were performed on HoCu with current along the $\langle 100 \rangle$ and $\langle 210 \rangle$ directions and a magnetic field parallel to the crystallographic $\langle 110 \rangle$ and $\langle 111 \rangle$ directions, respectively [4], both as magnetic field- and temperature sweeps. The resistivity with current along the $\langle 100 \rangle$ direction and field along the $\langle 110 \rangle$ direction is presented in Figure 1.10 (a). Hall effect investigations in rare earth intermetallics are scarce, and these measurements seem to be the first on the CsCl-type compounds.

The measured Hall resistivity for temperature sweeps in Figure 1.10 (b) is anisotropic, changes sign as a function of temperature, is non-monotonic as a function of the field and attains absolute values of almost $2\,\mu\Omega$cm at low temperatures. This is at odds with the linear characteristic of magnetisation and indicates a topological contribution. To quantify the potential topological contribution, the normal and anomalous Hall effect were first assessed and then subtracted.

The classical Hall constant was deduced from a linear fit to high-temperature field-sweeps and is assumed to be constant with temperature. The anomalous Hall effect scales with magnetisation and the square of resistivity. The subtraction was analysed in detail and performed in the master thesis of M. Rahn [4]. The topological contribution was found to be 500 times larger than the topological contribution in MnSi, a compound hosting skyrmions [14].

A larger topological resistivity indicates a smaller lattice size for the underlying structure. The effective field of the topological spin structures scales with the inverse square of the lattice spacing. Computer calculations of allowed multi-k magnetic structures in these materials were carried out by M. Rahn, and the results are given in Appendix B.
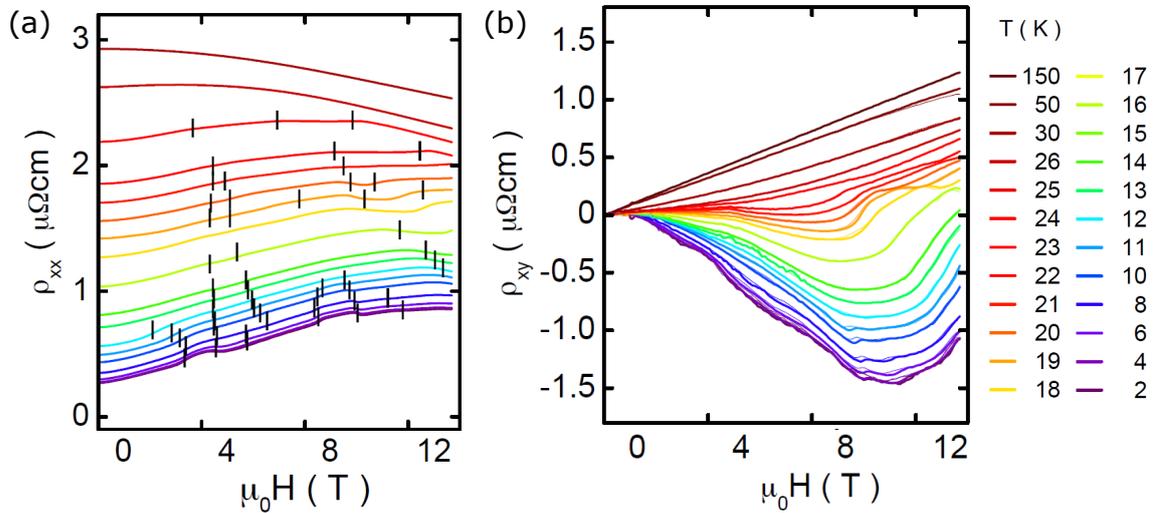
Figure 1.10: HoCu resistivity with magnetic field along the $\langle 110 \rangle$ direction with marked anomalies (a). Hall effect measurements in HoCu with a very large topological contribution (b). [4]

1.3.2 Magnetisation and ac-susceptibility

Magnetisation and ac-susceptibility measurements on ErCu were carried out by H. Hautmann and the results are presented in Figure 1.11 and Figure 1.12. For various sample orientations, magnetic field sweeps from $0\,\mathrm{T}$ to $14\,\mathrm{T}$ and temperature sweeps were performed.

Features which were selected for constructing magnetic phase diagrams are indicated by black vertical markers. Data were analysed to obtain the Weiss temperature $24.57\,\mathrm{K}$. As a function of magnetic field, the magnetisation of ErCu shows a series of metamagnetic transitions varying in number and position for different sample orientations.
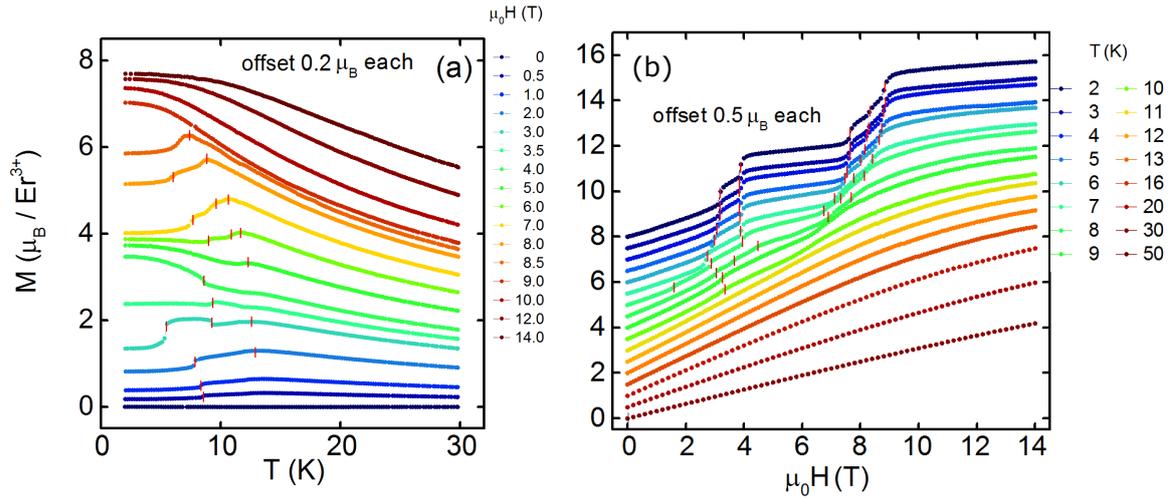
Figure 1.11: Magnetisation in ErCu with magnetic field along the $\langle 100 \rangle$ direction for temperature- (a) and magnetic field sweeps (b). [35]
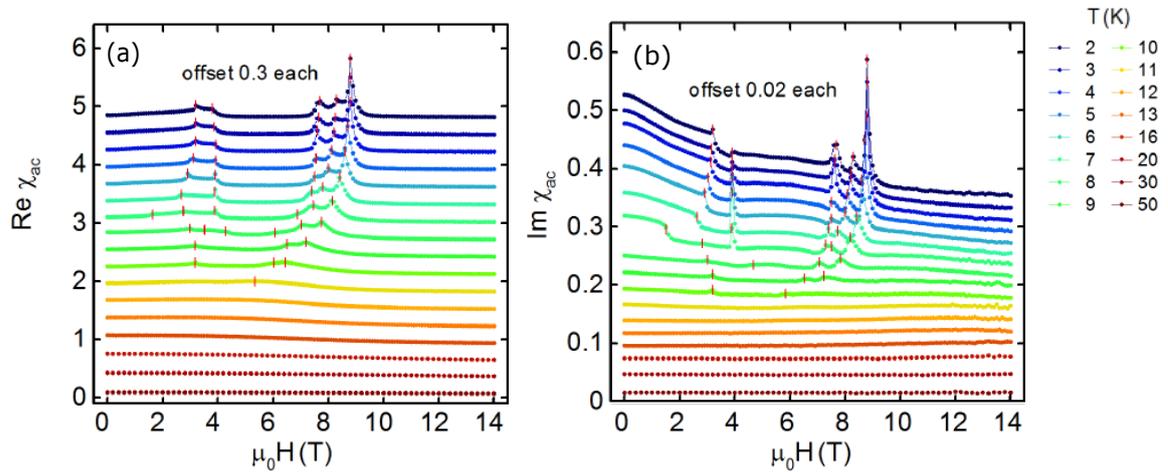
Figure 1.12: ErCu ac-susceptibility with magnetic field along the $\langle 100 \rangle$ direction for temperature- (a) and magnetic field sweeps (b). [35]

1.3.3 Phase diagrams

Partial magnetic phase diagrams were constructed from the tracked features in magnetisation and ac-susceptibility measurements (Fig. 1.13). The data revealed a great multitude of phases, strongly dependent on the direction of the applied field. A full mapping of the phase diagrams for HoCu, and ErCu in hard axes would require experiments with fields in excess of 20T.

Though these measurements produced immensely rich magnetic phase diagrams, some of the features tracked with these methods might not be of thermodynamic origin. A part of them could be magnetic reorderings with no associated energy change, or a single transition marked several times, at its beginning, the transition itself and its end.
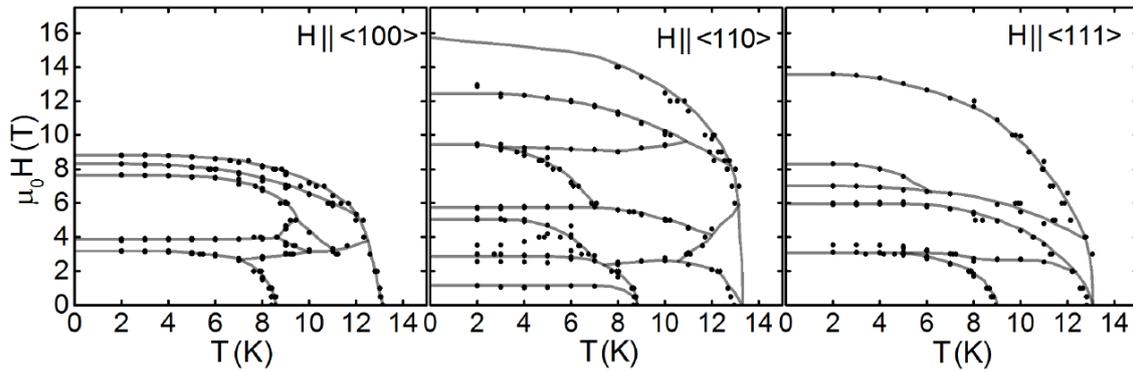
Figure 1.13: Phase diagrams of ErCu, constructed from anomalies in magnetisation and ac-susceptibility measurements. [35]

A more conclusive experimental probe from the thermodynamic point of view would be the heat capacity. This experiment was attempted during both the master thesis of M. Rahn and the bachelor thesis of H. Hautmann, but the issue of magnetic torque when measuring along the hard magnetisation axes rendered them futile with the Standard heat capacity setup.

1.4 Thermodynamics

Entropy and its derivatives, such as specific heat, play an important role in the study of phase transitions [36]. Entropy usually exhibits a step change across first order transitions leading to the absorption or release of heat, often called latent heat. Across second order transitions, entropy evolves continuously, but not smoothly, leading to discontinuities or divergences in its derivatives.

1.4.1 Entropy in magnetic systems

The first law of thermodynamics is a statement about the conservation of energy. For a purely magnetic system, it is mathematically expressed as

$$\mathrm{d}U = \Delta Q + \mu_0 H \mathrm{d}M \tag{1.4}$$

Here μ_0 is the magnetic vacuum permeability, H is the vacuum field and M the magnetisation.

The second law of thermodynamics is based on an observation that for any closed reversible path $\oint \frac{\Delta Q}{T} = 0$. A new thermodynamic function, entropy S is defined, whose differential is the above integrand. Its natural variables in a magnetic experiment are temperature T and magnetic field H. Its total differential can, therefore, be written as

$$\mathrm{d}S(T,H) = \left.\frac{\partial S}{\partial T}\right|_H dT + \left.\frac{\partial S}{\partial H}\right|_T dH \tag{1.5}$$

The first part describes the change of heat content upon a small temperature change at a constant field. It can be recognised as the heat capacity C_H of the system at a constant magnetic field, divided by temperature

$$\left.\frac{\partial S}{\partial T}\right|_H dT = \left.\frac{C_H}{T}\right|_H \tag{1.6}$$

Similarly, one can measure the magnetocaloric coefficient Γ as the change of entropy while changing the magnetic field at a constant temperature

$$\left.\frac{\partial S}{\partial H}\right|_T dT = \left.\frac{\Gamma}{H}\right|_T \tag{1.7}$$

The third law of thermodynamics states that at zero temperature all thermodynamic systems have the same entropy, to be defined as zero. It should be noted that the first and the second law of thermodynamics allow us to write the magnetic version of one of Maxwell's relations, leading to

$$\lim_{T\to 0}\frac{\partial S}{\partial H} = \lim_{T\to 0}\frac{\partial M}{\partial T} = 0 \tag{1.8}$$

Entropy links theoretical predictions of microscopic models with the experimentally accessible quantities of thermodynamics via the postulate that the entropy of a system with N accessible microstates is given in the microcanonical ensemble $S = k_B \ln N$. For a magnetic system with magnetic moment J, this can be rewritten as

$$S = k_B \ln\left(2J + 1\right) \tag{1.9}$$

Reconstructing the entropy of a system by specific heat measurements

It is theoretically possible to reconstruct the entropy of a system over the whole phase diagram by only measuring the specific heat $C(H,T)$ as a function of the appropriate magnetic field and temperature. One can write in principle

$$S(H_1, T) - S(H_0, T) = \int_0^T \left\{ \frac{C(H_1, T') - C(H_0, T')}{T'} \right\} \mathrm{d}T' \qquad (1.10)$$

Still, it is impossible to measure C at zero temperature, and one has to extrapolate down to zero. This method breaks down close to low temperatures where magnetocaloric effect gains importance. The calculated entropy values can commonly be just qualitatively compared due to an influence of the measurement technique on the exact specific heat values at phase transitions.

1.4.2 Specific heat

Specific heat represents the amount of energy needed to raise the temperature of a known quantity of a material by one degree. It is defined as

$$C_H = T \frac{\partial S}{\partial T}\bigg|_H \qquad (1.11)$$

which is in practice modified to

$$C_H = \frac{\Delta Q}{\Delta T}\bigg|_H \qquad (1.12)$$

for the static measurement where ΔQ is the amount of heat introduced into a calorimeter during a heat pulse and ΔT is the resulting temperature rise. Alternatively, heat capacity is defined as the inverse change of the slope of the response function $\mathrm{d}T/\mathrm{d}t$ times an applied power $P(t)$

$$C_H = \frac{P(T)}{\mathrm{d}T/\mathrm{d}t}\bigg|_H \qquad (1.13)$$

Measuring heat capacity provides key information on the phase transitions, revealing the nature of excitations and changes of entropy across the phase boundaries and therefore is directly linked to the free energy functional of the system.

Specific heat is an important material property which gives information about its phononic, electronic and magnetic properties [37]. In general, they give independent contributions to heat capacity.

$$C = C_{ph} + C_{el} + C_{mag} \qquad (1.14)$$

Phononic contribution

The phononic contribution C_{ph} can be described by the Debye model for most solids. The vibrations of the atomic lattice are treated as phonons in a box. In general, the internal energy E_{ph} of an ensemble of phonons as a function of their characteristic frequencies is

$$E_{ph} = \frac{h}{2\pi} \int D(\omega) n(\omega) \omega \mathrm{d}\omega \tag{1.15}$$

$D(\omega)$ is the phonon density of states, describing the fraction of phonons that occupy a particular energy level characterised by its frequency ω. The Debye model assumes that the density of states is described by a continuum ω^2 dependence up to a characteristic frequency ω_D, referred to as the Debye frequency. The function $n(\omega)$ is the statistical distribution function, the Bose-Einstein statistics

$$n(\omega) = \frac{1}{e^{h\omega/2\pi k_B T} - 1} \tag{1.16}$$

with $h = 6.63 \times 10^{-23}$ Js is the Planck's constant. Inserting the Debye density and the distribution function, a solution for the internal energy of phonons reads

$$E_{ph}(T) = 9 N k_B \left(\frac{T}{\Theta_D}\right)^3 \int_0^{\Theta_D/T} \frac{x^3}{e^x - 1} \mathrm{d}x \tag{1.17}$$

where $x = h\omega/2\pi k_B T$. The Debye temperature is defined concerning the maximum phonon frequency, ω_D

$$\Theta_D = \frac{hc}{2\pi k_B} \left(6\pi^2 \frac{N}{V}\right)^{1/3} \tag{1.18}$$

where c is the speed of sound in the material and N/V the number of molecules per unit volume. For most solid materials, the Debye temperatures range from $100\,\mathrm{K}$ to $1000\,\mathrm{K}$ The specific heat can be calculated directly by differentiating the internal energy in Eq. (1.16) with respect to temperature

$$C_{ph}(T) = 9 N k_B \left(\frac{T}{\Theta_D}\right)^3 \int_0^{\Theta_D/T} \frac{x^4 e^x}{(e^x - 1)^2} \mathrm{d}x \tag{1.19}$$

where x is temperature scaled by the Debye temperature. At temperatures substantially below the Debye temperature ($T \ll \Theta_D$), the specific heat has a cubic temperature dependence

$$C_{ph}(T \ll \Theta_D) = \beta T^3 = \frac{12\pi^4}{5} N k_B \left(\frac{T}{\Theta_D}\right)^3 \tag{1.20}$$

In the high-temperature limit, the phononic contribution saturates at a constant value, known as the Dulong-Petit law.

$$C_{ph}(T \gg \Theta_D) = N k_B \approx 25\,\mathrm{JK}^{-1} \tag{1.21}$$

By the equipartition theorem, the specific heat of solids approaches a maximum of $3R$ per mole of atoms. The three vibrational-mode degrees of freedom each corresponds to a quadratic kinetic- and potential energy term, an average of each giving

a $1/2k_BT\,\text{mol}^{-1}$ in energy. This model is fairly accurate, although it does not take anharmonicity into account which gives further rise to heat capacity.

Thermal expansion is due to anharmonicity of atom interactions [38]. As a result, the measured specific heat at constant pressure C_P does not equal the specific heat at constant volume C_V as derived in the Debye model and the Dulong-Petit prediction. Starting from the fundamental thermodynamic relation one can show

$$C_P - C_V = T\frac{\partial P}{\partial T}\bigg|_V \frac{\partial V}{\partial T}\bigg|_P \qquad (1.22)$$

This can be rewritten regarding the coefficient of thermal expansion α and the isothermal compressibility β_T.

$$C_P - C_V = VT\frac{\alpha^2}{\beta_T} \qquad (1.23)$$

This shows that at temperatures significantly above the Debye temperature, a linearly increasing value of specific heat, higher than the saturation Dulong-Petit value, is expected.

Electronic contribution

For metals at low temperatures, $T < 10\,\text{K}$, there is an additional contribution due to the energy contained in the conduction electrons. The internal energy of the electron gas E_e is analogous to the Eq. 1.14

$$E_e = \int D(\epsilon)f(\epsilon)\epsilon\,\mathrm{d}\epsilon \qquad (1.24)$$

The density of states in the free-electron model is

$$D_e = \frac{V}{2\pi^2}\left(\frac{m}{2\pi^2}\right)^{3/2}\epsilon^{1/2} \qquad (1.25)$$

The electrons obey the Fermi-Dirac statistics

$$n(\epsilon) = \frac{1}{e^{(\epsilon-\mu)/k_BT} + 1} \qquad (1.26)$$

where μ is the chemical potential, approximately equal to the Fermi energy E_F at lower temperatures. The Fermi energy in the free-electron model is defined in terms of the total number of free electrons per unit volume, $n = N_e/V$

$$E_F = \frac{h^2}{8\pi^2 m_e}\left(3\pi^2\frac{N_e}{V}\right)^{2/3} \qquad (1.27)$$

where m_e is the mass of an electron equal to 9.11×10^{-31} kg. The characteristic Fermi temperature is $T_F = E_F/k_B \approx 10^4$ K.

In the simplest electron model of a Fermi liquid, the electronic contribution to specific heat is linear and dominates for low temperatures

$$C_{el}(T) = \gamma T = \frac{\pi^2 n k_B^2}{2E_F}T \qquad (1.28)$$

with the Sommerfeld coefficient $\gamma = \frac{1}{3}\pi^2 D(E_F)k_B^2$, the electron density at the Fermi level n and the Fermi energy E_F.

Magnetic contribution

The magnetic contribution to heat capacity depends on the magnetic ordering. The specific heat of a FM is generally proportional to $T^{3/2}$ while the AFM ordering gives a T^3 dependence [39]

$$C_{AFM}(T) = \zeta T^3 = z \left(\frac{k_B T}{JS} \right)^3 k_B \qquad (1.29)$$

The coefficient of this temperature dependence ζ in inversely proportional to the cube of the product of the magnetic moment J and the spin S state of the magnetic ions, z is a numeric factor depending on the specific crystal and magnetic structure. In the case of strong spin-orbit coupling, S is no longer a good quantum number.

One way to extract the magnetic contribution is to measure an equivalent non-magnetic compound. Its specific is subtracted from the specific heat of a magnetic compound to account for the phononic and the simple electronic part. This approach was followed in this study by preparing a LuCu sample and measuring its specific heat.

An overall expression for the specific heat low-temperature dependence reads

$$C = C_{ph} + C_{el} + C_{mag}$$
$$C(T \ll \Theta_D) = \beta T^3 + \gamma T + \zeta T^3 \qquad (1.30)$$

1.4.3 Phase transitions

Magnetic phase transitions appear as anomalies in heat capacity, but there is no universal mathematical expression for their description [40]. They are hence discussed in a basic classification of first-order and second-order phase transitions. First-order phase transitions are those that involve latent heat while the second-order phase transitions are continuous.

Clausius-Clapeyron relation is often considered in PVT systems, relating the curvature of the first order phase transition line in the $P - T$ diagram is connected to the ratio of entropy S and volume V differences between two coexisting states at P_C and V_C.

The analogous expression for a magnetic transition is

$$\mu_0 \frac{\mathrm{d}H_C}{\mathrm{d}T_C} = -\frac{S_2 - S1}{M_2 - M_1} \qquad (1.31)$$

the $\mu_0 \mathrm{d}H_C/\mathrm{d}T_C$ is the curvature of the first order transition line in the $H - T$ plane of the phase diagram. Therefore, detailed magnetisation measurements are capable of ruling out the change of entropy during a first order transition [41], [42].

The curvature of the phase transition line at zero temperature has to be zero since ΔS equals zero according to the third law of thermodynamics while ΔM is generally not zero.

1.5 Aim of the thesis

The major goal of this thesis is **developing a mechanically stable calorimeter** for systems with complex magnetic phase diagrams in finite magnetic fields since strong magnetic torques prevent measurements along hard magnetisation axes.

- **Design, construction and characterisation**

  To overcome the issue of magnetic torque, new designs to measure heat capacity are to be invented, constructed and characterised in detail. Such an experimental setup has opposing requirements on the experimental setup. The addenda signal is to be minimised, but mechanical solidity is essential to prevail against the resulting forces.

  All parts of the setup should be chosen with care regarding their material, size and shape. The resulting thermal properties ought to be calculated so that the time constants are available and appropriate.

- **Optimisation**

  The new calorimeter, fitting to a commercially available sample puck provided by the Physical Property Measurements System (PPMS) from Quantum Design, needs to be compared to the conventional heat pulse calorimeter technique. PPMS has an accompanying software for controlling the measurement procedure, acquiring and processing the data.

  A suitable measurement method is to be optimised in respect to the particular materials and verified using the present-day apparatus in zero-field.

- **Validation**

  The applicability and reliability of the new setup are to be tested with a sample of known specific heat. Experimental error and its cause should be estimated and explained.

This thesis aims at **investigating RE-Cu compounds**, as possible hosts of topologically non-trivial spin structures. The studied rare earth intermetallics have multiple-k antiferromagnetic orderings in the temperature range (7-27) K.

- **Thermodynamic properties in magnetic field**

  There is no consensus on the hierarchy of numerous interactions competing and interplaying in these materials, but one main outcome is the magnetic anisotropy. Crystal electric fields (CEF) imply that the magnetic moment is confined to principal symmetry directions with a number of equivalent directions among which the most favourable depends on the secondary interactions.

19

They predict the $\langle 110 \rangle$ direction to be the easy axes of the system which is in disagreement with the bulk measurements. The most prominent candidate among the secondary interactions to take precedence over CEF in magnetic field is the quadrupolar exchange.

To study the relationship of different interactions, it is important to conduct direction-dependent measurements of underlying energy changes and confirm or disprove the earlier results. On that ground, the primary objective of this thesis is to measure thermodynamic properties in magnetic field along the three principal crystallographic axes.

- **Analysis of phase diagrams and anomalies**

    Previous measurements of magnetisation and ac-susceptibility produced immensely rich magnetic phase diagrams. Some of the features tracked with these methods might be magnetic reorderings with no associated energy change, or a single transition marked several times, at its beginning, the transition itself and its end.

    For this reason, heat capacity would be the deciding experimental probe from the thermodynamic standpoint which could lead to the simplification of phase diagrams. It would also indicate the phase transition order in examining the shape of features in heat capacity measurements.

- **Magnetic entropy evaluation**

    Entropy connects microscopic models with macroscopic quantities of thermodynamics and provides information on the underlying changes across the phase boundaries. It can be reconstructed from specific heat measurements as a function of the appropriate magnetic field and temperature.

    To evaluate magnetic entropy, one has to separate different contributions to specific heat. A non-magnetic equivalent of the RE-Cu materials is to be prepared to account for the phononic- and simple electronic contribution.

2 Experimental methods

Heat capacity measurements distinguish the thermodynamic transitions, reveal their nature and their relative size to other contributions, but also give information on the entropy in the system. The original principle of measuring the specific heat was investigating the change of temperature after supplying a well-defined amount of energy, the so-called adiabatic measurement. Since the 1960s, other methods have been developed, in which the sample is not completely isolated, such as the relaxation time and the ac-method [43].

I will focus on the method used in the Physical Property Measurements System (PPMS) from Quantum Design, which is the relaxation-time method with a possibility to process the pulses as if measured with the adiabatic method.

In magnetic materials for measurements along the hard magnetisation axes in finite fields, a strong mechanical torque prevents gathering information on heat capacity with present-day apparatus. New experimental setups for overcoming this issue were realised in this study.

Setup-independent heat capacity considerations of RE-Cu materials are presented in section 2.1. It is followed by a description of the Physical Property Measurement System (PPMS) in section 2.2, the development of the new setups in section 2.4 and an analysis of the new setups' performance in section 2.4.

In the first setup-independent part of the study, measurements were conducted on the HoCu compound since it is the most investigated of the three sister-compounds. HoCu measurements were interrupted due to irradiation of the sample during neutron scattering measurements. The study continued on the ErCu sample which became the central compound of the thesis and was used for verification of the setup in section 2.4.

2.1 Measurement techniques to determine the heat capacity

In Figure 2.1, a schematic and a photograph of the Heat Capacity Option in the PPMS are represented. To measure the heat capacity, one has to apply heat to the system in a controlled way via a heater and measure the temperature response of the sample via a thermometer. The temperature of the thermal bath is supposed to be constant. The measurement system is characterised by its heat capacity and the thermal conductance of the thermal link as derived in the following subsection.
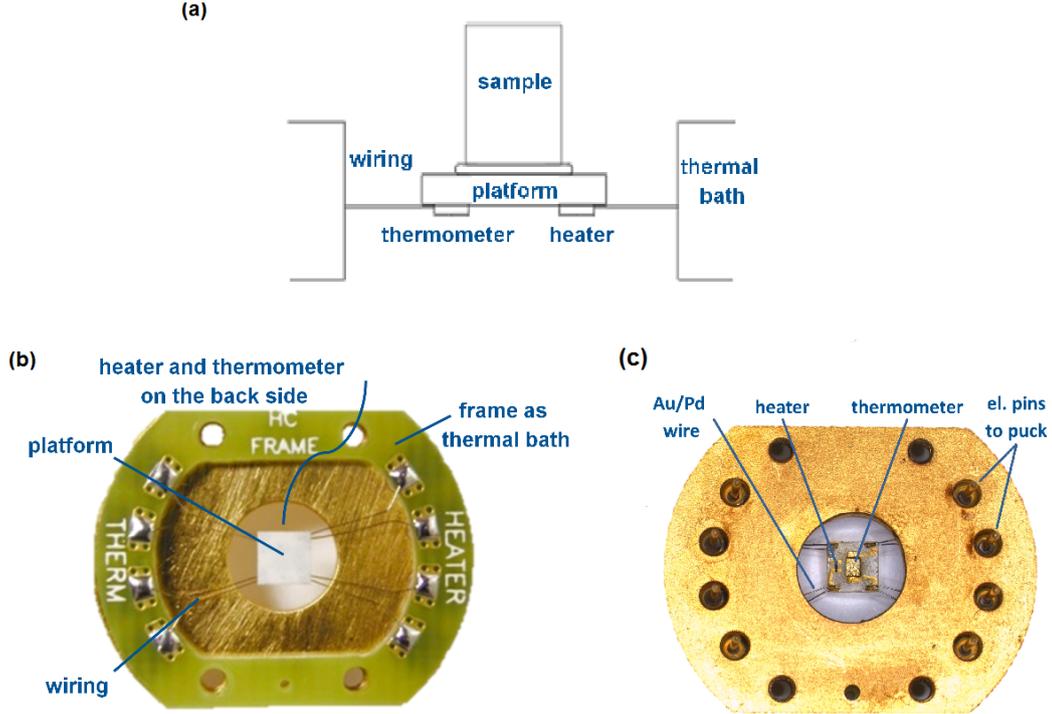
Figure 2.1: Schematic of PPMS Heat Capacity Option (a) and the associated frame attachable to the Heat Capacity puck from the top (b) and the bottom side (c). [44]

2.1.1 Relaxation technique

The heat flow diagram for a standard calorimeter is depicted in Figure 2.2 (a). A sample of unknown heat capacity C is attached to a sample platform with adhesive for thermal contact. The platform thermometer and heater are attached to the bottom of the platform.

Combined addenda heat capacity of the platform, thermometer, heater and adhesive, amounts to C_a. Heat is added with power $P(t)$ for a fixed time at the sample platform with a changing temperature T_p, after which a relaxation time τ_1 to the thermal bath at stable T_b occurs. Temperature response is recorded during the heating and the cooling process.

The relaxation time depends on the total heat capacity $C_{tot} = C + C_a$, and thermal conductance K_1 between the platform and the thermal bath. Thermal conductance of the adhesive K_2 should provide a fast response τ_2 ($\tau_2 \ll \tau_1$) in the sample temperature T.

Heat-balance condition for the system is described by the following equations, the first describing the platform (T_P) and the second the sample (T) [45]

$$P = C_a \frac{dT_p}{dt} + K_2(T_p - T) + K_1(T_p - T_b) \tag{2.1}$$

$$0 = C \frac{dT}{dt} + K_2(T - T_p) \tag{2.2}$$
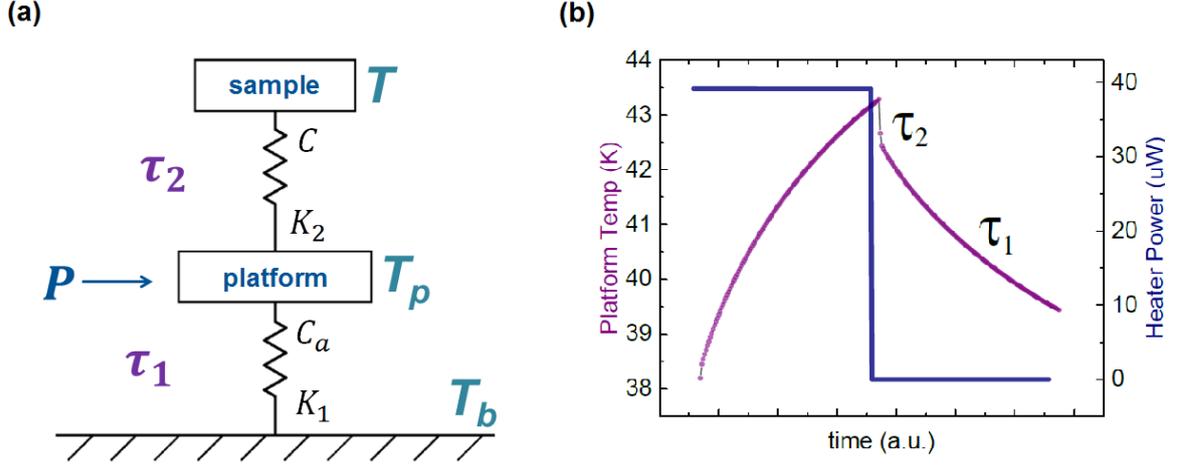
Figure 2.2: Typical caloric experiment showing its main properties and their relation to each other. A controlled amount of heat P is applied at the platform (T_P) and relaxed to the sample (T) and the thermal bath (T_b) with time constants τ_1 and τ_2, to the thermal bath and the sample, respectively (a). Two-tau temperature dependence of the platform temperature T_P, the blue line indicating the heater power P. A drop of $1K$ in temperature is visible during the τ_2 period (b).

Assuming an ideal (instant) thermal contact K_2 between the sample T and the platform T_p, the heat-balance equation simplifies to

$$P = (C_a + C)\frac{\mathrm{d}T_p}{\mathrm{d}t} + K_1(T_p - T_b) \tag{2.3}$$

When the heat flowing to the platform is discontinued, the sample platform temperature T_p follows the simple expression

$$T_p(t) = T_b + \Delta T \exp\left(-t/\tau\right) \tag{2.4}$$

with a time constant $\tau = (C + C_a)/K_1$. Disregarding the time dependence of C, C_a and K_1 for a small ΔT ($\Delta T \ll T$), Eq. (2.4) determines C from a measured τ. If the thermal contact of the adhesive K_2 is not sufficient to secure $K_2 \gg K_1$, the thermal decay involves the sum of two exponentials such as in Figure 2.2 (b).

$$T_p(t) = T + A \exp\left(-t/\tau_1\right) + B \exp\left(-t/\tau_2\right) \tag{2.5}$$

Addenda heat capacity is measured without a sample attached to the platform and K_1 is determined from measuring ΔT. Data analysis automatically subtracts the addenda heat capacity C_a from the calibration and fits the model, yielding a value of heat capacity C.

2.1.2 Measurement methods

It is common to distinguish the small heat pulse- from the quasi-adiabatic large pulse method. The pulse size is the percentage of the current sample temperature.

Small pulse method

The small pulse technique employs a heat pulse resulting in ΔT of about $(0.1 - 2)\%$ of the current sample temperature. Many small pulses are applied at different temperatures which can be time-consuming if τ_1 is overly large. This approach [46] neglects variations of the sample specific heat C over the temperature range of a single pulse. This is not necessarily true near a first-order phase transition. In addition, this approach neglects variations of thermal conductivity during a pulse [47].

Measured decay curves can be fitted with the Hwang-model [48] to obtain τ_1, τ_2, K_2 and C, for known values of C_a and K_1. The sample temperature T is logged as a function of time, and the whole response curve is used in the model. Therefore, for each pulse one obtains a single heat capacity value.

Large pulse method

In the large pulse technique, typical heat pulse increases the starting temperature by $(10-30)\%$. The heating and cooling curve are treated individually using the following equation [49]

$$C_{tot}\left(T\right) = \frac{-K_2(T - T_b) + P(T)}{\mathrm{d}T/\mathrm{d}t} \tag{2.6}$$

For fast scans, especially at higher temperatures, the heat capacity is derived using the dual-slope method [50]. Heating and cooling curves are combined by interpolation, assuming a symmetric pulse as follows

$$C_{tot} = \frac{P_h\left(T\right) - P_c\left(T\right)}{\left.\dfrac{\mathrm{d}T}{\mathrm{d}t}\right|_h + \left.\dfrac{\mathrm{d}T}{\mathrm{d}t}\right|_c} \tag{2.7}$$

where the indices h and c of the temperature response slope refer to the heating and the cooling curve, respectively. Therefore, for each point of the temperature response curve, one gets a heat capacity data point, resulting in higher data density. The results for neighbouring pulses are placed next to each other, forming a continuous curve in temperature. Using the dual-slope method, a larger peak is observed at the correct phase transition temperature of the heating curve with better statistics, almost equivalent to the cooling curve. The drawback of this method is a potential smaller second peak on the phase transition temperature of the cooling curve, owing to the aforementioned asymmetry. Nevertheless, this approach is preferred for data analysis.

Pulse asymmetry

Large overall heat capacity can lead to a non-symmetrical pulse, such as in Figure 2.3, due to the heat drag from the sample and the sample platform. Another source of such a discrepancy is the latent heat in the system.
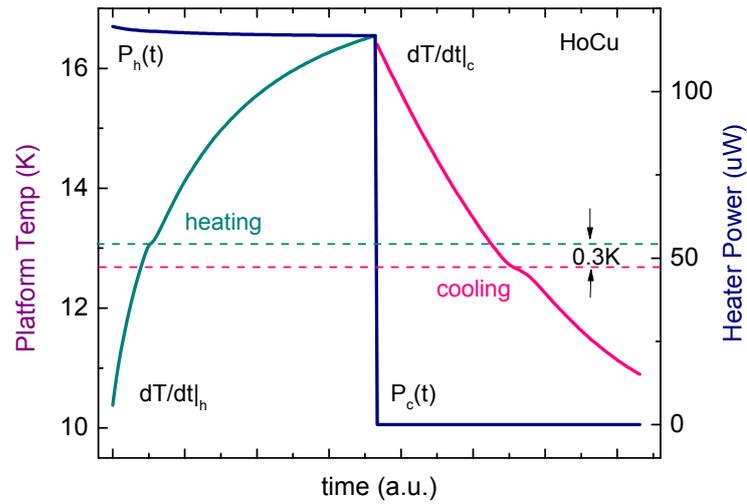
Figure 2.3: An asymmetrical heat pulse at the first order phase transition with the indicated heater power. Phase transition temperatures of the heating and the cooling curve disagree due to latent heat and the temperature drag from the platform.
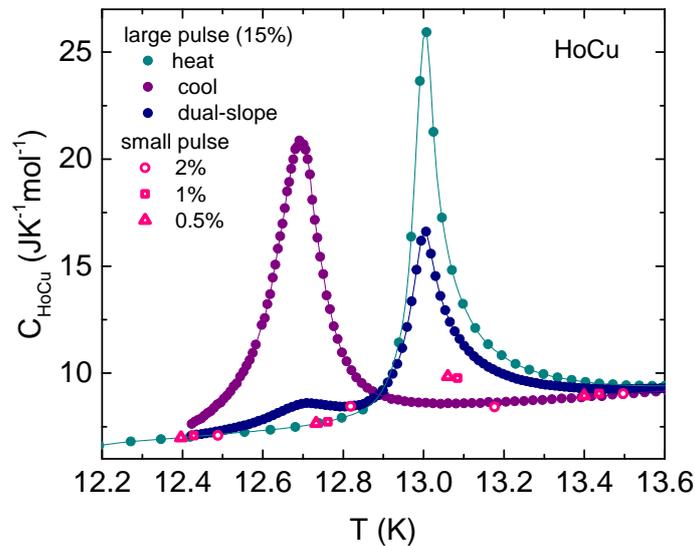
Figure 2.4: Pulse treatments with the small pulse and large pulse method in the vicinity of a phase transition. The heating, dual-slope and small pulse method agree on the peak position. The small pulse method is inapplicable for the RE-Cu measurements since the peaks are very narrow in temperature $(0.2\,\mathrm{K})$.

As a result, the heating and cooling curve disagree on the position and size of the phase transition, especially around first order phase transitions, involving the latent heat. The disagreement in the peak position is approximately $0.3\,\mathrm{K}$ at $13\,\mathrm{K}$ which corresponds to $\sim 2.5\%$, a temperature near a phase transition.

The heating process is faster than the cooling process, resulting in fewer data points, but its position agrees with the small pulse technique which is not susceptible to the temperature drag ambiguity, visible in Figure 2.4. Despite this, the small pulse method is impractical for the RE-Cu measurements since the pulses are as narrow as $0.2\,\mathrm{K}$, which would require many pulses and lead to extremely long measuring times.

2.1.3 Experimental error

Another important point to discuss is the uncertainty (experimental error) of every measured heat capacity data point. In general, the accuracy of the heat capacity measurement critically depends on [51]

- the accuracy of the energy, time and temperature measurements
- the internal relaxation time τ_2, meaning the uniform heat distribution to the sample, and the external relaxation time τ_1 between the platform and the surroundings

For a universal estimate of the heat capacity error, one can regard a semi-adiabatic heat pulse. It includes four distinct intervals:

The first, the fore-drift is the time when the heater is disabled, and the temperature floats due to heat exchange with the surrounding. In the heat pulse period, a $\Delta Q = Pt$ amount of energy is added to the platform. The temperature rises rapidly from turning on the heater to the end of the pulse. The third period is both the fast internal- and the slow external relaxation period. The final interval, the after-drift starts after the relaxation at t_1.

The biggest source of error comes from the temperature measurements. The thermometer calibration error is estimated at maximum 1% in the temperature range of interest from the comparison of the bath and platform temperature in thermal equilibrium. If we use the Eq. 1.12, the error of the measured heat capacity σ_C is given as follows

$$\sigma_C = \frac{1}{\Delta T}\left(\sigma_{\Delta Q} + C\sigma_{\Delta T}\right) \tag{2.8}$$

where $\sigma_{\Delta Q}$ and $\sigma_{\Delta T}$ are standard uncertainties in ΔT and ΔQ.

The average uncertainty in ΔQ of approximately 0.1% is achieved during the heat pulse for the used pulses in PMMS [44]. The significant part of the error is thus from the measured temperature uncertainty. It is assumed to be dominantly the difference of the sample temperature between the heat pulse period and the relaxation period for the same platform temperature.

There are two equivalent means to determining the experimental error supposing it occurs from the thermal drag of the sample to the platform temperature. Firstly, as one can see in the Figure 2.3, there is a τ_2 effect resulting in a temperature drop of $1\,\mathrm{K}$ at a temperature of $40\,\mathrm{K}$. This corresponds to a temperature uncertainty of $0.3\,\mathrm{K}$ at $13\,\mathrm{K}$ if we linearly extrapolate the value.

Secondly, taking a look at the asymmetrical pulse in Figure 2.4, there is a $0.3\,\mathrm{K}$ temperature difference between the phase transition as determined from the heating and the cooling curve. These values are similar since they both represent the same effect. Taking them in the Eq. 2.8, one comes to uncertainty in specific heat amounting to $\sigma_C/C \sim 2.5\%$ at $13\,\mathrm{K}$, a temperature near a phase transition.

2.2 Physical Property Measurement System (PPMS)

The PPMS can perform various experiments with precise thermal- and field control such as magnetometry, electrical transport, thermal transport or adapting the basic platform for unique configurations [44].

2.2.1 Cryostat and sample environment

The basic setup consists of a dewar with a superconducting magnet and a pump for evacuating the sample chamber. The available sample environment includes magnetic fields up to ± 14 T and a $(1.8 - 400)$ K temperature range.

The chamber incorporates a platform with 12 pins, and each experimental option uses its particular removable insert, or sample "puck", to be plugged in as required. A schematic of the sample environment is given in Figure 2.5 [52].
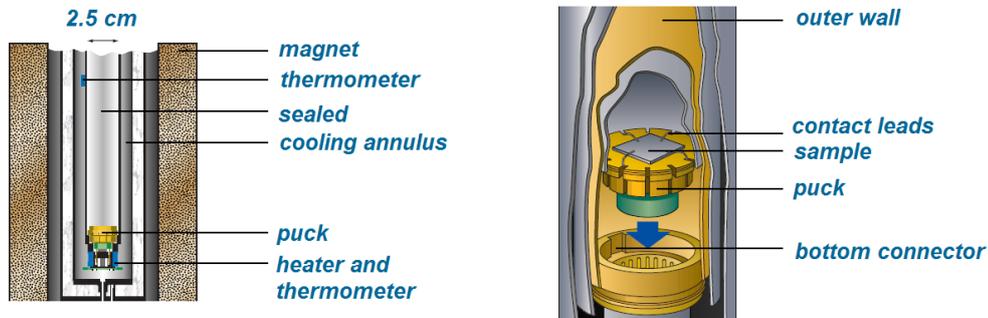
Figure 2.5: Sample environment in the PPMS cryostat (left) with a close-up on the sample insert (right). [52]

The Model 6000 PPMS Controller provides direct communication with the application electronics. PPMS MultiVu software is used for executing measurements and collecting data. With it, one can control the system parameters (temperature, field) manually or create measurement sequences to automatise its operation. Customising data acquisition with other programs such as Python is possible.

2.2.2 Heat Capacity Option

The Standard setup for the PPMS Heat Capacity Option consists of a puck and a sample frame. The frame has a sapphire or Al_2O_3 platform of 3×3 mm^2, suspended on eight $75 \, \mu$m Au-Pd wires such as in Figure 2.6 (a). They provide electrical contact, mechanical support and thermal path K_1 for the sample platform, the relation presented in Figure 2.6 (b).

A Ruthenium Oxide heater and a Cernox thermometer are attached on the back side, and the contacts are made of sputtered gold and wire bonded. The addenda

heat capacity is negligible in comparison to the sample heat capacity for the used RE-Cu samples.
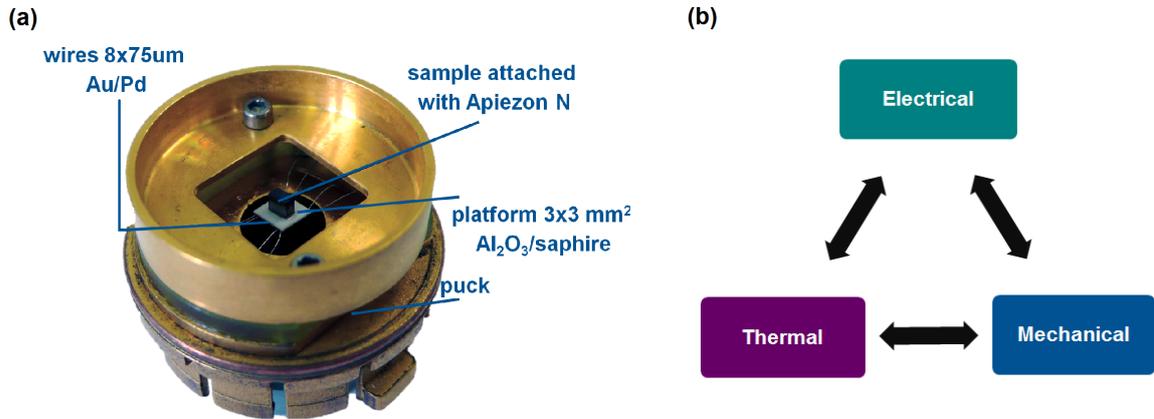
Figure 2.6: Standard Heat Capacity Option in the PPMS (a). Electrical, mechanical and thermal contact are all connected in the Standard setup (b).

The sample is mounted using a thin layer of Apiezon N grease $(1\,\mathrm{mg})$, which serves as the thermal contact to the platform K_2. Since the sample is only weakly fixed, it will easily turn towards a more favourable orientation in high magnetic field measurements along the hard axis.

The thermal connection to the thermal bath is dominated by the conductance of the wiring $K_1 \sim 18\,\mu\mathrm{W/K}$ (at $15\,\mathrm{K}$) since the sample space can be evacuated to high vacuum. This gives a reproducible heat link with the corresponding time constant sufficient to allow both sample platform and sample to achieve thermal equilibrium in the range of seconds. The PPMS calibration consists of measuring the setup heat capacity to subtract the addenda contribution C_a from the total heat capacity and determining the thermal conductance $\kappa = K_1$. It was performed in zero-field, $1\,\mathrm{T}$, $4\,\mathrm{T}$, $6\,\mathrm{T}$, $9\,\mathrm{T}$ and $14\,\mathrm{T}$ to account for the thermometer changes in magnetic field.

The temperature is logged as a function of time, each pulse consisting of 256 data points. An analysis of the PPMS performance and limitations was carried out by Lashley et al. [53]. An examination of the pulse size is given in the Figure 2.7 for the HoCu compound.

Post-processing

The post-processing procedure in MultiVu consists of applying a moving average (MA) for smoothing the data and excluding (EX) the initial part of the pulse. The MA can be in the range of $(1 - 10)\%$ which is by agreement increased until the nearby higher temperature points form a continuous, non-oscillating curve in a single pulse at phase transitions. It reduces the scattering of data points and causes a smearing of sharp anomalies.

The EX procedure of the pulses eliminates the influence of the thermal drag from the sample required to achieve thermal equilibrium and the effect of switching the

heater on and off. To account for these effects, it is possible to exclude the initial part of the pulse. This exclusion sometimes reaches 25%, thus, a considerable overlap (50%) in temperature is required for neighbouring pulses.

Further on, different post-processings disagree on the size of the peak at a phase transition, both in height and width, as well as the surface it encompasses. Treating all the data as described gives us an opportunity to examine the heat capacities and the derived values, keeping in mind it is primarily a qualitative analysis.
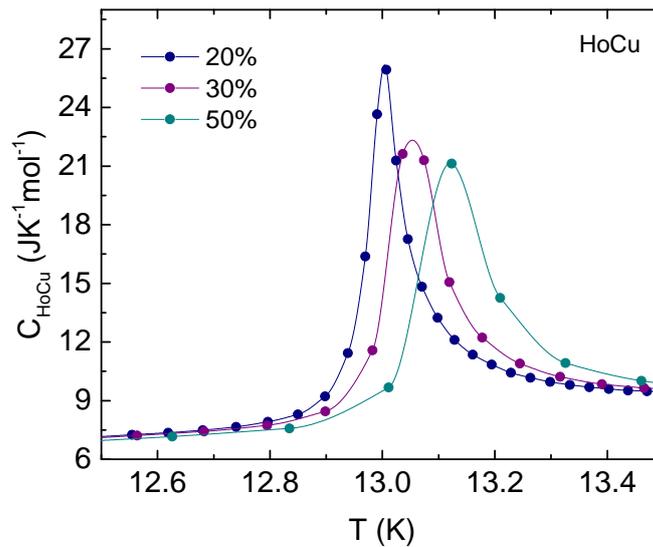
Figure 2.7: Pulse size varying from $(20 - 50)\%$ for the HoCu compound at a first order phase transition, showing the reduction of point density for larger pulses treated with a moving average of 10% and an initial pulse exclusion of 1%.

Larger pulses cover the temperature range with shorter measurement time, however, may give erroneous data when multiple phase transitions are encountered during a single pulse. Since the number of data points is fixed for any pulse size and duration, a larger pulse results in a lower density of points. The maximal pulse size is restricted by the requirement that the heating curve consists of enough data points for measurements to be regarded as relevant. On the other hand, the pulse size should not be smaller than the size of the phase transition itself and smaller pulses require more points, i.e. longer measurement times.

For the studied RE-Cu materials, the transitions are in the temperature range $(7 - 30)\,\mathrm{K}$ and some are as narrow as $0.2\,\mathrm{K}$, setting the appropriate pulse size to $(10 - 20)\%$.

Experimental error of the PPMS Heat Capacity Option

There are several means to determine the experimental error of a calorimeter. One way to estimate the error of the addenda and the total heat capacity is to compare them with known values measured at a different, more reliable setup. The second idea is to refer to an average deviation from a smoothed curve as an average accuracy. This gives a reasonable estimate of the repeatability, not the accuracy of a calorimeter. A third possibility is to express it as a standard deviation in the fit of a certain model.

The accuracy of the PPMS specific heat data is specified within the $\pm 5\%$ by Quantum Design, while the scattering of neighbouring data points is to be less than 1% [44]. These were presumably estimated using the first two stated methods, namely a comparison with a known specific heat value and the deviation from the smoothened curve. In the small pulse method, using the Hwang model, the experimental error is obtained from the fit and amounts to $(0.3 - 3)\%$ depending on the proximity of the phase transition for HoCu measurements. Lashley et al. [53] compared the specific heat values of the Standard PPMS setup operating in the large pulse method with a semi-adiabatic calorimeter at Lawrence Berkeley National Laboratory for gold samples. Estimates of this error for the temperatures in the range of $(4 - 30)\,\mathrm{K}$ are $(0.5 - 1)\%$. However, at a phase transition of a superconductor $\mathrm{Mg}_{11}\mathrm{B}_2$ the observed differences amounted up to 15%.

2.3 Development of magnetic hard axes heat pulse calorimeter

The studied systems are anisotropic and display a change of the magnetic easy axis with changes of temperature and field. Problems were encountered due to rotation of the sample with magnetisation $\vec{M}$ in magnetic field $\vec{B}$ (Fig. 2.8). When measuring along the hard magnetisation axis in high fields, a magnetic torque $\vec{\tau} = \vec{M} \times \vec{B}$ tilts the present-day platform or detaches the sample. In order to remedy this flaw in the Standard heat capacity setup, a modification of the sample stage was undergone.
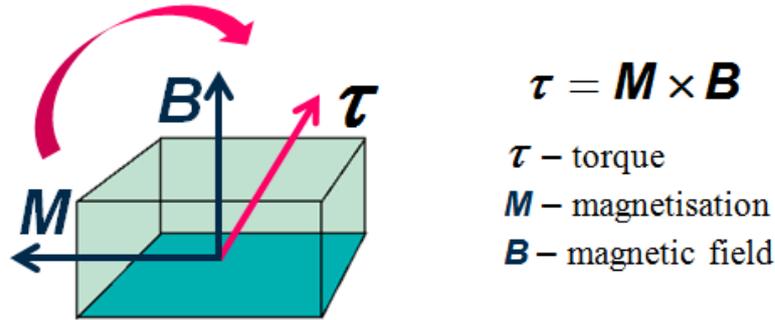
Figure 2.8: The magnetic torque when measuring along the hard magnetisation axes.

The specific heat and magnetocaloric measurements of complex magnetic systems under high magnetic fields impose considerable and often competing requirements on the experimental setup. When adding parts to the original setup, it is necessary to calculate their effect on the time constants and to adjust their material, size and shape so that the relation between them remains similar. One wants to minimise the relative contribution of the addenda to the total signal but have a good mechanical stability to overcome the forces resulting from the sample with a large magnetic moment. On the contrary, a large sample with a large total magnetic moment requires longer relaxation times.

I introduced two new designs, the Al- and the Kevlar setup, calculated the relevant parameters (C_a, K_1, τ_1) and experimentally established an appropriate measuring routine for the available samples. The geometric parameters of the new setups are given in subsections 2.3.2 and 2.3.3., while the properties relevant for thermodynamic measurements are presented in section 2.4.

2.3.1 Al setup

An upgrade of the Standard setup was first performed using the Standard puck and frame for measuring the heat capacity. The new design, shown in Figure 2.9 (a), consists of a mechanically stable aluminium plate ($0.5\,$mm) instead of the sample platform, which primarily determines the addenda heat capacity, and fibreglass spacers, which define the thermal conductance.

Figure 2.9: Heat capacity puck with a mounted Al setup (a). The electrical contact is separated while the mechanical and the thermal contact are coupled through the fibreglass spacers (b).

Aluminium was selected among the non-magnetic machinable materials because of its low density. It consequently gives an overall smaller heat capacity than the heat capacity of other materials with similar specific heat. Since it is a good thermal and electrical conductor, it needs to be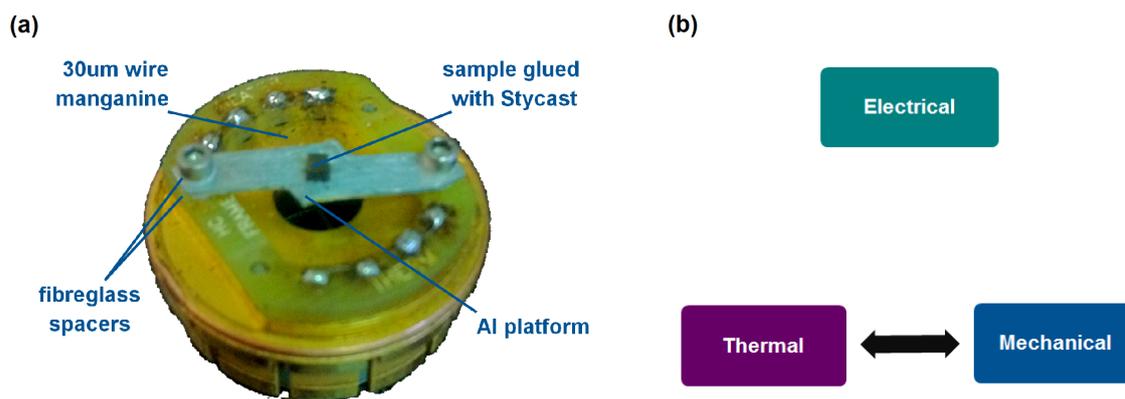 separated from the bath to permit gradual relaxation. Fibreglass spacers were chosen for this purpose, because of their low heat capacity and thermal conductance. Precise defining and tuning of the thermal link is achieved by the geometry of the spacers, the area of contact with the heat sink and their thickness ($0.5\,\mathrm{mm}$).

A Ruthenium Oxide RX-102A, $1\,\mathrm{k\Omega}$ chip is used as a heater and a Cernox temperature sensor CX-1010 is used as a thermometer, both purchased from Lake Shore. It is possible to calibrate this thermometer down to temperatures of $100\,\mathrm{mK}$. Small bare chips were added manually, fixed with GE varnish and contacted with four $0.7\,\mathrm{cm}$ long $30\,\mu\mathrm{m}$ manganine wires using a two component silver epoxy (EPO-TEK, H20S). Manganine has significantly lower thermal conductance than the conventional Au-Pd wiring. It is thus assumed that the thermal contact is given solely through the fibreglass spacers. Thereby, the electrical contact is decoupled from the mechanical and the thermal contact; the resulting relation is given in Figure 2.9 (b).

Though the mechanical stability is given solely by the Al platform, the thermal path is through both the Al plate and the fibreglass spacers. There is always a temperature gradient along the platform since one of its sides is permanently attached to the thermal bath at the spacers.

The sample is attached by Stycast 2850 FT, a two component, thermally conductive epoxy. It gives a strong permanent connection of the sample to the sample platform. Its addenda contribution is comparable with the addenda of the Apiezon N grease in the conventional setup. It is possible to remove and reuse the sample after diluting and softening Stycast with acetone.

2.3.2 Kevlar setup

The second design aims to reduce the effects of torques massively, while separating the electrical, mechanical and thermal contact entirely, alongside with providing a better defined thermal link. It is inspired by the setup in the doctoral thesis of A. Rost [54]. The particular implementation is shown in Fig. 2.10.
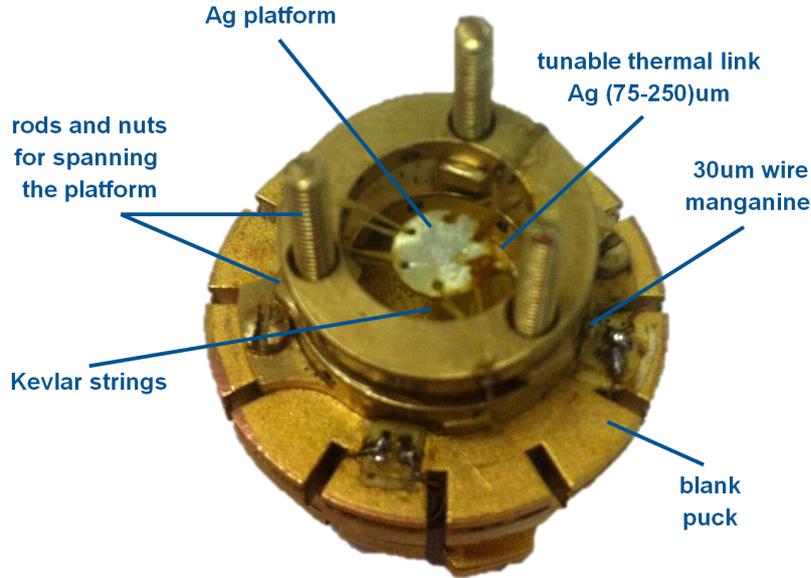
Figure 2.10: Blank puck with a mounted Kevlar setup.

Unlike in the Standard- and the Al setup, the starting base for the construction of the Kevlar setup was a blank Quantum Design puck, instead of the heat capacity puck. The sample platform is a silver plate, 0.5 mm thick with a diameter of 5 mm. Silver was chosen, for its good thermal conductivity and since it is suitable for mK measurements.

On the top side of the platform, the sample can be glued with Stycast 2850 FT, while the heater and the thermometer are installed on the bottom side using GE varnish. The heater is a standard SMD 1 kΩ resistor, and the thermometer is the same Cernox CX-1010 chip used in the Al setup. The SMD resistor is smaller in size compared to the RX-102A resulting in a smaller addenda contribution, but the difference is neglected in the following analysis. The electrical contacts are made with four 2 cm long 30μ m manganine wires.

The mechanical support between the sample platform and the thermal bath has to have an extremely low thermal conductivity to achieve a high tunability of the thermal link. The chosen design, therefore, uses Kevlar strings, made of ~40 extremely strong filaments of $12\,\mu$m in diameter (Goodfellow, Kevlar @29-167). They are threaded through holes in the platform and the accompanied structure.

This structure is more easily understood in the SolidWorks sketch in Figure 2.11 (a). It consists of two brass rings, a lower fixed ring screwed into the blank puck, and an upper moveable ring with which the mechanical rigidity is attained. The lower

ring has gaps for wiring and three vertical holes for rods onto which the upper ring is mounted. The distance between the two rings is adjusted using nuts on rods, which are used to find a stable horizontal position of the platform.

Thermal contact is achieved by a $(1-2)$ cm silver wire spanning from the platform to the lower ring. It is glued with GE varnish on both sides, and its diameter can be changed to adjust the relaxation times. In this study, two different links were tried out with diameters of $75\,\mu$m and $250\,\mu$m. The relation between the electrical, mechanical and thermal contact is depicted in Figure 2.11 (b).
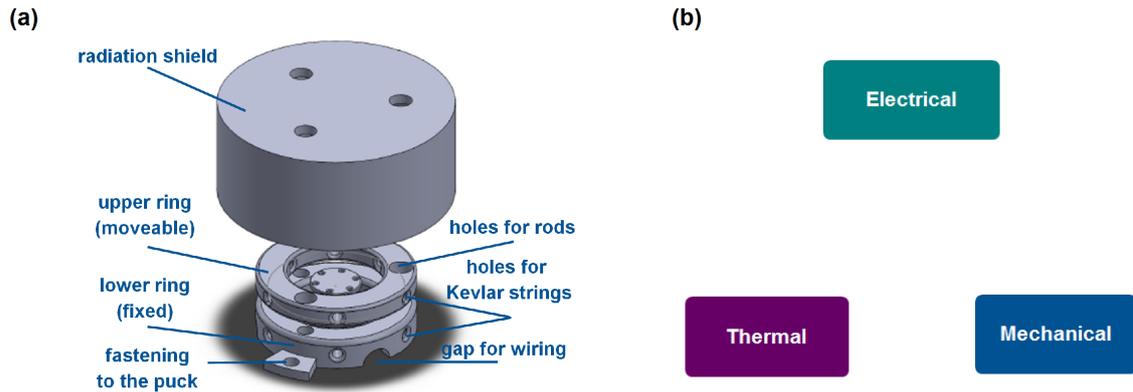
Figure 2.11: Drawing of the Kevlar setup components designed in SolidWorks (a). Electrical, mechanical and thermal contact are all decoupled (b).

Though the Kevlar strings can be tensioned at room temperature, they have a negative thermal coefficient of expansion, meaning that they extend at low temperatures. A check of the platform rigidity was conducted by cooling the sample to liquid nitrogen temperature (77 K) since most of the total thermal expansion takes place above this temperature. No change in platform stiffness was observed when it was immersed in liquid nitrogen and manually pushed.

The setup was built to fit into the existent ADR cryostat, but it has so far not been tested in these conditions.

2.4 Setups comparison

Thermal characteristics of the new setups were estimated on the basis of physical properties for used materials selected according to advice found in literature [55], [56]. These were calculated and adjusted to allow shortest measurement times still accessible by the PPMS.

The new setups were verified by comparing results on RE-CU as well as measuring the specific heat of MnSi, a thoroughly studied compound in the E51 group. Ultimately, the limits of the measurement technique are approached by studying the peculiar shape of single pulses, and the measurement uncertainty is estimated.

2.4.1 Thermal properties of calorimeters

The most important thermal property is the relaxation time constant. The simple expression giving the time constant τ follows

$$\tau = \frac{C}{K} \tag{2.9}$$

in which the numerator is the heat capacity and the denominator the thermal conductance. For the calibration, the upper term is the addenda heat capacity C_a, while during the measurements it is the total heat capacity C_{tot}, the sum of the addenda and the sample heat capacity.

In both cases, the τ needs to be measurable, in the PPMS ($> 0.1\,\text{s}$), yet a smaller time constant is preferred for faster measurements. To achieve good resolution of sample heat capacity, the addenda heat capacity needs to be smaller than the sample heat capacity.

The temperature range of interest is below the ordering temperature of RE-Cu compounds, $(2-30)\,\text{K}$. The calculations for Tau constants were carried out at $2\,\text{K}$, $5\,\text{K}$, $10\,\text{K}$, $20\,\text{K}$, $50\,\text{K}$, $100\,\text{K}$ and $300\,\text{K}$ using the tabulated value of specific heat and thermal conductance for the used materials [56]. Typical samples are cubes or cuboids of $(1-2)\,\text{mm}$, having a heat capacity of $(2-10)\,\text{mJK}^{-1}$ at $15\,\text{K}$.

The results are presented both in text and in tabular form for $15\,\text{K}$, a mid-range temperature of interest, for which the values were linearly interpolated. The tables clarify the calculation procedure and the ratio between the segments of the setup. The graphic form of the results covers a wider temperature range to follow the relation of various properties in different setups.

Addenda heat capacity

In the standard setup, the specific heat of sapphire is low, $0.5\,\text{mJg}^{-1}\text{K}^{-1}$, leading to a contribution of the order of nJK^{-1}. The addenda heat capacity is given by the heater and thermometer, measured in the calibration to be $50\,\mu\text{JK}$. An additional addenda contribution is coming from Apiezon N grease used for thermally connecting sample.

It has a specific heat of $0.05\,\mu\mathrm{Jg^{-1}K^{-1}}$ which for a mass of approximately $1\,\mathrm{mg}$ gives a contribution of $0.05\,\mathrm{nJK^{-1}}$.

at 15 K	heater and thermometer	mechanical stability	addenda
Standard		*sapphire* $0.5\,\mathrm{mJg^{-1}K^{-1}}$ platform $\sim\mathrm{nJK^{-1}}$	$\sim 50\,\mu\mathrm{JK^{-1}}$
Al	$\sim 50\,\mu\mathrm{JK^{-1}}$ (calibration)	*Al* $5\,\mathrm{mJg^{-1}K^{-1}}$ plate $\sim 0.5\,\mathrm{mJK^{-1}}$ *fibreglass* $30\,\mathrm{mJg^{-1}K^{-1}}$ spacers $\sim 0.4\,\mathrm{mJK^{-1}}$	$\sim 0.9\,\mathrm{mJK^{-1}}$
Kevlar		*Ag* $6\,\mathrm{mJg^{-1}K^{-1}}$ platform $0.6\,\mathrm{mJK^{-1}}$	$\sim 0.6\,\mathrm{mJK^{-1}}$

Table 2.1: Addenda heat capacity analysis at $15\,\mathrm{K}$ for the three setups. Data are taken from [56].

In the new setups, the main addenda contributions come from the new platforms. Aluminium has a specific heat of $5\,\mathrm{mJg^{-1}K^{-1}}$, giving an addenda heat capacity of the plate $0.5\,\mathrm{mJK^{-1}}$. Fibreglass specific heat amounts to $30\,\mathrm{mJg^{-1}K^{-1}}$, resulting in the spacers heat capacity of $0.2\,\mathrm{mJK^{-1}}$. The total addenda heat capacity for the Al setup is calculated to be $0.7\,\mathrm{mJK^{-1}}$ at $15\,\mathrm{K}$. Silver has a specific heat of $6\,\mathrm{mJg^{-1}K^{-1}}$, leading to a heat capacity addenda of the platform $0.8\,\mathrm{mJK^{-1}}$.
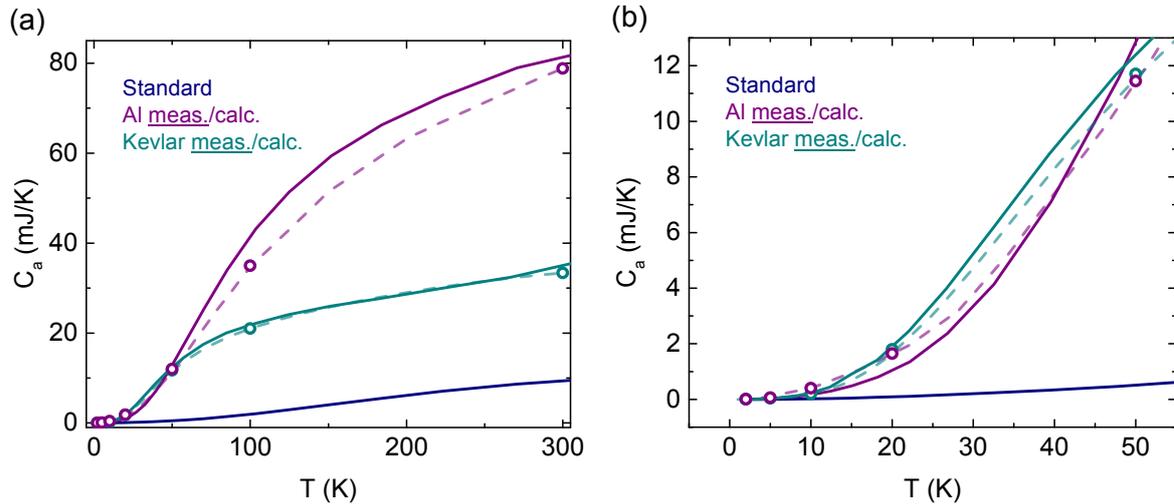
Figure 2.12: Addenda heat capacity of the three setups $(2-300)\,\mathrm{K}$ (a) and in the temperature range of interest $(2-50)\,\mathrm{K}$ (b). The dashed line represents the interpolation of the calculated estimate of the addenda heat capacity at seven stated temperatures shown as open circles.

A secondary contribution in the new setups is the addenda from the heater and the thermometer, being similar to the value in the Standard setup. The third part of

the addenda is given by roughly $1 \, \text{mg}$ of Stycast for fixating the sample. All amorphous materials, such as Apiezon N and Stycast, have the same order of magnitude and similar temperature dependence of specific heat [54]. These contributions are in both cases much lower than the addenda heat capacity from the structures giving mechanical stability.

Finally, in all three cases, there is the contribution of the wiring, neglected in the heat capacity assessment due to their small mass.

Results for the measured (full line) and the estimated (open circles and dashed line interpolation) addenda heat capacity for the three setups are given in Figure 2.12. The left figure represents the entire temperature range while the right one focuses on the temperature range of interest, where the new setups are viable. The calculated values are in good agreement with the measured values with a discrepancy in the Al setup.

Since the fibreglass spacers contribute both to mechanical stability and serve as a thermal link, they are always in contact with the thermal bath, meaning that they are not entirely and uniformly heated during a pulse. Thermal gradient in the fibreglass spacers renders the calculated addenda heat capacity values larger than the real measured addenda heat capacity. At higher temperatures, the calculated value underestimates the real measured heat capacity which might be due to the very strong coupling from the heater to the thermal bath. In this way, a pulse could raise the temperature of the puck as well, making it a part of the addenda.

Figure 2.13: Addenda heat capacity in comparison with the ErCu sample heat capacity, showing the applicability of the new setups.

At higher temperatures, the calculated value underestimates the real measured heat capacity which might be due to the very strong coupling from the heater to the thermal bath. In this way, a pulse could raise the temperature of the puck as well, making it a part of the addenda.
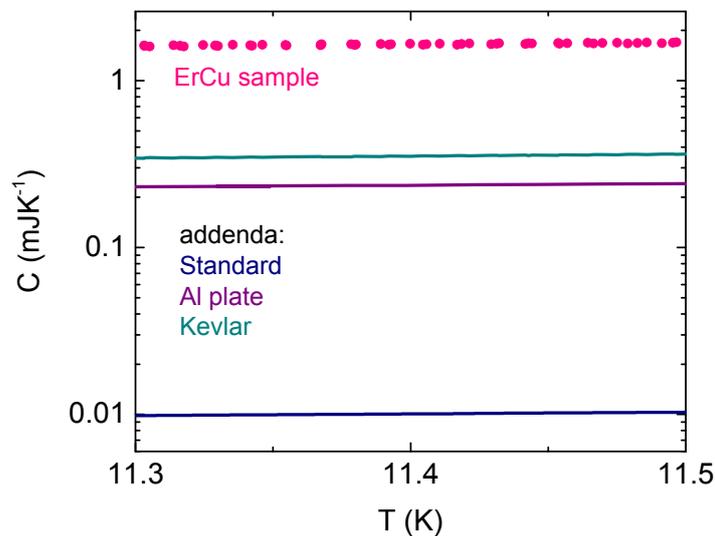
38

The new setups have significantly greater heat capacities than the Standard setup. Nevertheless, in Figure 2.13, one can see that the heat capacity of the sample (ErCu, OFZ-104-3-4-1) is substantially larger than the addenda heat capacity.

Thermal conductance K_1

The large addenda heat capacity needs to be followed by a proportionally larger thermal link to keep the τ constants reasonable ($< 1000\,\mathrm{s}$) range and reachable for the system ($> 0.1\,\mathrm{s}$). The second vital property of the setup is hence the thermal conductance between the sample and the thermal bath.

In the standard setup, this is given solely by the eight $75\,\mu\mathrm{m}$ Au-Pd wires. The thermal conductance of the wiring is read from the calibration files to be $18\,\mu\mathrm{WK}^{-1}$ at $15\,\mathrm{K}$.

In the Al setup, the aluminium has a large thermal conductivity $15\,\mathrm{Wm}^{-1}\mathrm{K}^{-1}$) and is assumed to thermalise instantaneously in comparison with the fibreglass spacers which have a thermal conductivity of $0.14\,\mathrm{Wm}^{-1}\mathrm{K}^{-1}$ at $15\,\mathrm{K}$. The thermal conductance is given by

$$K = k\frac{A}{l} \tag{2.10}$$

where A is the surface and l the length of the thermal link. The spacers are $0.5\,\mathrm{mm}$ thick, have an outer diameter of $2\,\mathrm{mm}$ and an inner diameter of $1\,\mathrm{mm}$, giving a thermal conductance of $0.2\,\mathrm{mWK}^{-1}$ at $15\,\mathrm{K}$. The measured thermal conductance is $0.33\,\mathrm{mWK}^{-1}$, which is in good agreement with the prediction.

The thermal link in the Kevlar setup is given by a silver wire, approximately $(1-2)\,\mathrm{cm}$ long and can be tuned by changing its diameter. The two different links used in this study had a diameter of $75\,\mu\mathrm{m}$ and $250\,\mu\mathrm{m}$. Silver thermal conductivity is similar to the Al thermal conductivity but strongly depends on its purity. The results from the calibration give a value of $0.02\,\mathrm{mWK}^{-1}$ for the $75\,\mu\mathrm{m}$ and $0.08\,\mathrm{mWK}^{-1}$ for the $250\,\mu\mathrm{m}$ wire. Though the diameter ratio predicts a 11 fold increase in thermal conductance for a thicker wire, just a 4 times larger value was observed. This can partly be explained by different length and shaping of the wire. The thicker wire is more difficult to shape and is, for this reason, longer.

The thermal conductance in the Kevlar setup is assumed to rise exclusively from the silver wire according to the following discussion. The 12 Kevlar strings each consist of 40 filaments of $12\,\mu\mathrm{m}$ diameter and $4\,\mathrm{mm}$ length. The thermal conductivity of Kevlar is extremely low $4\,\mathrm{mWm}^{-1}\mathrm{K}^{-1}$ (at $4\,\mathrm{K}$) with weak temperature dependence, giving a thermal conductance of $0.2\,\mathrm{nWK}^{-1}$. The mechanical support does not contribute to the thermal conductance of the Kevlar setup. The four $30\,\mu\mathrm{m}$ manganine wires in new setups have a thermal conductivity of $95T^{1.19}\,\mathrm{mWm}^{-1}\mathrm{K}^{-1}$ [54] which with $(0.7-2)\,\mathrm{cm}$ length, result in a small thermal conductance of $(12-34)\,\mathrm{nWK}^{-1}$.
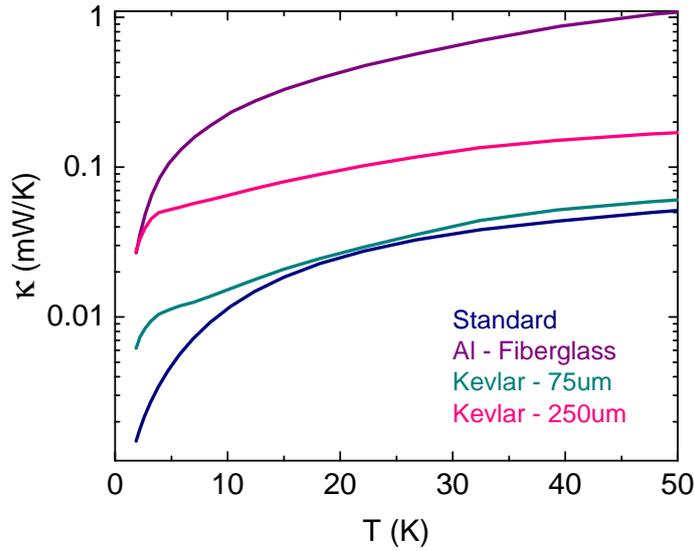
Figure 2.14: Thermal conductance of different setups in logarithmic scale. The Kevlar setup thermal conductance is tuned by changing the wire diameter.

at 15 K	thermal conductance	
Standard	$0.018\,\mathrm{mWK}^{-1}$ (*Au-Pd* from calibration)	
Al	*manganine* $95T^{1.19}\,\mathrm{mWm}^{-1}\mathrm{K}^{-1}$ $12\,\mathrm{nWK}^{-1}$	*fibreglass* $0.14\,\mathrm{Wm}^{-1}\mathrm{K}^{1}$ $0.33\,\mathrm{mWK}^{-1}$
Ag	$34\,\mathrm{nWK}^{-1}$	*Ag* $75\,\mu\mathrm{m}$ - $0.02\,\mathrm{mWK}^{-1}$ *Ag* $250\,\mu\mathrm{m}$ - $0.08\,\mathrm{mWK}^{-1}$ (calibration)

Table 2.2: Thermal conductance analysis at $15\,\mathrm{K}$ for the three setups. Data are taken from [56] and [57].

Thermal conductances are tabulated for $15\,\mathrm{K}$ in Table 2.2 and the measured values from the calibration are depicted in Figure 2.14. Al setup has the largest thermal conductance while the thermal link of the Standard- and the Kevlar setup with a weaker thermal link are the smallest and alike.

Tau constants for addenda calibration and sample measurements

Finally, taking a closer look at the τ constants of different setups in Figure 2.15 for the calibration (left) and the sample measurements (right) reveals that the Standard and Al setup agree on the time constants for the calibration while the Kevlar setup has a notably longer time constant disregarding the thermal link size. Table 2.3 gives an overview of the addenda heat capacity, the thermal conductance and the resulting tau constants for the calibration and for a $5\,\mathrm{mJK}^{-1}$ sample.

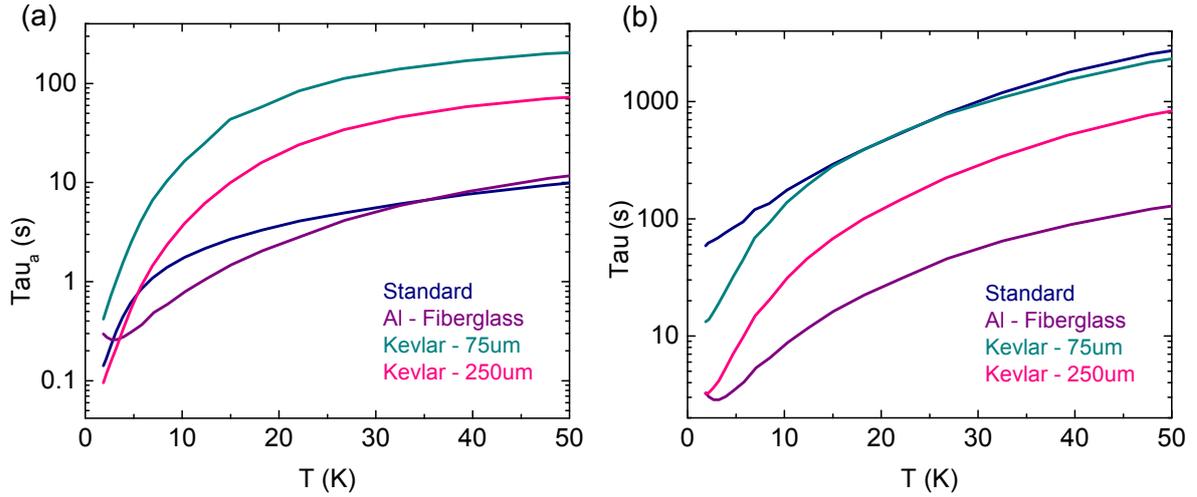Figure 2.15: Relaxation constant to the thermal bath during calibration of the addenda (a) and for average sample (b), shown in logarithmic scale. Shorter time constants produce faster results.

at $15\,\mathrm{K}$	addenda C_a	th. cond. κ (mWK^{-1})	$\tau_a = C_a/\kappa$ (s)	$\tau = C_{tot}/\kappa$ (s)
Standard	$\sim 50\,\mu\mathrm{JK}^{-1}$	0.018	2.8	260
Al	$\sim 0.5\,\mathrm{mJK}^{-1}$	0.33	1.5	17
Ag	$\sim 0.8\,\mathrm{mJK}^{-1}$	$75\,\mu\mathrm{m}$ - 0.02	40	290
		$250\,\mu\mathrm{m}$ - 0.08	10	73

Table 2.3: Tau constants at $15\,\mathrm{K}$ in the three setups, for the calibration and an average sample of heat capacity $5\,\mathrm{mJK}^{-1}$.

For the more relevant, sample time constants, the longest time constant is the one of the Standard setup, the Kevlar setup with a weaker link being slightly below. The shortest time constant is achieved with the Al setup. The Kevlar setup with a stronger thermal link produces a mid-range relaxation constant among the four different arrangements.

2.4.2 Verification

Different setups were used to measure the heat capacity of ErCu for verifying the new setups. The results for $(5.3 - 5.5)\,\mathrm{K}$ and $(15.5 - 15.7)\,\mathrm{K}$ are shown in Figure 2.16.

The slopes of the three curves agree while the absolute value differs by less than 5%. The difference of 2% at $15\,\mathrm{K}$ is alike the experimental uncertainty error in section 2.1. The startling disparity in point density comes from different post-processing requirements for different setups.

The post-processing procedure consists of applying a moving average (MA) for smoothing the data and excluding (EX) the initial part of the pulse as described in subsection 2.2.2.
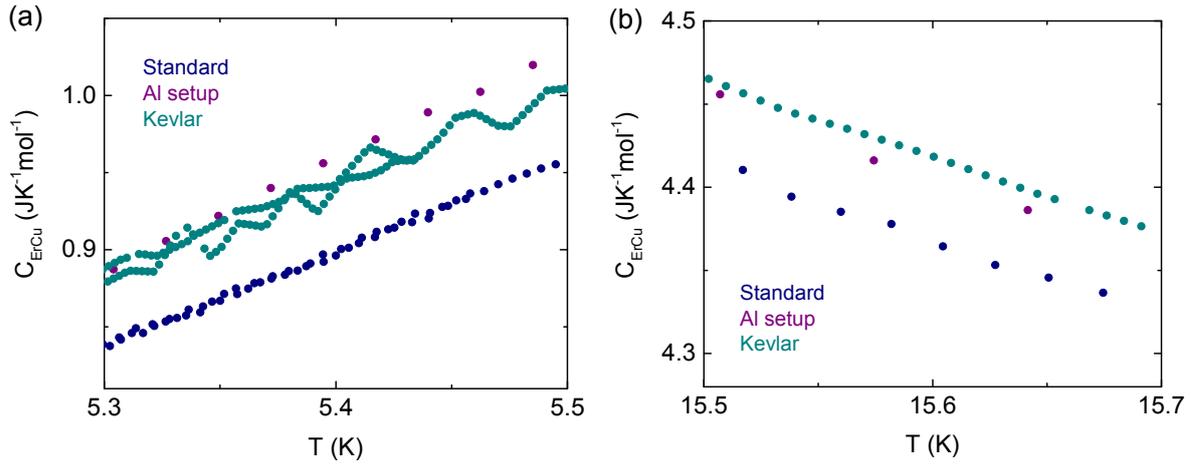
Figure 2.16: Specific heat of ErCu sample at $(5.3 - 5.5)\,$K (a) and at $(15.5 - 15.7)\,$K (b) as measured with the Standard-, Al- and Kevlar setup, using 20% pulses. Different post-processing applied according to the setup results in different density of data points. The heat pulse is defined by a percentage of the bath temperature which results in fewer points for the same temperature range at higher temperatures.

In the case of the Standard setup, a moving average of $(3 - 5)\%$ is regularly required, in the Al setup a MA of 10% is regularly required and in the Kevlar setup a 1% moving average suffices. This shows that the preferred setup for RE-Cu measurements is the Kevlar setup. It is often needed to apply large exclusions $(15 - 25)\%$ when the pulse size is large. This does not change the density of data points, but a significant (50%) overlap of neighbouring pulses is necessary.

Al setup was the first proposed design for improving the mechanical stability and the idea of tuning the thermal link independently, as in the Kevlar setup, came subsequently. For this reason, the first third of the overall results, namely the phase diagram of ErCu in $\langle 110 \rangle$ direction, were obtained using this setup, while the following measurements were done with the Kevlar setup.

2.4.3   Potential and limits

The estimated error when using the small pulse method comes from fitting the two-tau model while the software does not give an uncertainty of the measured heat capacity when using the post-processing procedure. The error can then be evaluated following the general discussion in section 2.1. According to the previous discussion, the error of the new setups is comparable to the error of the PPMS Standard setup when the resolution limit of the addenda contribution is respected, being 2.5% at $13\,$K, near a phase transition.

MnSi heat capacity measurement with the Kevlar setup

To test the potential of the new setups, measurements on MnSi were performed, a compound studied extensively in this group. Its magnetic phase diagram is presented in Figure 2.17 (a), showing a helical and a paramagnetic phase in zero-field and a phase pocket of the skyrmionic phase at intermediate fields, between the conical and the paramagnetic phase [58]. Previous measurements of specific heat of this compound were conducted by A. Bauer, during his doctoral studies [59] using the PPMS Standard setup. The results at $165\,\mathrm{mT}$ (Fig. 2.17 (b)) show two peaks at phase transitions. The peak at $28.5\,\mathrm{K}$ represents the transition from the conical to the A-phase, while the peak at $28.8\,\mathrm{K}$ is the transition from the A-phase into the paramagnetic state.
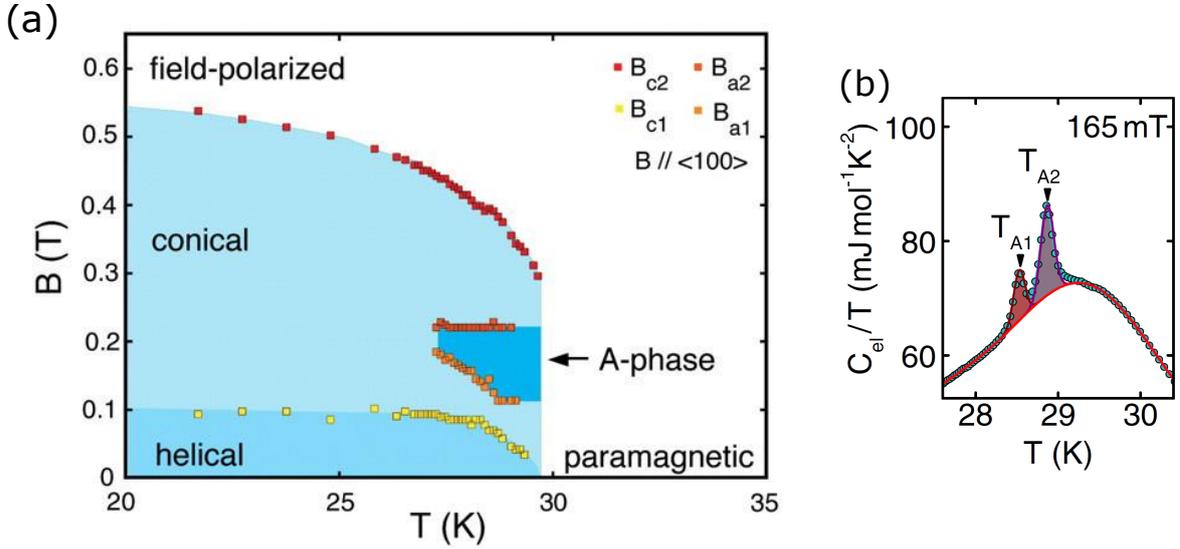
Figure 2.17: Magnetic phase diagram of MnSi for field along $\langle 100 \rangle$ (a). For intermediate field values, the conical phase develops in the A-phase as a small phase pocket. [1] Specific heat of MnSi divided by T at $165\,\mathrm{mT}$, showing the skyrmionic phase transitions, measured with the Standard Heat Capacity option. [59]

It was a challenge to measure this compound using the new setups. At $30\,\mathrm{K}$ the heat capacity of the new setups is similar to the heat capacity of the addenda $C_a \sim C_{RE-Cu} \approx 4\,\mathrm{mJK^{-1}}$. MnSi sample of comparable size ($8\,\mathrm{mm^3}$) has a three times smaller heat capacity of $2\,\mathrm{mJK^{-1}}$ at $30\,\mathrm{K}$. This is evident when considering the molar masses of the two compounds $M_{ErCu} = 230.81\,\mathrm{g/mol}$, $M_{MnSi} = 83.02\,\mathrm{g/mol}$, giving the aforementioned ratio $M_{ErCu}/M_{MnSi} \approx 3$.

The measuring procedure used in previous measurements was to apply a single pulse of $\sim 10\%$ over the temperature range where transitions occur. This was not possible with the new setups since more post-processing was required. Several small pulses of 2% were used instead and post-processed with a moving average of 10% and an initial exclusion of 10% (Figure 2.18). The specific heat values at phase transitions are in good agreement with the previous measurements, while the scattering can be

accounted for by the previously discussed experimental error. Peak positions differ $0.2\,$K, which corresponds to the thermometer calibration accuracy. The disagreement could be due to the change of the measuring procedure, a temperature gradient in the sample or a potentially not perfectly defined magnetic field.
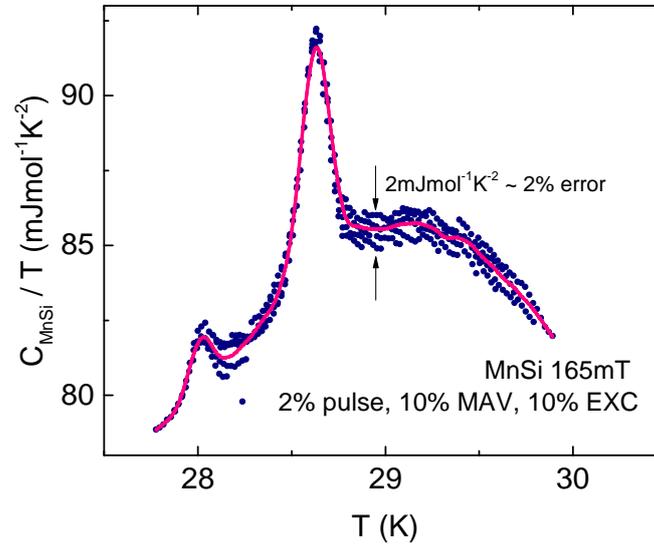
Figure 2.18: Specific heat of MnSi divided by T at $165\,$mT as measured using the Kevlar setup. The peak position and size difference to the previous measurements can be accounted for by the experimental error and the thermometer accuracy, the pink curve obtained by interpolation (100000 points) and smoothening (1000 points window).

Pulse shape as a result of relaxation times

One peculiar artefact of the measurement technique are the pulse shapes, often leading to a discontinuous transition between the neighbouring pulses. Since the relaxation times are rather long $(100\,\text{s})$, there might be some residual heat in the system when applying the next pulse. This results in an error in the initial part of the pulse which can be corrected by EX.

Usually, a $60\,$s waiting time was added between the pulses. To demonstrate the aforementioned effect, two neighbouring pulses were applied with no waiting time (Figure 2.19). Post-processing was used to distinguish the heating and the cooling curve from the dual-slope processing. The offset is largest for the heating curve due to temperature drag from the sample and the fastest temperature change, set by the heater, not the system. The cooling curve exhibits an equivalent issue at the end of the cooling curve.

Most reliable results are achieved with the dual-slope processing, but slightly curved shape without physical significance remains for each pulse.

Figure 2.19: Two neighbouring pulses applied with no waiting time processed to obtain ErCu heat capacity from the heating (a) and the cooling curve (b) in comparison with the dual-slope processing (c). One observes that the offset is largest for the heating curve due to temperature drag from the sample and the fastest temperature change. Most reliable results are achieved with the dual-slope processing, but slightly curved shape without physical significance remains for each pulse.
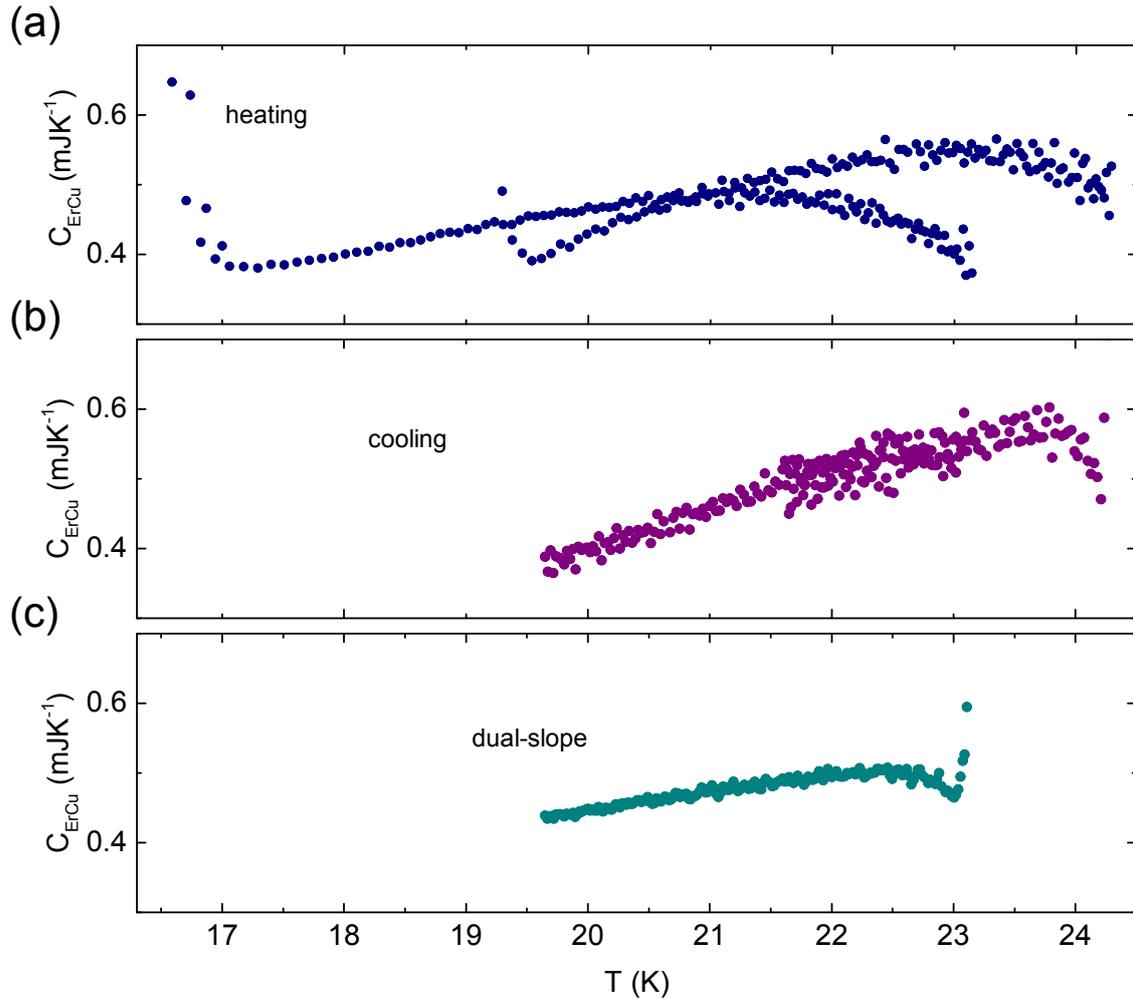
3 Results

New setups were characterised and applied for the determination of specific heat of ErCu in high magnetic fields for the three main crystallographic axes. An overview of the conducted heat capacity measurements is given in Table 3.1. Further on, results comprise simplified magnetic phase diagrams, an analysis of the magnetic contribution and magnetic entropy. First measurements of magnetocaloric effect were attempted (Appendix C).

The currently available samples suitable for heat capacity measurements are listed in Table 3.1, including the three compounds in all directions of interest. At the start of this study, only the larger HoCu (OFZ-95-3-3-h) and ErCu (OFZ-104-3-4-1) samples were available. Other samples were prepared in the second half of the thesis for future studies.

The detailed determination of HoCu magnetic phase diagram, conducted during the master thesis of M. Rahn, showed that the saturation fields can not be reached with the present measurement system since they exceed $14\,\mathrm{T}$. Besides, the measurements in lower fields were inconclusive due to the aforementioned issue of magnetic torque. Since the topological Hall contribution of HoCu was studied in-depth, the test measurements were performed on HoCu. This sample was shared for neutron scattering measurements, and the Ho isotope soon became activated for several months. The second test sample ErCu OFZ-104-3-4-1 was used for further measurements.

setup	HoCu	ErCu
Standard	test measurements of	$T > 30\,\mathrm{K}$
Al	pulse size and post-processing	$\langle 110 \rangle$, $(0-14)\,\mathrm{T}$, $(2-25)\,\mathrm{K}$
Kevlar		$\langle 100 \rangle$, $\langle 111 \rangle$, both $(0-14)\,\mathrm{T}$, $(2-25)\,\mathrm{K}$

Table 3.1: Overview of conducted measurements.

compound	name	dimensions	orientation
HoCu	OFZ-95-3-3-h	$2 \times 2 \times 1\,(\mathrm{mm}^3)$	$\langle 100 \rangle$, $\langle 110 \rangle$
HoCu	OFZ-95-2-3-1	$1.5 \times 1.5 \times 1\,(\mathrm{mm}^3)$	$\langle 110 \rangle$, $\langle 111 \rangle$, $\langle 211 \rangle$
ErCu	OFZ-104-3-4-1	$1.75 \times 1.5 \times 1\,(\mathrm{mm}^3)$	$\langle 100 \rangle$, $\langle 110 \rangle$
ErCu	OFZ-104-3-4-2	$1.1 \times 1 \times 0.9\,(\mathrm{mm}^3)$	$\langle 110 \rangle$, $\langle 111 \rangle$, $\langle 211 \rangle$
TmCu		$1.4 \times 1.4 \times 1.4\,(\mathrm{mm}^3)$	$\langle 100 \rangle$, $\langle 110 \rangle$
TmCu		$1.35 \times 1.35 \times 1.35\,(\mathrm{mm}^3)$	$\langle 110 \rangle$, $\langle 111 \rangle$, $\langle 211 \rangle$

Table 3.1: Available RE-Cu samples for heat capacity measurements

3.1 Specific heat

3.1.1 ErCu in zero-field

Specific heat of ErCu was firstly measured in zero-field with the Standard setup for the entire available temperature range (Fig. 3.1). It shows saturation specific heat close to the Dulong-Petit law (≈ 25 JK^{-1}), as expected.

The low-temperature specific heat is represented on the right-hand side. It shows several anomalies at temperatures 8.8 K (1), 12.7 K (2) and 13.5 K (3). The sharp peak at 12.7 K is assumed to be the antiferromagnetic ordering temperature, the Néel temperature. The anomaly 3 is not visible in other magnetic measurements, likely being a structural phase transition.
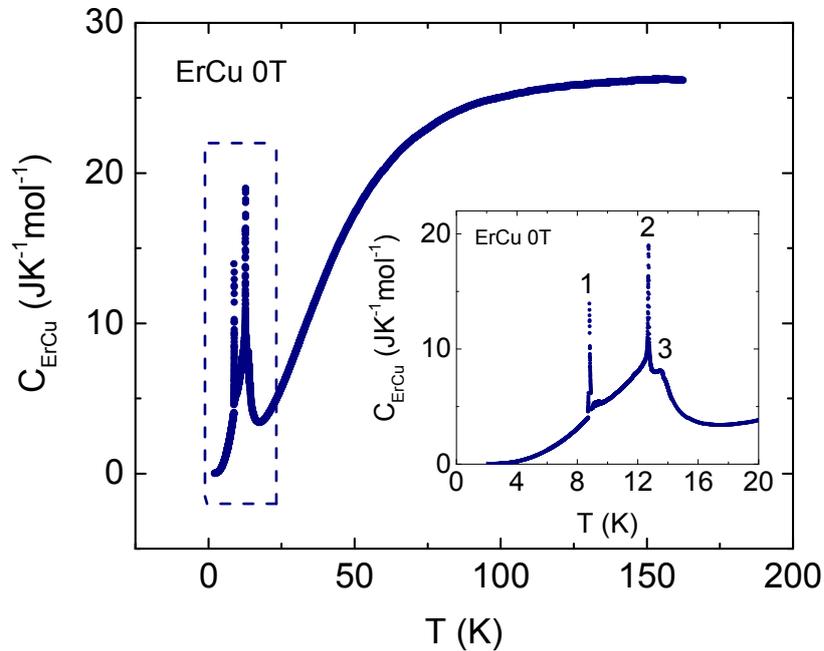
Figure 3.1: Specific heat of ErCu in zero-field for the entire temperature range measured with the Standard setup and the temperature range where magnetic ordering is present (inset). Several anomalies are visible, sharp peaks at 8.8 K (1) and 12.7 K (2), and a shoulder at 13.5 K (3).

Detailed view of the associated heat pulses belonging to the transitions 1, 2 and 3 in zero-field is given in Figure 3.2. The upper row (a-c) shows the typical temperature dependence of the sample (platform thermometer) and the lower row (d-f) the corresponding derived specific heat using the dual-slope method.

The transition 1 reveals a sharp kink, presumably an effect of latent heat in a typical first-order phase transition. Comparably, there is a latent heat effect present in the middle transition 2, less sharp than in the lower temperature phase transition.

There is a major difference in the time scales of pulses at these two transitions, the first relaxation time being around 20 s and the second 20 times longer, 400 s. The

specific heat changes in the two transitions are alike, 1 amounting to $12\,\mathrm{Jmol^{-1}K^{-1}}$ and 2 to $6\,\mathrm{Jmol^{-1}K^{-1}}$.

The third anomaly (3) is a much smaller $(0.5\,\mathrm{Jmol^{-1}K^{-1}})$ kink in specific heat, likely a structural transition, because it was not visible in the previous measurements which could see only the magnetic properties of the system. It is hard to deduce about the nature of this phase transition, because the used pulse size might smear out the latent heat effect supposing it is proportionally smaller, like the change in specific heat.

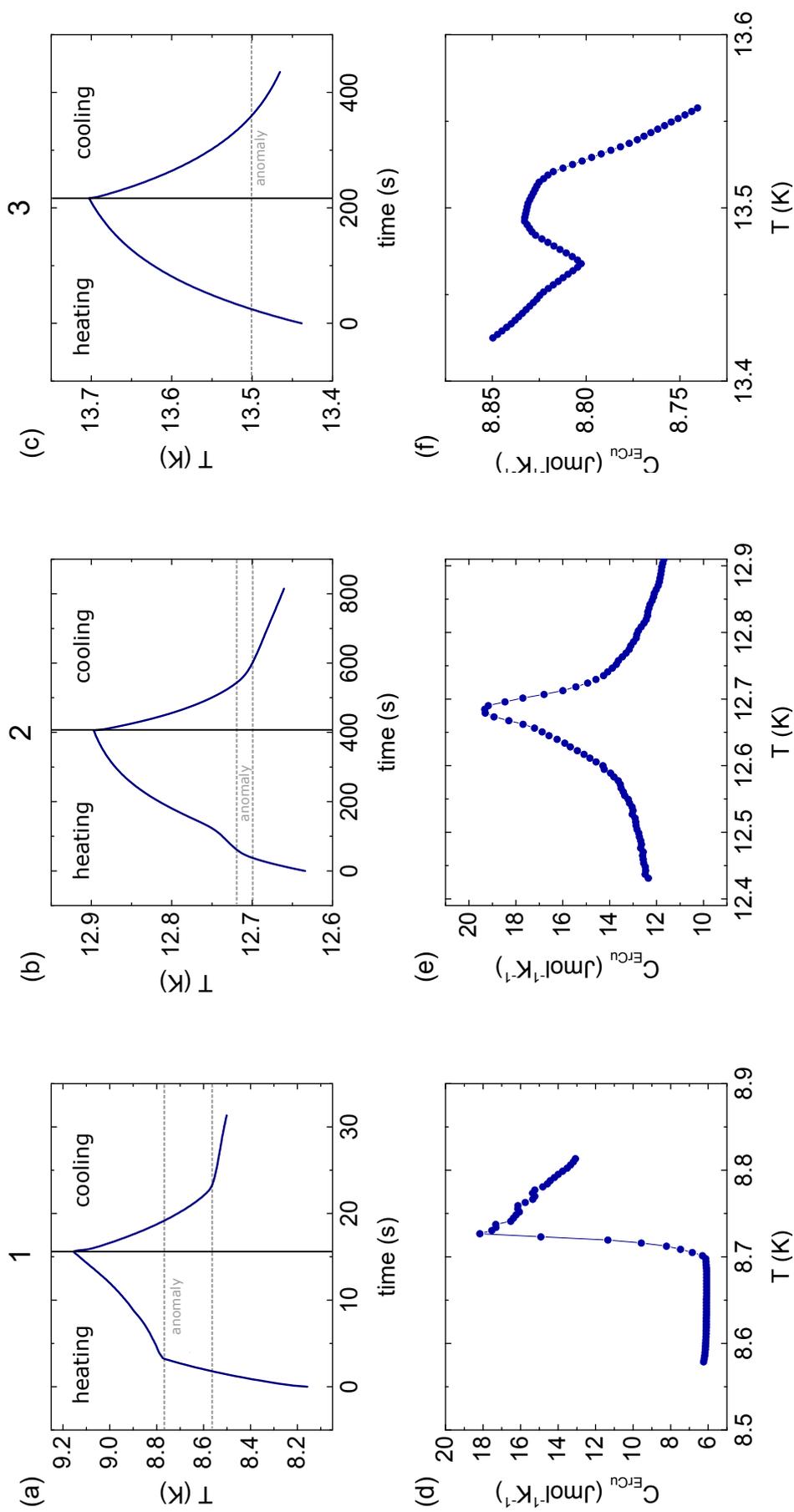Figure 3.2: Detailed view of the pulses (a-c) and heat capacities (d-f) of anomalies at $8.8\,\mathrm{K}$ (1), $12.7\,\mathrm{K}$ (2) and $13.5\,\mathrm{K}$ (3) in zero-field. Upper row shows the typical temperature dependence and the lower row the corresponding derived heat capacity.

3.1.2 ErCu in field

Figure 3.3 is the main result of this study, showing the heat capacity of ErCu in fields up to $14\,\text{T}$ for crystallographic axes $\langle 100 \rangle$, $\langle 110 \rangle$ and $\langle 111 \rangle$.

The $\langle 110 \rangle$ direction was measured using the firstly constructed Al setup while the other two directions were measured using the Kevlar setup, later on, determined as better suited for these measurements (Table 3.1). One can see that the saturation field can be achieved in the $\langle 100 \rangle$ and $\langle 111 \rangle$ directions, at $9\,\text{T}$ and $13.5\,\text{T}$, respectively. The $\langle 100 \rangle$ direction is the easy axis of the system while $\langle 110 \rangle$ is the hardest axis.

This is in agreement with the previous bulk measurements, but in disagreement with the crystal electric field (CEF) prediction, claiming the $\langle 110 \rangle$ to be the easy axis. CEF is, thus, not the dominating interaction at least in some parts of the magnetic phase diagram. It could be explained by quadrupolar exchange gaining importance, which may also give rise to complex spin structures.

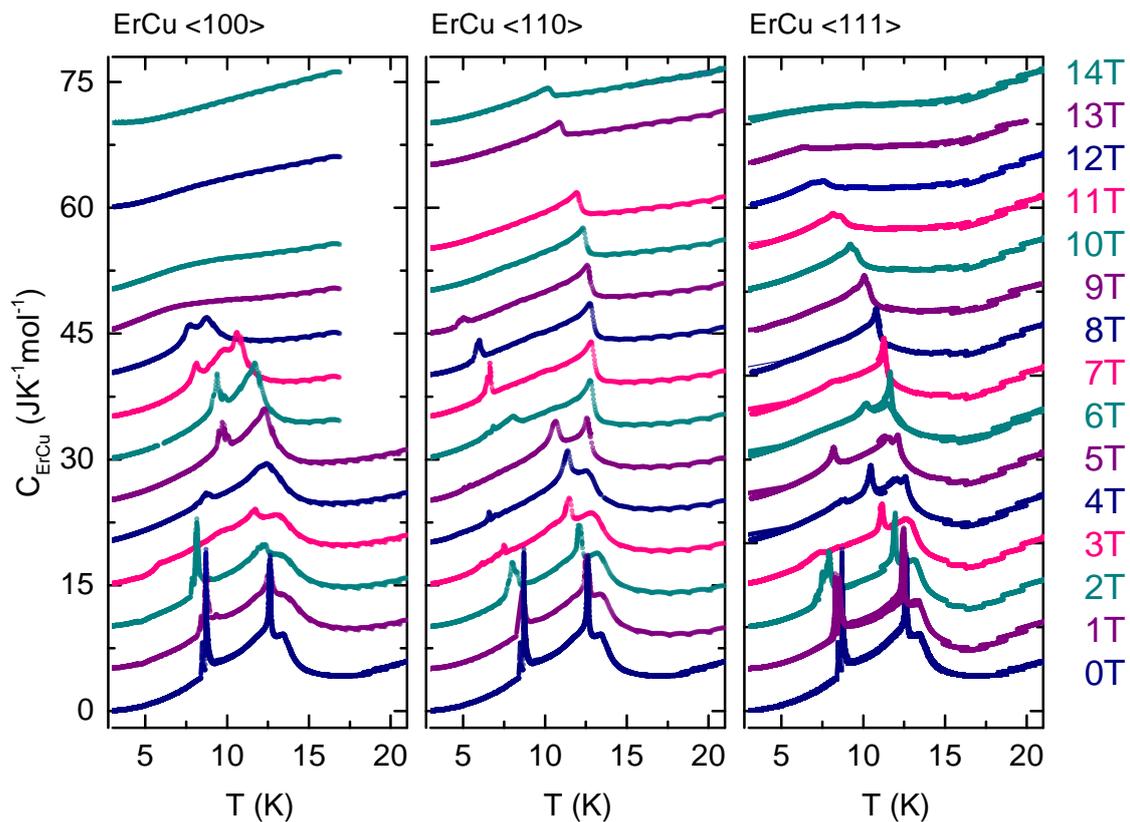Figure 3.3: Specific heat of ErCu measured in magnetic field up to $14\,\text{T}$ for crystallographic axes $\langle 100 \rangle$, $\langle 110 \rangle$ and $\langle 111 \rangle$. $\langle 110 \rangle$ direction was measured using the Al setup, while the other two directions were measured using the Kevlar setup, see Table 3.1. The plots were shifted by $5\,\text{JK}^{-1}\text{mol}^{-1}$ for clarity.

3.2 Phase diagrams

One can track the position of anomalies in field and temperature to construct the phase diagrams (Fig. 3.4). Zero-field phases are labelled A, B and C with increasing temperature, while the in-field induced phases are named D and E, the formed appearing in all three directions at lower temperatures and the latter solely in the $\langle 110 \rangle$ direction. The magnetisation and ac-susceptibility measurements in ErCu displayed a far larger number of features than the determined specific heat. It is possibly a result of tracking each feature in previous measurements multiple times and some of the transitions observed in these studies not being of thermodynamic origin. Lines are added as guides for the eye of the possible phases.

Noticeably, no phase transitions in heat capacity were observed at lower temperatures, because they become field-independent, fixed to a certain field. It is hence difficult to measure at the exactly correct field to see the lower temperature transitions. This problem can be overcome in magnetisation and ac-susceptibility measurements by carrying out field-sweeps or in magnetocaloric measurements. First attempts of magnetocaloric measurements with the Kevlar setup are shown in Appendix C.
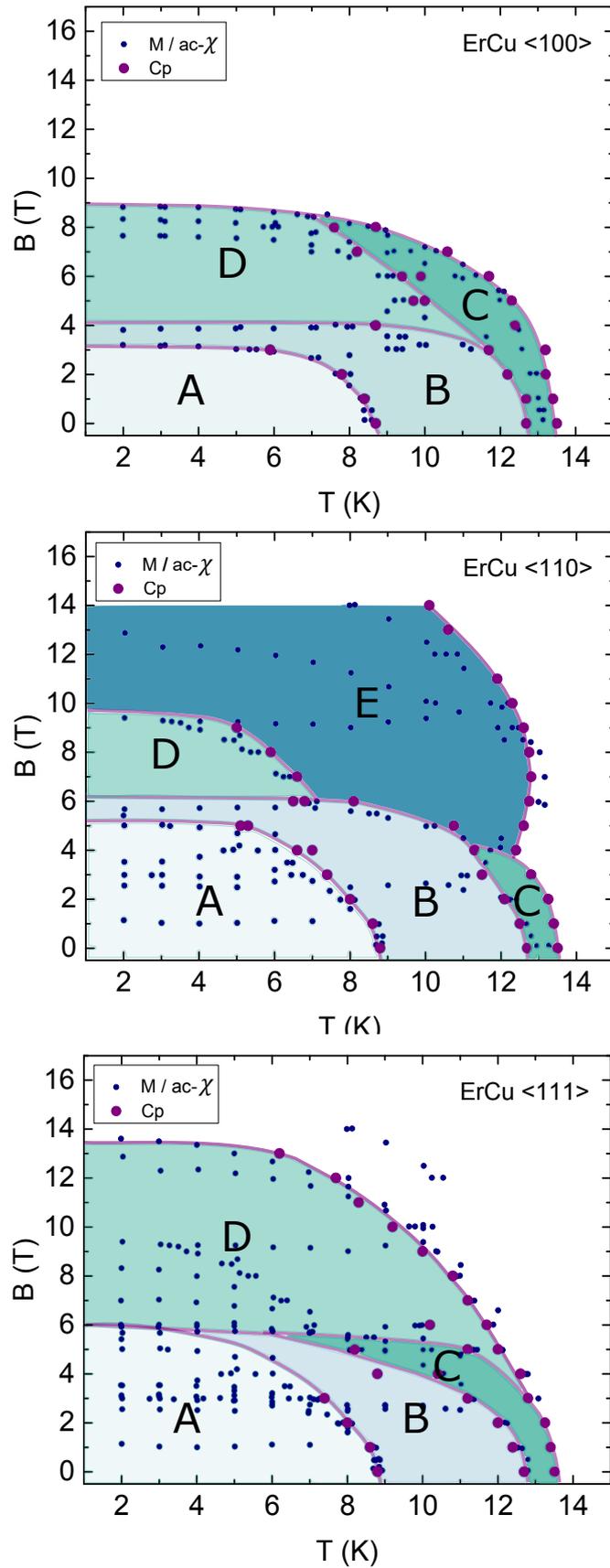
Figure 3.4: Phase diagrams of ErCu measured in magnetic field up to $14\,\text{T}$ for crystallographic axes $\langle 100 \rangle$, $\langle 110 \rangle$ and $\langle 111 \rangle$. The $\langle 110 \rangle$ direction was measured using the Al setup, while the other two directions were measured using the Kevlar setup.

3.3 Evaluation of the magnetic contribution to the heat capacity

One way to extract the magnetic contribution is to fit the electronic and the phononic part of specific heat and subtract them from the overall heat capacity. This approach can be hindered by a large magnetic contribution extending to low temperatures in a way that the Debye temperature and the Sommerfeld coefficient can not be correctly determined.

In the case of RE-Cu, it is possible to estimate the magnetic contribution by subtracting the specific heat of LuCu. It is a non-magnetic equivalent of Ho-, Er- and TmCu with the same crystal structure, but with the rare-earth atom Lu which has a full 4f shell, $[Xe]4f^{14}5d^16s^2$. The resulting approximate Lu^{3+} ion in the LuCu compound has the electron configuration $[Xe]4f^{14}$. Furthermore, the magnetic entropy can be evaluated from the information on magnetisation [60] or the specific heat [61], according to the discussion in 1.5.1.

3.3.1 Non-magnetic RE-Cu equivalent LuCu

A polycrystalline LuCu pill was prepared using spark plasma sintering. A $2\,\text{mm}$ sample cube was cut for heat capacity measurements.

The specific heat in the low-temperature regime consist of the phononic and the electronic part and has a temperature dependence

$$C(T) = \beta T^3 + \gamma T \tag{3.1}$$

where β is the coefficient from the phononic and γ the Sommerfeld coefficient from the electronic contribution.

Figure 3.5 represents the Specific heat of LuCu, as measured with the Standard setup, with a Debye model fit (Eq. 1.18) for constant volume. The measured values expectedly exceed the Debye model and the Dulong-Petit law since they are valid for a constant volume measurement while the measurements were carried out at a constant pressure (section 1.4). The Debye temperature from the fit equals $\Theta_D = (186.8 \pm 0.3)\,\text{K}$. If we show the C/T dependence on T^2, as in the inset of Figure 3.6, a linear dependence is expected

$$C(T)/T = \beta T^2 + \gamma T \tag{3.2}$$

In a linear fit, the intercept on the y-axis is the Sommerfeld coefficient $\gamma = (1.55 \pm 0.01)\,\text{mJmol}^{-1}\text{K}^{-2}$, while the slope amounts to $\beta = (0.140 \pm 0.001)\,\text{mJmol}^{-1}\text{K}^{-4}$. After subtraction of the LuCu specific heat from the ErCu specific heat, we assume the phononic and simple electronic part are accounted for and the remaining part is referred to as the magnetic part. Taking into account that the compound orders antiferromagnetically, another cubic temperature dependence is expected at low temperatures, from the magnetic contribution.

$$C_{ErCu} - C_{LuCu} = C_{AFM} = \zeta T^3 + \gamma^* \tag{3.3}$$
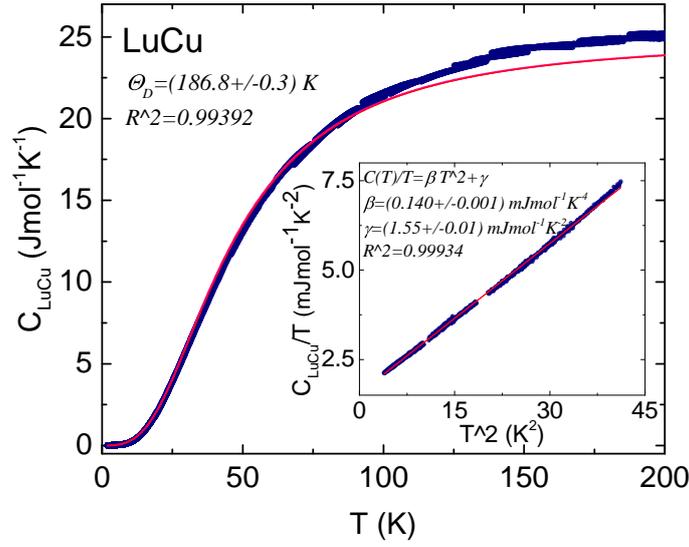
Figure 3.5: Specific heat of LuCu with a Debye fit for constant volume, giving a Debye temperature of $186.8\,\mathrm{K}$. The simple electronic contribution is determined by a linear fit of C/T to T^2, shown in the inset.
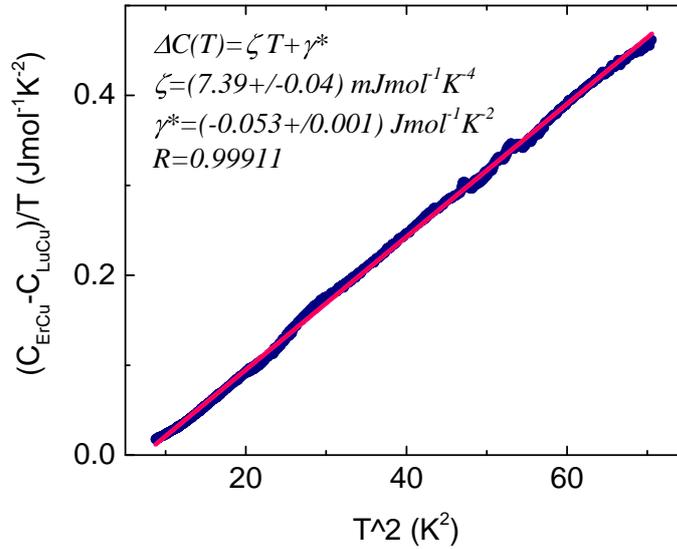
Figure 3.6: C/T to T^2 dependence of magnetic contribution to ErCu specific heat, showing a low-temperature lying cubic antiferromagnetic contribution. Its coefficient exceeds the phononic contribution by more than $\zeta/\beta \approx 50$ times.

Following the previous analysis, a C/T to T^2 dependence is plotted in Figure 3.6. The slope of the line is the ζ coefficient amounting to $(7.39\pm0.04)\,\mathrm{mJmol^{-1}K^{-4}}$ and the intercept $\gamma^* = (-0.053\pm0.001)\,\mathrm{Jmol^{-1}K^{-2}}$. One can observe that the antiferromagnetic cubic contribution is about $\zeta/\beta \approx 50$ times larger than the phononic contribution. Almost the entire heat capacity at low temperatures comes from the magnetic order-

ing. Nonetheless, it is important to account correctly for the LuCu contribution for the following entropy analysis.

3.3.2 Magnetic entropy

The magnetic contribution of ErCu specific heat is obtained by the previously described procedure. The specific heat- and temperature values were linearly interpolated resulting in 10000 points for the temperature range (0-25)K for ErCu and LuCu, the difference representing the magnetic contribution. The specific heat divided by T is linearly extrapolated to $0\,$K and numerically integrated according to the formula 1.10. The values saturate at $(20 - 25)\,$K. This temperature is defined as the point at which LuCu and ErCu heat capacity become virtually identical. Entropy as a function of temperature in zero-field is given in Figure 3.7. The saturation value of $2.6\,$Jmol^{-1}K^{-1} corresponds to a J value of 0.3 according to Eq. 1.9. A magnetic moment $J = 1/2$ would result in the saturation entropy $\Delta S \approx 5.76\,$Jmol^{-1}K^{-1}.
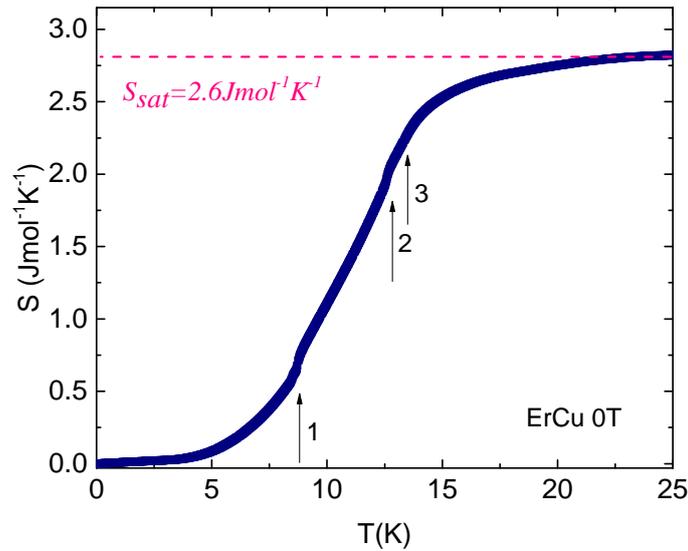
Figure 3.7: Entropy as a function of temperature for ErCu at 0T with marked anomalies and the saturation value of $2.6\,$Jmol^{-1}K^{-1}.

Surfaces of entropy as a function of temperature and field for $\langle 100 \rangle$, $\langle 110 \rangle$ and $\langle 111 \rangle$ are given in Figure 3.8. The highest entropy values are achieved in the $\langle 100 \rangle$ direction and the lowest in the $\langle 111 \rangle$ direction. The $\langle 100 \rangle$ direction accumulates the most entropy in the phase transition at $3\,$T, with it achieving the overall highest entropy values, despite being the easy direction. This indicates that the new field-induced phase possibly occurs by introducing a new k-ordering vector in the $\langle 100 \rangle$ direction. The three surfaces agree in the lower temperature range since no phase transitions were measured due to the weak field dependency which should be corrected for in future measurements. At higher temperatures, the entropy in the $\langle 110 \rangle$ rises for all available magnetic fields since the saturation field was not achievable.

Entropy dependence on field and temperature is also presented in Figure 3.9. In these graphs, the integer values of fields at which heat capacity was measured are visible as ridges. These graphs correspond to the phase diagrams of ErCu in Figure 3.4.
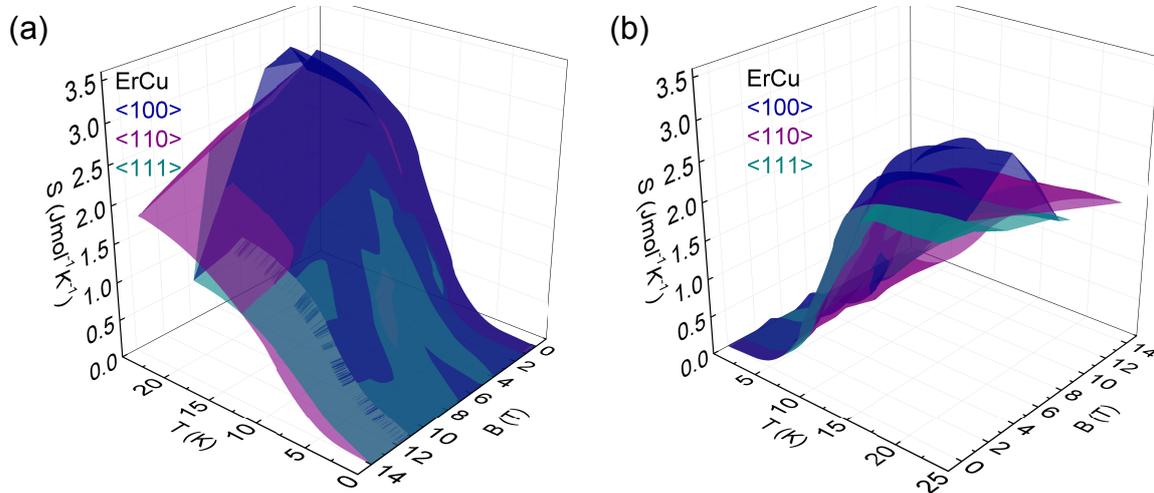
Figure 3.8: Entropy surfaces for three crystallographic axes of interest. Saturation fields were not accessible for the $\langle 110 \rangle$ direction leading to significant entropy values even at highest fields (a). The greatest entropy values are achieved in the $\langle 100 \rangle$ direction, as can be seen in (b), and the lowest in the $\langle 111 \rangle$ direction.
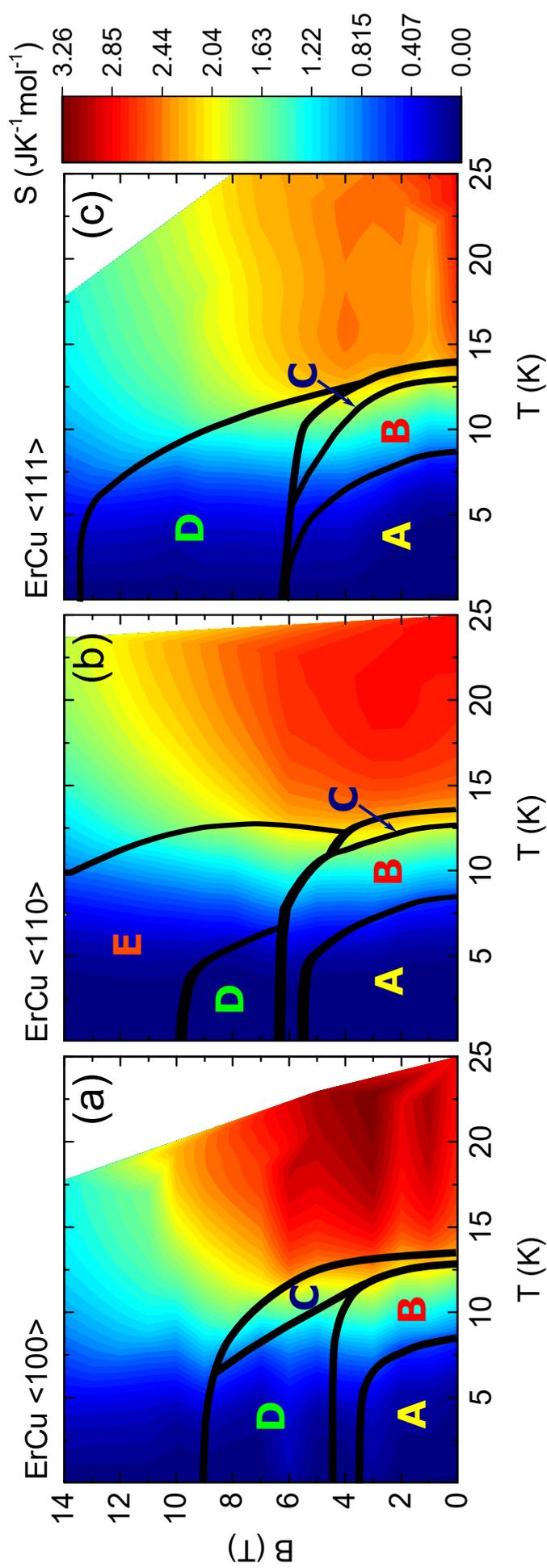
Figure 3.9: Color map of entropy as a function of temperature and field for three crystallographic axes of interest. The greatest entropy values are achieved with the magnetic field in the ⟨100⟩ direction (a). Entropy continually rises for magnetic field along the ⟨110⟩ direction (b). The lowest entropy values were deduced for magnetic field in the ⟨111⟩ direction (c). The ridges at integer values are a characteristic of the measuring procedure, which was done at fixed constant fields. The absolute entropy values are not to be taken as exact since the lower-temperature lying transitions in higher fields were not measurable and since the evaluation procedure changes the absolute values of heat capacity at phase transitions. The specific heat- and temperature values were linearly interpolated resulting in 10000 points for the temperature range (0-25)K and numerically integrated. They serve as a relative guide between different crystallographic directions.

4 Discussion

This chapter is intended as a summary of the achieved advancements and insights in respect to the thesis' aims listed in section 1.5.

Developing a mechanically stable calorimeter

- Two new setups, the Al setup and the Kevlar setup were implemented for measurements of heat capacity under large applied magnetic fields along hard magnetisation axes. In these setups, the platform is mechanically stable, and the sample is fixed by glue.

  The Al setup is an upgrade of the Standard setup which uses the same puck but changes the sample platform and the wiring. The electrical contact is separated from the mechanical and the thermal contact, which are connected through the Al plate and the fibreglass spacers.

  In the Kevlar setup, a new supporting construction was designed for the platform on a blank puck. This design separates the electrical, mechanical and thermal path, creating an opportunity to tune the thermal link for different samples.

- The new setups are applicable in the temperature range of interest $(2 - 50)\,\text{K}$ and presumably to lower temperatures. The sample heat capacity is comparable with the error of the addenda heat capacity at higher temperatures. In this case, the Standard setup was used, since there is no magnetic ordering and consequently no torque on the sample.

  The measuring and data evaluation procedures were established for RE-Cu materials. Heating pulses of $(10 - 20)\%$ of the bath temperature are applied, and dual-slope method is used for post-processing. One can perform a moving average and initial exclusion of single pulses to treat the derived heat capacity. To obtain a larger density of data points, a minimal moving average is favoured, and the initial exclusion can be conducted where appropriate to account for the thermal drag of the sample to the platform.

  The Kevlar setup requires less post-processing than the Al setup, likely because of the better defined thermal link. Because of this, it is the selected setup for most of the results presented in this thesis.

  Different setups were used to measure the heat capacity of ErCu for verifying the new setups. The slopes of the three curves agree while the absolute value differs by less than 5%.

- The specific heat values of MnSi in the A-phase measured with the Kevlar setup are in good agreement with the previous measurements, while the scattering can be accounted for by the experimental error. The uncertainty in the value of specific heat amounts to $\sigma_C/C \sim 2.5\%$ at $13\,\mathrm{K}$, a temperature near a phase transition. The peculiar pulse shapes were explained by the internal relaxation times.

Investigating RE-Cu compounds

- Heat capacity was measured in fields up to $14\,\mathrm{T}$ for ErCu in $\langle 100 \rangle$, $\langle 110 \rangle$ or $\langle 111 \rangle$ directions. The saturation field can be achieved in the $\langle 100 \rangle$ and $\langle 111 \rangle$ directions at $9\,\mathrm{T}$ and $13.5\,\mathrm{T}$, respectively. The $\langle 100 \rangle$ direction is the easy axis of the system while $\langle 110 \rangle$ is the hardest axis.

  This is in agreement with the previous bulk measurements and signifies that the crystal electric fields (CEF) are not the dominating interaction at least in some parts of the magnetic phase diagram. A possible alternative interaction to CEF explaining the observed behaviour is the quadrupolar exchange, which could result in complex spin textures as well.

  Features at lower temperatures were not accessible since they are weakly field dependent and measurements were conducted at fixed fields, missed in these experiments. First attempts of magnetocaloric measurements with the Kevlar setup were undergone, but the constraint on the slowest ramping speed of the magnet resulted in inconclusive outcomes.

- From these measurements, phase diagrams were constructed and superimposed on the previous phase diagrams. Substantially fewer features were visible using heat capacity, simplifying the former phase diagrams.

  Anomalies in zero-field at $8.8\,\mathrm{K}$, $12.7\,\mathrm{K}$ and $13.5\,\mathrm{K}$ were observed more closely, the first two being sharp peaks while the third is a small shoulder. The third phase transition is not visible in other magnetic measurements, and is, hence, conceivably a structural phase transition.

- To evaluate the magnetic contribution to specific heat, a non-magnetic equivalent of RE-Cu compounds, LuCu, was prepared. Its heat capacity represents the crystal structure phononic- and the simple electronic contribution which were subtracted from the measurements on magnetic RE-Cu. The Debye temperature from the fit equals $\Theta_D = (186.8 \pm 0.3)\,\mathrm{K}$, the Sommerfeld coefficient $\gamma = (1.55 \pm 0.01)\,\mathrm{mJmol^{-1}K^{-2}}$ while the coefficient of the cubic phononic contribution at low temperatures amounts to $\beta = (0.140 \pm 0.001)\,\mathrm{mJmol^{-1}K^{-4}}$.

The remaining magnetic contribution shows a characteristic antiferromagnetic cubic temperature dependence, more than 50 times stronger than the phononic contribution.

Entropy diagrams were deduced from the magnetic contribution to heat capacity. The absolute values of entropy are not reliable since the lower temperature transitions were not measured during this thesis, and the post-processing of heat capacity importantly influences its absolute values near phase transitions. Despite these limitations, it is possible to conclude on the relative entropies gathered in different crystallographic directions.

The largest entropy values appear in the $\langle 100 \rangle$ direction, accounted by a pronounced peak at $2\,\text{T}$, the entropy continuously rises with field for the $\langle 110 \rangle$ since the saturation fields were not achieved, and the $\langle 111 \rangle$ has the lowest overall entropy in the entire temperature and field range according to the current results.

5   Conclusion and outlook

The project was motivated by a search for topologically non-trivial magnetic phases, such as the skyrmion lattice. Rare earth intermetallics were extensively studied since the 1970s, both experimentally and theoretically, but solely on polycrystalline samples. The Ho, Er- and Tm- Cu display multi-k magnetic orderings, which singled them out as materials of interest for this thesis. Strong CEF effects in the cubic symmetry constrain the magnetic moments to the high symmetry $\langle 100 \rangle$, $\langle 110 \rangle$ or $\langle 111 \rangle$ direction.

Large single crystals of the compounds HoCu, ErCu and TmCu, were prepared by optical floating zone prior to the study. Magnetisation, susceptibility and transport measurements had been used before to map the magnetic phase diagrams. They confirmed three magnetic phases in zero-field and several additional phases induced by a magnetic field. The Hall effect, sensitive to both band-structure- and real-space-topology, showed a giant Hall resistance with multiple transitions for HoCu and TmCu.

Measurements of the heat capacity in magnetic materials provide key information on the nature of the excitations and changes of entropy across the phase boundaries. They are of vital importance to distinguish the real thermodynamic phase transitions from numerous features tracked in previous bulk measurements. In magnetic materials with complex phase diagrams, strong mechanical torque in finite magnetic fields rendered them futile with the Standard experimental apparatus.

Two entirely new setups for heat capacity measurements were designed to ensure mechanical stability against torques acting on the sample when applying magnetic fields along the hard axes. They were constructed, characterised and optimised for RE-Cu compounds in the temperature range of interest, $(2-30)$ K. They both fit into a commercially available sample puck provided by the Physical Property Measurements System (PPMS) from Quantum Design.

Al setup consists of a screw tightened Al-plate as sample platform separated from the thermal bath by fibreglass spacers to slow down the relaxation process. The second, Kevlar setup, has a completely new structure, permitting to tune and adjust the setup for different materials. It proved to be the preferred setup for RE-Cu measurements due to a better defined thermal link.

A detailed characterization of the new setups was conducted in comparison to the conventional heat pulse calorimeter technique. We concentrated on the heat capacity of ErCu along the three principal crystallographic directions in the temperature range from 2 K to 200 K up to magnetic fields of 14 T. It enabled us to simplify the rich magnetic phase diagrams and identify a structural transition with no magnetic reason. Magnetic contribution in the compounds of interest was assessed by specific heat of a non-magnetic equivalent of the material - LuCu - prepared during this thesis.

The list below summarises how the present efforts could be supplemented and expanded in future projects.

- **Sister compounds**

  Additional samples of the sister-compounds HoCu and TmCu samples with different orientations were cut from the existing crystals. Presently, all samples are available for heat capacity measurements along the three significant crystallographic axes of interest.

- **High field measurements**

  For the HoCu compound and ErCu in $\langle 110 \rangle$ direction, heat capacity measurements must be continued to higher fields to complete the phase diagrams.

- **Magnetocaloric effect**

  Further magnetocaloric measurements need to be conducted in a system in which the magnetic field can be continuously swept at slow enough ramping rates. This would help establish the phase diagram for the lower temperature, as well.

  Another upshot of these results would be a more accurate calculation of the entropy and entropy changes over observed features.

- **Hall resistivity of ErCu**

  In analogy to the previously analysed topological Hall effect in HoCu [4], Hall resistivity of ErCu is to be measured and evaluated to clarify the development of magnetic phases emerging in field.

- **Entropy changes across first order phase transitions**

  Detailed analysis of the first order magnetic transitions from the magnetisation measurements is to be conducted according to the Clausius-Clapeyron relation (Eq. 1.30).

- **mK measurements**

  The Kevlar setup was designed to fit into the ADR cryostat so to carry out lower temperature measurements not only on these materials but other compounds which display the issue of magnetic torque.

- **Neutron scattering** In parallel to this thesis, neutron scattering experiments are conducted in the group by Wolfgang Simeth, within his doctoral thesis. The results of these experiments are to clear the magnetic structure of the studied RE-Cu materials.

Appendices

Appendix A   Berry curvature

In quantum mechanics, the Berry phase arises in a cyclic adiabatic evolution [62]. For a quantum mechanical system H, the parameters $\vec{R}$ change slowly enough $(\tau \gg \hbar/\Delta E)$, ΔE being the energy difference between neighbouring states, that the system remains in its eigenstate $|\psi(t)\rangle = |n(\vec{R}(t))\rangle$ for every t.

Since the change is cyclic $(\vec{R}(0) = \vec{R}(T))$, the Hamiltonian H returns to its initial state after T. The system eigenstate evolves according to the Schrödinger equation.

$$H(\vec{R}(t))|\psi(t)\rangle = i\hbar\frac{\mathrm{d}}{\mathrm{d}t}|\psi(t)\rangle \tag{A.1}$$

For the initial state $|\psi(0)\rangle = |n(\vec{R}(0))\rangle$, the solution at time t reads

$$|\psi(t)\rangle = e^{i\Phi(t)}|n(\vec{R}(t))\rangle \tag{A.2}$$

Taking into account the above expressions and the initial phase $\Phi(0) = 0$, the phase at the end of a cycle amounts to

$$\Phi(T) = -\frac{1}{\hbar}\int_0^T E_n(\vec{R}(t))\mathrm{d}t + i\int_0^T \langle n((\vec{R}(t))|\frac{\mathrm{d}}{\mathrm{d}t}|n(\vec{R}(t))\rangle \mathrm{d}t \tag{A.3}$$

The first term is a dynamic phase ϕ_d that a system in energy state E_n collects during a period T, $\phi_d(T) \equiv -\frac{1}{\hbar}\int_0^T E_n(\vec{R}(t))\mathrm{d}t$. We can rewrite the second term, considering that the system goes through a closed loop C in parameter space

$$\Phi(T) = \phi_d(T) + i\oint_C \mathrm{d}\vec{R}(t)\langle n(\vec{R})|\vec{\nabla}_{\vec{R}}|n(\vec{R})\rangle \tag{A.4}$$

The second term is than defined as the geometric (Berry) phase ϕ_g, an integral in the parameter space, independent of the rate at which the curve C is described and the energy of the system

$$\phi_g(C) \equiv i\oint_C \mathrm{d}\vec{R}(t)\langle n(\vec{R})|\vec{\nabla}_{\vec{R}}|n(\vec{R})\rangle \tag{A.5}$$

The geometric phase for normalised states is real and independent of the arbitrary choice of the system eigenstates up to a factor $2\pi n$, $n \in \mathbf{N}$. One can alternatively express the geometric phase in terms of the Berry connection A_n and Berry curvature Ω_n.

$$\phi_g = \oint_C \mathrm{d}\vec{R}\, A_n(\vec{R}) \tag{A.6}$$

$$\phi_g = \int_S \mathrm{d}\vec{S}\, \Omega_n(\vec{R}) \tag{A.7}$$

where $A_n(\vec{R}) = \langle n(\vec{R})|\vec{\nabla}_{\vec{R}}|n(\vec{R})\rangle$ is the Berry connection, a gauge dependent Berry potential. Using the Stokes' theorem for a boundary surface S of the closed path C introduces the Berry curvature Ω_n .

According to the analytical formula, derived by Thouless [63], the Hall conductivity can be connected to the topology of the electron band structure

$$\sigma_{ij} = -\varepsilon_{ijl}\frac{e^2}{\hbar}\sum_n \int \frac{\mathrm{d}\vec{k}}{(2\pi)^3} f(E_n(\vec{k}))\Omega_n^l(\vec{k}) \tag{A.8}$$

where ε_{ijl} is the Levi-Civita tensor. The Hall conductivity is proportional to the momentum space integral of one band's Berry curvature $\vec{\Omega}_n^l(\vec{k})$, weighted by the density of states f.

In a simple single-band model for the topological Hall effect of an itinerant antiferromagnet, the influence on the effective magnetic field can be estimated as [64]

$$1/\sigma_{xy}^{top} = P \, R_0 \, B_{eff} \tag{A.9}$$

$$B_{eff} = \left|\frac{q_\sigma^e}{e}\right| \vec{\Omega} \tag{A.10}$$

Appendix B   Allowed magnetic structures
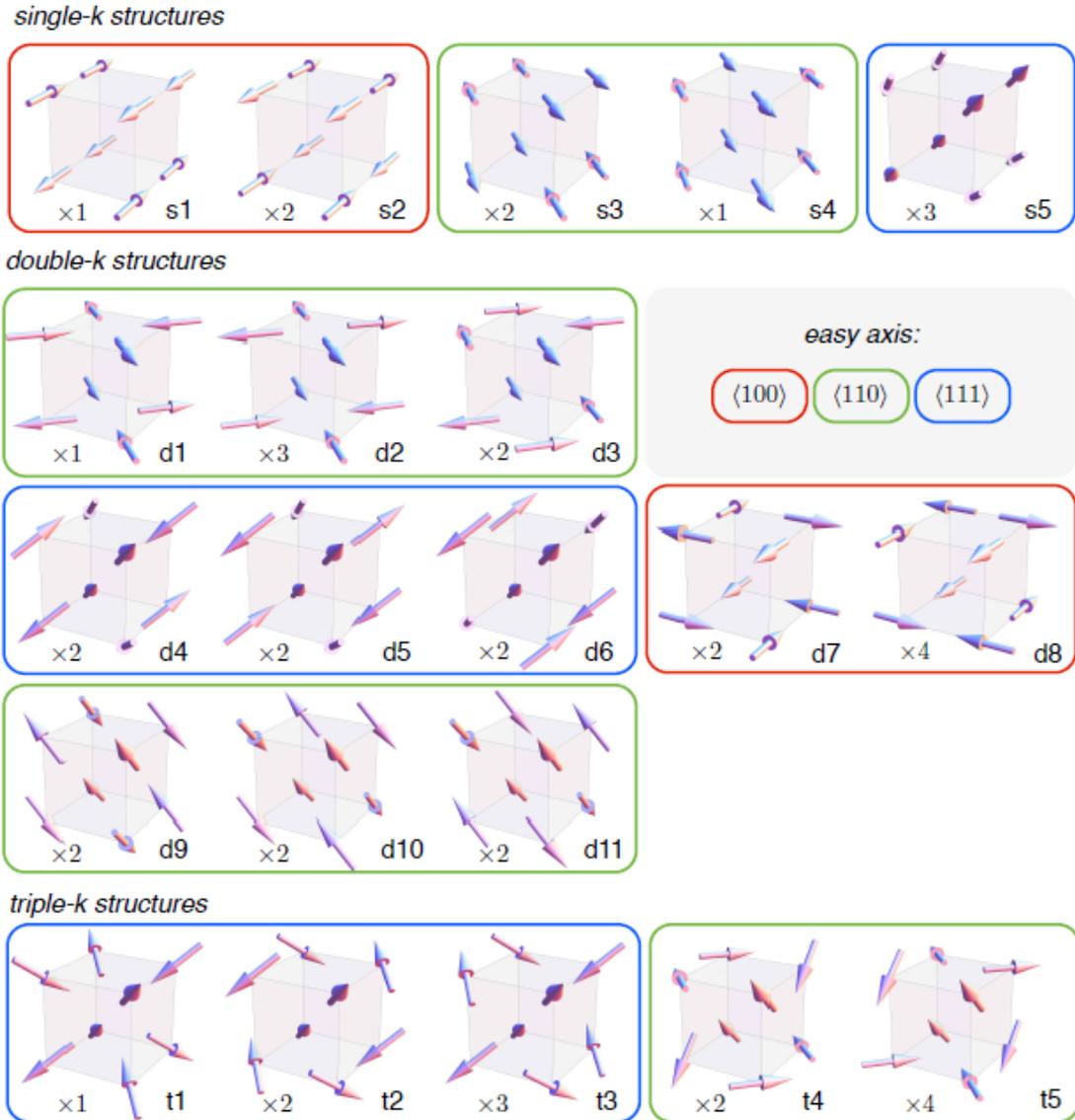
Figure B.1: Unit cells of the 21 possible high symmetry $\langle \frac{1}{2} \frac{1}{2} 0 \rangle$ spin structures, the multiplicity ("×2") of possible domains is indicated. [4]

Previous analysis of possible magnetic structures in RE-Cu [65] corresponds to present computer calculations taking two general assumptions, the constraint on the direction of magnetic moment to high symmetry axes and the constant modulus of the magnetic moment.

There exist 21 spontaneous high-symmetry magnetic structures fulfilling these conditions. They are presented in the Figure B.1. Neutron scattering experiments can be used to distinguish between the possible structures.

Appendix C   Magnetocaloric effect

The phase transitions depend weakly on field at lower temperatures, causing no visible features in temperature sweeps at a fixed field. For this reason, field-sweeps at a fixed bath temperature were conducted, following the idea in [66]. The Kevlar setup was used for these measurements.

This was also done in the PPMS system, using a Python script, instead of the MultiVu software. Platform temperature was tracked with a LakeShore temperature controller. The slowest ramping speed of the magnet in P14 cryostat is restricted to $9.3\,\text{Oe/s}$.

This was found to be too fast for the present design. We decreased the ramping speed by introducing additional waiting times between two fields, creating a step-wise sweep.
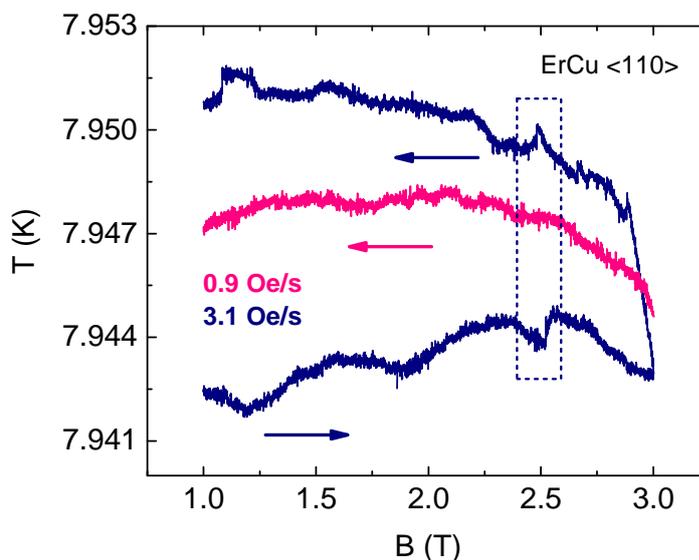
Figure C.1: Field-sweep at approximately $8\,\text{K}$ with ramping speed $3.1\,\text{Oe/s}$ shows three features in the up-sweep and a hysteresis, with just one matching feature in the down-sweep. Field-sweep at $0.9\,\text{Oe/s}$ shows no features.

The results for field-sweeps at about $8\,\text{K}$ at ramping speeds $3.1\,\text{Oe/s}$ and $0.9\,\text{Oe/s}$ are shown in Figure C.1. The field in the $3.1\,\text{Oe/s}$ sweep started at $1\,\text{T}$ and increased to $3\,\text{T}$. The temperature between the beginning and the end of the sweep increased by $0.002\,\text{K}$. When a subsequent down-sweep was performed, the temperature exhibited a sudden jump to higher temperatures and a further increase of $0.003\,\text{K}$ is visible. Only one of the anomalies is asymmetric to the up-sweep, perhaps due to a hysteresis of the heating-cooling processes. This anomaly at $2.5\,\text{T}$ can be matched to a point in the phase diagram found by heat capacity measurements.

Further on, a slower down-field-sweep at rate $0.9\,\text{Oe/s}$ still shows a drift in tem-

perature, but no features are noticeable.

The described artefacts are assumed to be the effect of the sample not being able to relax fast enough for these field scans, and the turning on and off of the magnet to reach the next field. In the future, the Kevlar Setup should be mounted in a system in which slow continuous field-sweeps are possible.

6 Prošireni sažetak

6.1 Uvod

Ovo istraživanje je potaknuto otkrićem rešetke skirmiona, topološki netrivijalnih kvazičestica, u MnSi-u [1]. Ispod temperature helimagnetnog prijelaza u srednjim magnetskim poljima, tri spirale feromagnetskog uređenja superponirane pod $120°$ stvaraju vrtloge spinova - skirmione (Slika 1.2). Jedna od indicija za topološko uređenje u materijalima je pojava magnetskog uređenja u više k smjerova.

6.1.1 RE-Cu spojevi

U opsežnim studijama provedenim 70-ih godina prošlog stoljeća [2], nađeno je da se RE-Cu materijali (RE = Ho, Er, Tm) antiferomagnetski uređuju ispod temperatura $(7 - 27)$ K i to u više k smjerova (Slika 1.4). Ti materijali su kemijski ekvivalentni jer je 4f orbitala koja daje magnetska svojstva zasjenjena zajedničkim 5s i 5p orbitalama (Slika 1.5) i kristaliziraju u jednostavnu CsCl kubičnu strukturu (Slika 1.5 (b)). Njihovi elektronski sustavi su jako korelirani s izraženom magnetskom anizotropijom. Kao takvi su od posebnog interesa zbog snažne međuigre spinskih i orbitalnih stupnjeva slobode.

Teorijska razmatranja relevantnih interakcija u ovim sustavima su utvrdila da je smjer magnetskog momenta duž jedne od glavnih osi određenih kristalnim poljima tj. duž $\langle 100 \rangle$, $\langle 110 \rangle$ i/ili $\langle 111 \rangle$ kristalnog smjera [21]. $\langle 110 \rangle$ je predviđena kao laka magnetska os prema utjecaju kristalnog električnog polja. Klasificiramo li magnetska uređenja prema Fourierovim komponentama spinskih struktura, može se utvrditi 21 moguća spinska struktura dozvoljena simetrijom (Slika B.1).

6.1.2 Dosadašnja istraživanja

Prijašnja istraživanja ovih materijala su rađena na polikristalnim uzorcima koji su onemogućavali točno utvrđivanje magnetske strukture. Prvi monokristalni uzorci su dobiveni u E51 grupi na Tehničkom sveučilištu München (Slika 1.9).
Kako bismo istražili topološka svojstva spinova, možemo provesti neutronska mjerenja ili identificirati topološku komponentu u transportnim mjerenjima - Hallovom efektu. Matematički i grafički prikaz doprinosa od normalnog, anomalnog i topološkog Hallovog efekta te rezultati mjerenja za HoCu su prikazani na Slici 1.3. Topološki Hallov efekt u HoCu je anizotropan, mijenja predznak kao funkcija temperature, nije monoton kao funkcija polja i dostiže apsolutne vrijednosti od $2 \mu\Omega$cm pri niskim temperaturama. Te karakteristike su naznaka netrivijalne topološke strukture u RE-Cu materijalima.
U grupi E51 su dosad provedena mjerenja ac-susceptibilnosti, magnetizacije i transportnih svojstava ovih materijala s ciljem izrade faznih dijagrama i određivanja magnetske strukture [4], [35]. Zbog dostupnosti uzoraka tijekom ovog projekta i

magnetskih polja u jakosti do $14\,\mathrm{T}$, fokusirat ćemo se na na ErCu spoj čiji su fazni dijagrami duž tri bitne osi prikazani na Slici 1.13. Iako se za neke od prikazanih faza pretpostavlja da se ne radi o stvarnim termodinamički drugačijim fazama različitim u energiji, brojnost otkrivenih faza ukazuju na kompleksnost ovih spojeva. Zaključak o njihovoj prirodi može se donijeti promatranjem toplinskog kapaciteta.

6.1.3 Termodinamička razmatranja

Toplinski kapacitet je od fundamentalne važnosti za istraživanja novih kvantnih stanja u fizici čvrstog stanja. Kao derivacija entropije po temperaturi, govori nam o prirodi i veličini faznih prijelaza između faza. Analogna veličina je magneto-kalorijski koeficijent, tj. derivacija entropije po polju.

Pomoću izmjerenih vrijednosti toplinskog kapaciteta moguće je rekonstruirati entropiju kao funkciju temperature i magnetskog polja, uz ograničenje na kvalitativnu analizu zbog toga što niže temperature nisu dostupne mjerenjima i što apsolutne vrijednosti toplinskog kapaciteta na faznom prijelazu ovise o korištenoj tehnici i načinu obrade mjerenja toplinskog kapaciteta.

Toplinski kapacitet tipično ima fononski, elektronski i magnetski doprinos. Fononski doprinos se može opisati Debyevim modelom i daje kubičnu temperaturnu ovisnost pri niskim temperaturama, a na visokim temperaturama saturira u Dulong-Petitov zakon. Elektronski doprinos ima linearnu temperaturnu ovisnost, a ponašanje magnetskog doprinosa ovisi o uređenju koje je prisutno u sustavu. U slučaju antiferomagneta radi se o kubičnom doprinosu.

6.2 Eksperimentalne metode

Mjerenja toplinskog kapaciteta u magnetskim materijalima koji imaju kompleksne fazne dijagrame uzduž osi teške magnetizacije su otežana zbog javljanja snažnog zakretnog momenta u konačnom magnetskom polju i neprikladnosti postojećih mjernih postava. Tijekom projekta su izrađena dva eksperimentalna postava za mjerenje specifičnog toplinskog kapaciteta u slučajevima kada je prisutan snažan magnetski moment i proučavani su navedeni RE-Cu sustavi.

Mjerenja su rađena u uređaju Physical Property Measurements System (PPMS) od Quantum Designa s dostupnim magnetskim poljem $\pm 14\,\mathrm{T}$ i temperaturnim područjem $(1.8 - 400)\,\mathrm{K}$. Korištena je relaksacijska metoda mjerenja koja ima mogućnost obrađivanja pulseva kao da su mjereni adijabatskom metodom.

6.2.1 Toplinski kapacitet

Shematski prikaz i slika sklopa za mjerenja toplinskog kapaciteta su prikazani na Slici 2.1. Važni dijelovi postava su platforma za uzorak, termometar, grijač te termalna

kupka. Bitno je osigurati električni, mehanički i termalni kontakt uzorka do termalne kupke.

Toplinski kapacitet se mjeri praćenjem temperature uzorka tijekom i nakon primjene pulsa konstantne snage na grijaču. Karakteristike postava su toplinski kapacitet postava C_a, toplinska vodljivost između termalne kupke i platforme K_1 te između platforme i uzorka K_2. Model koji daje vremensku ovisnost temperature platforme je prikazan u 2.1.1, a rezultantni puls na Slici 2.2 (b).

Metode mjerenja toplinskog kapaciteta u PPMS uređaju

Dvije osnovne metode mjerenja toplinskog kapaciteta provođene u PPMS-u su metoda malih pulseva $(0.1 - 2)\%$ i metoda velikih pulseva $(10 - 30)\%$. U prvoj metodi se pri obradi koristi teorijski model koji pretpostavlja konstantnu vrijednost toplinskog kapaciteta i vodljivosti tijekom mjerenja, što nije ispunjeno za fazne prijelaze. U drugoj metodi se pulsevi naknadno obrađuju prema izrazu 2.7 direktno koristeći definiciju toplinskog kapaciteta. Prikaz obrade pulseva je dan na Slici 2.4.

Moguće je odvojeno promatrati krivulje grijanja i hlađenja ili koristiti obje krivulje. Posljednja metoda je utvrđena kao preferirana uz dodatno izglađivanje te isključivanje početnog dijela pulse. Eksperimentalna greška je procijenjena na 2.5% što dolazi od kašnjenja temperature uzorka za temperaturom platforme.

Standardni postav

Standardni postav na Slici 2.6 (a) se sastoji od postolja (puck) i okvira na kojem je obješena $3 \times 3\,\mathrm{mm}^2$ safirna ili $\mathrm{Al_2O_3}$ platforma pomoću osam $75\,\mu\mathrm{m}$ Au-Pd žica. One pružaju električni kontakt, mehaničku podršku i termalni put K_1 za platformu što je prikazano na Slici 2.6 (b).

$\mathrm{RuO_2}$ grijač i Cernox termometar se nalaze s donje strane platforme te su njihovi kontakti načinjeni naparivanjem zlata. Toplinski kapacitet postava je zanemariv (nJK^{-1} na $15\,\mathrm{K}$) naspram toplinskog kapaciteta uzorka (mJK^{-1} na $15\,\mathrm{K}$). Uzorak se termalno povezuje malom količinom ($1\,\mathrm{mg}$) Apiezon N masti. Termalni kontakt između platforme i termalne kupke je dominiran žicama termometra i grijača jer se postolje nalazi u visokom vakuumu.

PPMS kalibracija se sastoji od mjerenja toplinskog kapaciteta postava C_a i određivanja toplinske vodljivosti K_1 te je provedena u nekoliko magnetskih polja. Jedan puls se sastoji od 256 točaka. Obično se nakon mjerenja provodi naknadna obrada izglađivanjem do 10% kojom se gubi na gustoći podataka ili isključivanjem početnog dijela pulsa po potrebi kako bi se uklonio efekt kašnjenja temperature uzorka za temperaturom platforme. Za RE-Cu materijale je prema širini faznih prijelaza utvrđena adekvatna veličina pulsa $(10 - 20)\%$ (Slika 2.7).

6.2.2 Razvoj i usporedba postava

Mjerenje toplinskog kapaciteta kompleksnih magnetskih sistema pri jakim magnetskim poljima nameće znatne i često protivne zahtjeve na eksperimentalni postav. Želimo minimizirati relativni doprinos postava toplinskog kapacitetu prema ukupnom signalu, ali imati mehaničku stabilnost kako bi nadvladali sile na uzorak s velikim magnetskim momentom. S druge strane, velik uzorak s velikim ukupnim magnetskim momentom ima duga relaksacijska vremena

Uvedena su dva nova postava: Al postav i Kevlar postav, izračunati toplinski kapaciteti postava C_a, toplinske vodljivosti $\kappa = K_1$ i rezultantna relaksacijska vremena $\tau = C/\kappa$ kada je $C = C_a$ pri kalibraciji i za $C = C_{tot}$ za mjerenja uzoraka. Cilj je održati τ mjerljivim u PPMS-u (> 0.1s), a učiniti ga što kraćim. Za dobru rezoluciju je potrebno da je toplinski kapacitet postava manji od toplinskog kapaciteta uzorka za područje od interesa $(2 - 30)$ K. Tipični uzorci su kvadri duljina stranice $(1 - 2)$ mm s toplinskim kapacitetom $(2 - 10)$ mJK^{-1} na 15 K.

Al postav

Al postav je prikazan na Slici 2.9, zajedno s odnosom mehaničkog, termalnog i električnog kontakta. Mehanički stabilna aluminijska pločica $(0.5$ mm$)$ uvedena je umjesto platforme u Standardnom postavu uz podloške od staklenog vlakna koji definiraju toplinski kontakt. Otpornik RX-102A $(1$ k$\Omega)$ predstavlja grijač, a Cernox CX-1010 temperaturni senzor. Oni su ručno dodani na stražnju stranu pločice, učvršćeni s GE ljepilom i električno spojeni s po dvije 0.7 cm duge i $30\,\mu$m manganin žice pomoću srebrne paste (EPO-TEK, H21S). Uzorak je fiksiran pomoću Stycast 2850 FT ljepila.

Kevlar postav

Kevlar postav (Slika 2.10) razdvaja mehanički, termalni i električni kontakt te je inspiriran postavom iz doktorskog rada A. Rosta [54]. Platforma je srebrni disk 0.5 mm debljine promjera 5 mm. Na gornju stranu platforme postavlja se uzorak pomoću Stycast ljepila kao u Al postavu, a sa stražnje strane nalaze se standardni SMD 1 kΩ otpornik za grijač i termometar CX-1010. Disk je obješen na Kevlar vlaknima od ~ 40 čvrstih $12\,\mu$m niti (Goodfellow, Kevlar @29-167) provučenih kroz platformu i prateću strukturu. Skica napravljene strukture je dana na Slici 2.11. Sastoji se od gornjeg pomičnog prstena kojim se postiže mehanička stabilnost i donjeg prstena s udubljenjima za prolaz električnih kontakata te tri vertikalne rupe u koje su uvučene šipke. Udaljenost prstena se namješta pomoću matica na šipkama. Termalni kontakt je postignut $(1 - 2)$ cm dugom srebrnom žicom od platforme do donjeg prstena. Kako bi se namjestio odgovarajuć termalni kontakt, korištene su žice dijametara $75\,\mu$m i $250\,\mu$m.

6.2.3 Usporedba postava

Toplinski kapacitet Standardnog postava je dominiran toplinskim kapacitetom grijača i termometra ($50\,\mu$JK na 15 K), a novih postava s Al pločicom toplinskog kapaciteta $0.5\,$mJK^{-1} na 15 K tj. s Ag diskom toplinskog kapaciteta $0.8\,$mJK^{-1} na 15 K. Tablica 2.1 je pregled doprinosa toplinskom kapacitetu postava pri 15 K, dok su vrijednosti za cijelo temperaturno područje na Slici 2.12.

Termalni kontakt između platforme i termalne kupke je u Standardnom postavu isključivo kroz Au-Pd žice i iznosi $18\,\mu$WK^{-1} na 15 K. U Al postavu je on dan podloškama od staklenih vlakana ($0.14\,$Wm^{-1}K^{-1} na 15 K), dok je u Kevlar postavu moguće mijenjati debljinu srebrne žice između $75\,\mu$m i $250\,\mu$m što daje termalni kontakt pri 15 K od $0.02\,$mWK^{-1} tj. $0.08\,$mWK^{-1}. Različiti segmenti termalnih vodiča su tablično prikazani u 2.2 za 15 K i grafički na Slici 2.14.

Relaksacijska vremena

Tau konstante koje proizlaze iz ovih vrijednosti su naznačene u Tablici 2.3 za kalibraciju i mjerenje uzorka tipičnog toplinskog kapaciteta $5\,$mJK na 15 K. Slika 2.15 daje uvid u odnose tau konstanti za širi temperaturni raspon. Standardni i Al postav imaju slične relaksacijske konstante u kalibraciji, dok su one značajno dulje za Kevlar postav. Pri mjerenju tipičnog uzorka su najdulje relaksacijske konstante Standardnog postava, srednje za Kevlar postav, a najkraće u Al postavu.

Bez obzira na sve, preferirani postav za mjerenje RE-Cu materijala je Kevlar postav jer je u njemu potrebno manje naknadno obrađivati podatke nego u Al postavu. To je moguće rezultat bolje definiranog termalnog kontakta.

Potvrda primjenjivosti

Kako bi potvrdili primjenjivost novih postava, mjeren je toplinski kapacitet ErCu te je slaganje potvrđeno kao što vidimo na Slici 2.16. Izvedena su mjerenja MnSi uzorka na $165\,$mT gdje postoji skirmionska faza (Slika 2.17 (a)). Pri mjerenju u polju očekujemo stoga dva fazna prijelaza kao na Slici 2.17 (b). Mjerenja s novim postavima su dobro odredila apsolutnu vrijednost i položaj faznog prijelaza unutar pogreške mjernog postava i točnosti termometra (Slika 2.18). Moguće objašnjenje odstupanjima je trostruko manji toplinski kapacitet MnSi uzorka u odnosu na ekvivalentne RE-Cu uzorke, nepotpuna termalizacija uzorka ili utjecaj potencijalne nehomogenosti magnetskog polja o kojem postoji značajna ovisnost.

6.3 Rezultati

Izmjeren je toplinski kapacitet ErCu bez magnetskog polja za raspon temperatura $(2 - 200)\,$K pomoću Standardnog postava (Slika 3.1). Opažena su dva prijelaza na $8.8\,$K i $12.7\,$K te anomalija na $13.5\,$K.

Detaljan pregled pulseva i rezultantnih promjena toplinskog kapaciteta za navedene anomalije je dan na Slici 3.2. Anomalija na $13.5\,$K nije opažena u dosadašnjim magnetskim mjerenjima te se stoga vjerojatno radi o strukturnoj promjeni.

Specifični toplinski kapacitet ErCu u magnetskom polju

Toplinski kapacitet je izmjeren u magnetskim poljima do $14\,$T u ErCu duž $\langle 100 \rangle$, $\langle 110 \rangle$ i $\langle 111 \rangle$ kristalografske osi (Slika 3.3). Uočava se da je laka os sustava $\langle 100 \rangle$ za koju je saturacijsko magnetsko polje $9\,$T. Teške magnetske osi su $\langle 110 \rangle$, za koju saturacijska polja nisu bila dostižna ($< 14\,$T), i $\langle 111 \rangle$ os sa saturacijskim magnetskim poljem od $13.5\,$T. To ukazuje da utjecaj kristalnog električnog polja nije dominantan barem pri nekim magnetskim poljima i temperaturama.

Pomoću tih mjerenja su izrađeni fazni dijagrami prikazani na Slici 3.4. Oni su pojednostavljeni u odnosu na prijašnje fazne dijagrame dobivene mjerenjima ac-susceptibilnosti i magnetizacije jer uzimaju u obzir samo prijelaze u kojima dolazi do promjene energije.

Magnetski doprinos

Magnetski doprinos specifičnom toplinskom kapacitetu je određen odračunavanjem specifičnog toplinskog kapaciteta LuCu (Slika 3.5), ne-magnetskog ekvivalenta ovih spojeva. Toplinski kapacitet LuCu predstavlja fononski i elektronski doprinos vodljivih elektrona toplinskom kapacitetu. Preostali magnetski doprinos ima očekivanu kubičnu ovisnost što se vidi na Slici 3.6. Doprinos fononskog i elektronskog dijela ukupnom toplinskom kapacitetu je malen na temperaturama kada je prisutno magnetsko uređenje, ali njegovo nam poznavanje omogućava odrediti kada magnetski doprinos više ne oslobađa nove stupnjeve slobode jer su tada specifični toplinski kapacitet ErCu i LuCu gotovo jednaki.

Poznavanjem magnetskog doprinosa specifičnom toplinskom kapacitetu možemo utvrditi funkciju entropije u ovisnosti o magnetskom polju i temperaturi. Rezultati su prikazani na Slikama 3.8 i 3.9. Ovdje se radi o kvalitativnoj analizi entropije. Prvi razlog tome je nedostatak mjerenja na nižim temperaturama koja su linearno ekstrapolirana, a drugi ovisnost integrala specifičnog toplinskog kapaciteta podijeljenog temperaturom o mjernoj tehnici i naknadnoj obradi podataka. Bez obzira na to, ovi podaci nam predočuju da je poljem inducirana faza najizraženija duž $\langle 100 \rangle$ osi što bi moglo indicirati promjenu magnetske strukture pobuđivanjem još jednog uređenja u tom k smjeru.

6.4 Zaključak

U projektu su istraživani RE-Cu materijali, HoCu, ErCu i TmCu koji su zbog prisutnosti antiferomagnetskog uređenja u više k smjerova i izrazitog topološkog Hallovog efekta kandidati za nastanak složenih spinskih tekstura. Mjerenja toplinskog kapaciteta pružaju informaciju o promjeni energije između faza, tipu prijelaza te razlikuju termodinamičku promjenu od magnetske reorijentacije bez promjene energije. Problem rotacije uzorka prilikom mjerenja toplinskog kapaciteta duž teške osi magnetizacije je riješen uvođenjem dvaju novih mehanički stabilnih postava.

Postavi za kalorimetrijska mjerenja u prisutnosti zakretnog momenta kod mjerenja u magnetskom polju duž teške osi magnetizacije

Prvi predložen dizajn je Al postav koji je nadogradnja na Standardni postav u mjernom uređaju Physical Property Measurement System (PPMS), Quantum Design. Električni kontakt je odvojen od mehaničkog i termalnog kontakta koji su spojeni kroz Al pločicu i podloške od staklenih vlakana. U Kevlar postavu, nova konstrukcija je napravljena na praznom postolju. Električni, mehanički i termalni kontakt su sasvim odvojeni i podesivi za različite uzorke.

Novi postavi i postupak mjerenja su optimizirani za područje od interesa $(2-50)$ K, a mogli bi se koristiti i na nižim temperaturama. Ustanovljeno je da je prikladna veličina pulsa $(10-20)\%$ te da Kevlar postav zahtjeva manje naknadne obrade podataka, dajući time veću gustoću rezultata.

Specifični toplinski kapacitet ErCu u magnetskim poljima do 14 T duž tri kristalografske osi od interesa

Toplinski kapacitet je izmjeren u magnetskim poljima do 14 T u ErCu duž $\langle 100 \rangle$, $\langle 110 \rangle$ i $\langle 111 \rangle$ kristalografske osi. U mjerenjima na 0 T opažena su dva prijelaza na 8.8 K i 12.7 K te anomalija na 13.5 K. Pomoću rezultata tih mjerenja su utvrđeni pojednostavljeni fazni dijagrami sustava duž navedene tri kristalografske osi. Izrađen je uzorak LuCu, ne-magnetskog ekvivalenta istraživanih spojeva. Mjerenja njegovog toplinskog kapaciteta su poslužila za određivanje entropije kao funkcije magnetskog polja i temperature. U tim rezultatima je primijećeno da poljem inducirana faza vjerojatno nastaje pobuđivanjem još jednog k vektora u $\langle 100 \rangle$ smjeru.

Nastavak istraživanja

Pripremljeni uzorci HoCu i TmCu su spremni za analogna mjerenja na novim postavima. Mjerenja za HoCu i ErCu trebaju biti izvedena u višim magnetskim poljima od $14\,$T. Potrebno je provesti magnetokalorijska mjerenja, započeta u Dodatku C, u kriostatu koji može kontinuirano mijenjati polje sporije nego PPMS uređaj. Mjerenja Hallovog efekta u ErCu spoju moraju biti izvršena i obrađena u skladu s analizom za HoCu.

Nadalje, Kevlar setup je dizajniran za kriostat s dilucijskim hladnjakom te će uskoro u njemu biti testiran. Paralelno s ovim istraživanjem provode se neutronska mjerenja koja bi trebala razjasniti magnetske strukture u RE-Cu materijalima.

Bibliography

[1] Mühlbauer, S., Binz, B., Jonietz, F., Pfleiderer, C., Rosch, B., A., N., Georgii, R., Böni, P. : Skyrmion lattice in a chiral magnet. // Science. Vol. 323, 5916(2009), pp. 915-919.

[2] Morin, P., Schmitt, D. : Quadrupolar interactions and magneto-elastic effects in rare earth intermetallic compounds. // Ferromagnetic Materials. Vol. 5, (1990), 5–132.

[3] Wills, A. S. : Validation of magnetic structures. // Zeitschrift für Kristallographie. Vol. 26 (2007), pp. 53–58.

[4] Rahn, M. Search for Topological Properties in Multi-k Magnetic Structures. Master thesis. München : Technische Universität München, 2009.

[5] Skyrme, T. H. R. : A Non-Linear Field Theory. // Proceedings of the Royal Society of London A. Vol. 260, 1300(1961), p. 127-138.

[6] Bak, P., Jensen, M., H. : Theory of helical magnetic structures and phase transitions in MnSi and FeGe. // Journal of Physics C: Solid State Physics., 13(1980), pp. 881–885.

[7] Dzyaloshinskii, I., E. : The theory of helicoidal structures in antiferromagnets. ii. metals. // Soviet Physics JETP. Vol. 20, 1(1965), pp. 223-231.

[8] Moriya, T. : Anisotropic superexchange interaction and weak ferromagnetism. // Phys. Rev. Vol. 120, 1(1960), pp. 91–98

[9] Franz, C., Freimuth, F., Bauer, A., Ritz, R., Schnarr, C., Duvinage, C., Adams, T., Blügel, S., Rosch, A., Mokrousov, Y., Pfleiderer, C. : Real-Space and Reciprocal-Space Berry Phases in the Hall Effect of $Mn_{1-x}Fe_xSi$. // Phys. Rev. Lett. Vol. 112, 18(2014), Nr. 186601.

[10] Yu, X.Z., Kanazawa, N., Onose, Y., Kimoto, K., Zhang, W.Z. : Near room temperature formation of a skyrmion crystal in thin-films of the helimagnet FeGe. // Nature Materials. Vol. 10, 2(2011), pp. 106-109.

[11] Münzer, W., Neubauer, A., Adams, T., Mühlbauer, S., Franz, C., Jonietz, F., Georgii, R., Böni, P., Pedersen, B., Schmitt, M., Rosch, A., Pfleiderer, C. : Skyrmion lattice in the doped semiconductor $Fe_{1-x}Co_xSi$. // Phys. Rev. B. Vol. 81, (2010), Nr. 041203.

[12] Seki, S., Yu, X. Z., Ishiwata, S., Tokura, Y. : Observation of skyrmions in a multiferroic material. Science Vol. 336, 6078(2012), pp. 198–201.

[13] Tokunaga, Y. et al. : A new class of chiral materials hosting magnetic skyrmions beyond room temperature. // Nat. Commun., Vol. 6, (2015), Nr. 7638.

[14] Neubauer, A., Pfleiderer, C., Binz, B., Rosch, A., Ritz, R., Niklowitz, P. G., Böni, P. : Topological Hall effect in the A phase of MnSi // Phys. Rev. Lett. Vol. 102, 18(2013), Nr. 186602.

[15] Radial probability of atomic orbitals, Orbitron, Mark Winter, `https://winter.group.shef.ac.uk`, 23.5.2016.

[16] Iandelli, A., Palenzona, A. : Atomic size of rare earths in intermetallic compounds. MX compounds of CsCl type. // Journal of the Less-Common Metals. Vol. 9, 1(1965), pp. 1–6.

[17] Walline, R. E., Wallace, W. E. : Magnetic and Structural Characteristics of Lanthanide—Copper Compounds. // The Journal of Chemical Physics. Vol. 42, 2(1965), pp. 604–607.

[18] Buschow, K. H. J. : Intermetallic compounds of rare earths and non-magnetic metals. // Reports on Progress in Physics. Vol. 42, (1979), pp. 13-73.

[19] Taylor, K. N. R. : Intermetallic rare-earth compounds. // Advances in Physics. Vol. 20, 87(1971), pp. 551–660.

[20] Campbell, I. A. : Indirect exchange for rare earths in metals. // Journal of Physics F: Metal Physics. Vol. 2, 3(1972), pp. 47-50.

[21] Lea, K. R., Leask, M. J. M., Wolf, W. P. : The raising of angular momentum degeneracy of f-electron terms by cubic crystal fields. // Journal of Physics and Chemistry of Solids. Vol. 23, 10(1962), pp. 1381–1405.

[22] Richter, M. : Band structure theory of magnetism in 3d-4f compounds. // Journal of Physics D: Applied Physics Vol. 31, (1997), pp. 1017–1048.

[23] Sablik, M. J., Teitelbaum, H. H., Levy, P. M. : Quadrupolar coupling and its contribution to electrical resistivity. AIP Conference Proceedings 10, (1973), pp. 548–552.

[24] CeB_6 Macroscopically Revisited. // Phys. Rev. Lett. Vol. 108, 2(2012), Nr. 026402.

[25] Morin, P., Pierre, J. : Thermal Expansion and Magnetostriction in Rare-Earth Equiatomic Compounds with Cu, Ag, Zn. // Phys. Stat. Sol. (a). Vol. 21, 161(1974), pp. 161-166.

[26] Morin, P., Schmitt, D. : Competition between multi-q antiferromagnetic structures in cubic rare earth-copper compounds. // Journal of Magnetism and Magnetic Materials. Vol. 21, 3(1980), pp. 243–256.

[27] Ho, J. C., He, S., Wu, C., Chien, T. S., Pavlovic, A. S. : Low temperature heat capacities of YCu and RECu (RE=Ho, Dy, Tb, Gd). // Chinese Journal of Physics. Vol. 29, 2(1991), pp. 147-155.

[28] Schmitt, D., Morin, P., Pierre, J. : Crystal field and magnetic properties in some cubic holmium compounds. Phys. Rev. B. Vol.15 4(1977), pp. 1698-1705.

[29] Morin, P., Pierre, J., Rossat-Mignod, J., Knorr, K., Drexel, W. W. : Crystal fields in ErCu, ErAg, and ErZn. // Phys. Rev. B. Vol. 9, 11(1974), pp. 4932-4938.

[30] Gignoux, D., Schmitt, D. : Competition between commensurate and incommensurate phases in rare-earth systems: Effects on H - T magnetic phase diagrams. // Phys. Rev. B. Vol. 48, 17(1993), pp. 12682-12691.

[31] Ibarra, M. R., Algarabel, P. A., Pavlovic, A. S. : High-field magnetostriction of TbCu, DyCu and HoCu. // Journal of Applied Physics. Vol. 67, 9(1990), pp. 4814-4815.

[32] Chao, C. C. : Electrical resistivity of equiatomic rare-earth-noble-metal compounds. // Journal of Applied Physics. Vol. 37, 5(1966), pp. 2081-2084.

[33] Birrs, R. R., Houldsworth, R. V., Lord, D. G. : Magnetoresistance in Holmium Copper compounds. // Journal of Magnetism and Magnetic Materials. Vol. 15-18, 2(1980), pp. 917–918.

[34] Wagner, M. : Single crystal growth of HoCu. Private communication.

[35] Hautmann, H. Untersuchung des magnetischen Phasendiagramms von ErCu. Bachelor thesis. München : Technische Universität München, 2013.

[36] Vojta, M. : Quantum phase transitions. // Rep. Prog. Phys. Vol. 66, (2003), pp. 2069-2110.

[37] Van Sciver, S., W. Helium Cryogenics Monograph Series. 2nd ed. New York : Springer, 2012.

[38] Ziman, J., M. Principles of the Theory of Solids. 2nd ed. Cambridge. : Cambridge University Press, 1972.

[39] Han, F. A Modern Course in Quantum Theory of Solids. 6th ed. Singapur : World Scientific, 2012.

[40] Kadanoff, L. P. et al. : Static Phenomena Near Critical Points: Theory and Experiment. // Rev. Mod. Phys. Vol. 39, 2(1967), pp. 395-431.

[41] Bauer, A., Pfleiderer, C. : Magnetic phase diagram of MnSi inferred from magnetization and ac susceptibility. // Phys. Rev. B. Vol. 85, (2012), Nr. 214418.

[42] Krey, C., Legl, S., Dunsiger, S., R., Meven, M., Gardner, J., S., Roper, J., M., Pfleiderer, C. : First Order Metamagnetic Transition in $Ho_2Ti_2O_7$ Observed by Vibrating Coil Magnetometry at Milli-Kelvin Temperatures. // Phys. Rev. Lett. Vol. 108, (2012), Nr. 257204.

[43] Stewart, G., R. : Measurement of low-temperature specific heat. // Rev. Sci. Instrum. Vol. 54, 1(1983), pp. 1-11.

[44] PPMS User's Manual. : Quantum Design, 2010.

[45] Brando, M. : Development of a relaxation calorimeter for temperatures between 0.05 and 4 K. // Rev. Sci. Instrum. Vol. 80, (2009), Nr. 095112.

[46] Bachmann, R. et al. : Heat Capacity Measurements on Small Samples at Low Temperatures. // Rev. Sci. Instrum. Vol. 43, 2(1972), pp. 205-214.

[47] Suzuki, H., Akira, I., Meingast, C. : Accurate heat capacity data at phase transitions from relaxation calorimetry. // Cryogenics Vol. 50, 10(2010), pp. 693-699.

[48] Hwang, J. S., Lin, K. J., Tien, C. : Measurement of heat capacity by fitting the whole temperature response of a heat-pulse calorimeter. // Rev. Sci. Instrum. Vol. 68, 1(1997), pp. 94-101.

[49] Bauer, A. Investigations of itinerant antiferromagnets and cubic chiral helimagnets. Doctoral thesis. München : Technische Universität München, 2014.

[50] Riegel, S., Weber, G. : A dual-slope method for specific heat measurements. // J. Phys. E: Sci. Instrum. Vol. 19, 10(1986), pp. 790-791.

[51] Pecharsky, V., K., Moorman, J., O., Gschneidner Jr., K., A. : A 3–350 K fast automatic small sample calorimeter. // Rev. Sci. Instrum. Vol. 68, 11(1997), pp. 4196-4207.

[52] PPMS brochures, Quantum Design, `https://www.qdusa.com/sitedocs/productBrochures/1070-002.pdf`, 20.5.2016.

[53] Lashley, J. C. et al. : Critical examination of heat capacity measurements made on a Quantum Design physical property measurement system. // Cryogenics Vol. 43, 6(2003), pp. 369-378.

[54] Rost., A. Magnetothermal properties near quantum criticality in the itinerant metamagnet $Sr_3Ru_2O_7$. Doctoral thesis. St. Andrews : University of St. Andrews, 2009.

[55] Pobell, F. Matter and Methods at Low Temperatures. 3rd ed. Berlin : Springer, 2007.

[56] Ekin, J., W. Han, F. Experimental techniques for low-temperature measurements : cryostat design, material properties, and superconductor critical-current testing. 3rd ed. Oxford : Oxford University Press, 2011.

[57] Ho, C., Y., Ackerman, M., W., Wu, K., Y., Oh, S. G. Oh, Havill, T. N. : Thermal conductivity of ten selected binary alloy systems // J. Phys. Chem. Ref. Data. Vol. 7, 3(1978), pp. 959-1177.

[58] Schulz, T., Ritz, R., Bauer, A., Halder, M., Wagner, M., Franz, C., Pfleiderer, C., Everschor, K., Garst, M., Rosch A. : Emergent electrodynamics of skyrmions in a chiral magnet // Nature Physics. Vol. 8, (2012), pp. 301-305.

[59] Bauer, A. and Garst, M., Pfleiderer, C. : Specific Heat of the Skyrmion Lattice Phase and Field-Induced Tricritical Point in MnSi. // Phys. Rev. Lett. Vol. 110, 17(2013), Nr. 177207.

[60] Bovo, L., Bramwell, S., T. Determination of the entropy via measurement of the magnetization: application to the spin ice $Dy_2Ti_2O_7$. // J. Phys.: Condens. Matter Vol. 25, 35(2013), Nr. 356003.

[61] Rost, A., W., Perry, R., S., Mercure, J.-F., Mackenzie, A., P., Grigera, S. A. : Entropy Landscape of Phase Formation Associated with Quantum Criticality in $Sr_3Ru_2O_7$. // Science Vol. 325, 5945(2009), pp. 1360-1363.

[62] Xiao, D., Chang, M.-C., Niu, Q. : Berry phase effects on electronic properties. // Rev. Mod. Phys. Vol. 82, 3(1959), pp. 1959-2007.

[63] Thouless, D. J., Kohmoto, M., Nightingale, M. P., Den Nijs, M. : Quantized Hall conductance in a two-dimensional periodic potential. // Phys. Rev. Lett. Vol. 49, 6(1982), pp. 405–408.

[64] Ritz, R., Halder, M., Franz, C., Bauer, A., Wagner, M., Bamler, R., Rosch, A., Pfleiderer, C. : Giant generic topological Hall resistivity of MnSi under pressure. // Phys. Rev. B. Vol. 87, 13(2013), Nr. 134424.

[65] Amara, M., Morin, P. : Multiaxial antiferromagnetic structures and quadrupolar interactions. // Physica B. Vol. 205, (1995), pp. 379-392.

[66] Tian, G. et al. : Large reversible magnetocaloric effect of light rare-earth inter-metallic compound Pr_5Si_3. // J. Alloys Compd. Vol. 496, 1(2010), pp. 517-520.